BEDFORM PATTERNS IN NEARSHORE SANDS

DOUGLAS JAMES WILSON

BEDFORM PATTERNS IN NEARSHORE SANDS.

A Thesis submitted to the School of Graduate Studies
in partial fulfillment of the requirements
for the degree of
Doctor of Philosophy
at
Department of Physics and Physical Oceanography
Memorial University
St. John's, Newfoundland
October, 1996

Abstract

In this thesis a self-organization mechanism is shown to reproduce the observed patterns of ripples in nearshore sands under waves. When viewed from above, these ripples assume a variety of patterns, including linear, brick pattern, oblique crossed sets, and lunate forms. Experimental and modelling evidence combine to demonstrate that the factors controlling bedform pattern include wave height and wave asymmetry, and the mechanisms of formation include self-organization in which the shape of the bed modifies the trajectories of those sand particles which are in motion such that a specific bed pattern is reinforced. In particular, the formation of crossed sets of ripples oblique to the incident wave direction is difficult to explain except by the self-organization mechanism described in this work, hence these crossed ripple sets are the principal focus here.

Previous field observations have associated these different patterns with depth and hence distance from shore, but little quantitative work has been done due to difficulties in making observations. In this study difficulties in making quantitative field observations were overcome by using a remotely operated, bottom mounted rotating head sidescan sonar system to image the bottom bedforms, and electromagnetic current meters and pressure sensors mounted on the same frame to quantify the wave forcing. Experimental results from a field experiment at Burley Beach, Ontario and wave tank results from two experiments at the National Research Council wave flume in Ottawa are presented. A simple computer simulation is developed to establish mechanisms of formation of the ripple pattern types observed.

Cross-ripples appeared in the field study at the rise and decline of each storm under

similar wave conditions each time. In the wave flume cross-ripples were observed for two different sand grain sizes under regular waves, grouping waves, and irregular waves. Thus cross-ripples are formed under a range of sand sizes and wave conditions. The computer model produces cross-ripples when there is asymmetry in the forcing under sufficiently energetic wave conditions. This is consistent with the field and laboratory results. There are no length scales of forcing in the model which correspond to the length scales of the bedforms produced. The sum of these observations supports the theory that cross-ripples form as a result of the self-organization mechanism.

Contents

List of Figures

List of Tables

Acknowledgements

The author wishes to thank all those who contributed their time and effort in making this thesis work an educational and rewarding experience, especially Dr. Alex Hay, for many creative ideas and long hours spent correcting this thesis. Invaluable encouragement was recieved from fellow staff and graduate students A. Crawford, L. Zedel, and J. Sheng. Thanks to T. Bowen for the hydrodynamic data from Burley beach and Ottawa 1993. Software and sonar images from Ottawa 1995 were provided by R. Craig.

A very important contribution to this thesis was the long hard hours spent by many to make the field experiments a success. For their help at the field locations we are grateful to R. Dittman, B. Guest, B. Roberts, J. Foley, and W. Paul (Memorial University); D. Hazen, N. Countway, S. McLean, A. Trivett, and P. MacAuley (Dalhousie University); and R. Brander, T. Aagaard, R. Atkins, K. Jagger, and B. Greenwood (University of Toronto). Special thanks to the National Research Council staff in Ottawa, particularly D. Willis and D. MacDonald. Support was provided in part by graduate fellowships from Memorial University of Newfoundland. The experiments were funded by the Operating and Strategic Grants and Collaborative Special Projects programs of the Natural Sciences and Engineering Research Council of Canada, and by the U.S. Office of Naval Research.

"Love all God's creation, the whole and every sand grain in it", F. Dostoevsky.

Chapter 1

Introduction.

Nearshore sand bedforms of the type commonly observed when wading at the beach continue to be studied by Geologists, Coastal Geographers, Earth Scientists, Hydraulic Engineers, and Oceanographers due to their importance in sandstone interpretation, large scale movement of sand, and in nearshore ocean dynamics. There is variety and complexity in these bedforms and the processes which form them. Under common wave and current conditions the bedforms have a strong influence on sand transport, and these bedforms are in turn strongly influenced by the sand transport. Studies of the formative mechanisms of nearshore sand bedforms have been hampered by the fact that most sand transport occurs under conditions where direct observation of the bed is difficult or impossible due to wave or current forces and water turbidity.

The difficulties involved in direct observation of bedforms under waves in the field have led to the majority of studies which measure both flow and bedforms being done in the laboratory. However, studies by Miller and Komar (1980a, 1980b) and Nielsen (1981) concluded that significantly different results are found in field and laboratory data, due to matters of scale, the presence of long-shore currents, and the irregularity of the waves and other field parameters. In this study the results from one field experiment and two subsequent laboratory wave flume experiments with nearly one to one scaling to the field experiment have been obtained and compared. Difficulties in observing the bedforms under the clouds of suspended sand have been overcome

by the use of a rotating sidescan sonar (Hay and Wilson, 1994).

This thesis is about determining the conditions and mechanisms under which sand bedforms occur by analysis of the images obtained from this sonar and correlating these results with simultaneously measured wave properties. In particular, the formation of cross-ripples will be examined in detail, as their formative mechanisms are currently largely speculative. Because the sidescan sonar information gives a plan view of the bottom, bedform patterns can be easily identified and quantified. Further insight into the formative mechanisms of the bedforms has been obtained by developing a computer simulation of the sand movement under vigorous wave forcing. Understanding the mechanisms of formation of the various bedforms will assist in the development of better prediction of sediment transport, and in the interpretation of bedforms preserved in the sedimentary record.

To introduce this subject, a brief (not comprehensive) historical background to bedform research is presented in the next section. The multi-disciplinary nature of this research has produced variety in the nomenclature, so a short discussion of bedform classification follows in section 1.2. Current understanding of the mechanisms of formation is presented in section 1.3, and theoretical background to the formative theories and computer simulation are covered in section 1.4. Evidence for the formative mechanisms of cross-ripples comes in part from wave and current measurements, so section 1.5 reviews the established methods of analyses of current meter data used in this study. Chapter 2 of this thesis describes the methods of data acquisition and the field and laboratory experiments from which the data have been obtained. Chapter 3 describes the results obtained from these experiments, especially those pertinent to cross-ripple formation. Chapter 4 describes a simple computer simulation model developed to explore the mechanisms of ripple pattern formation. Further details and discussion of the data analysis are included in Appendix A.

1.1 Historical Background.

Sand bedforms on beaches have been of interest to members of the Geological Science community since at least the 1800's (see, for example, Hunt 1882). Initially this interest stemmed from the desire to interpret ripple forms preserved in the sedimentary record in terms of paleo-environmental conditions and setting. Comprehensive reviews of these early studies are available in several texts, including Allen (1968, 1982) and Pettijohn, Potter and Siever (1987). Hydrologists became interested in riverine sand bedforms in the 1920's and 1930's (see for example Shields 1933) and Civil Engineers became involved in the study of sand bedforms in wave dominated environments during the Second World War, when the Allied forces were attacking beaches and sand bar formation influenced landing strategies. The main interest in these studies (some of which were published in Bagnold 1946) was the role of sand ripples in sand transport. Since this time there has been enormous growth in the industrial and recreational use of beaches, hence Geographers have come to study sand bedforms as they relate to sand transport and the longer term change in shorelines this transport creates. Other applications of an understanding of sand transport include harbour maintenance, erosion around man-made shoreline structures, and the restoration of recreational beaches. The interpretation of the sedimentary record has found increasing application in the exploration for petroleum resources.

Historically, approaches to the topic of sand bedforms have been divided into two general categories. Geologists tend to start with the bedform (often one preserved in the sedimentary record) and ask "what waves or currents formed it?" whereas Engineers and Oceanographers tend to ask, "given a wave and current field, what bedforms will be formed?". When the latter approach has been taken (as it has in this thesis), bedforms are typically classified according to three formative flow regimes: the uni-directional, or current formed bed; the oscillatory, or wave formed bed; and the combined flow, or wave-current bed (Sleath 1984).

The bedforms described in this study have been formed by oscillatory and combined flows. Yet the uni-directional flow regime is the most studied due to the application in rivers and streams. These studies comprise a large body of literature (see for example the text by Yalin 1977 or Raudkivi 1990). Many of the fundamental concepts and measurements in uni-directional flows are similar to those for the oscillatory flow case, and thus are used in this study. Bedforms formed under purely oscillatory flows have been studied in the laboratory, and the pure oscillatory motion is considered analogous to deep sea swell induced motions on the continental shelf. In the nearshore beach environment the flows have much less well defined period, direction, and spatial variations, and also have sometimes important currents superimposed, so would often be classified as combined flow. There has been very little quantitative study on combined flow bedforms in either the laboratory or the field (Sleath 1984, Amos et al. 1989).

Until the advent of commercially available SCUBA gear and underwater photography, quantitative field observations were limited to tidal beaches and observations while wading or boating in clear water (Hunt 1882, Bagnold 1946). Several important field studies of ripple forms in wave dominated environments were conducted with SCUBA gear in the 1950's and 1960's, including an extensive study by Inman (1957). In Inman's work several sites at different depths were each visited weekly over a period of several months by SCUBA divers. Ripple dimensions were marked on plastic sheets with grease pencil, and wave conditions were recorded where possible from the fathometer mounted on the small boat used as the divers' tender. Though comprehensive in scope, the diver observations tended to be qualitative or semi-quantitative in wave and current observations.

Bedform observations using other techniques include track mounted acoustic fathometer operated by a SCUBA diver (Dingler and Inman 1974), greased combs pressed into the bottom from piers (Kawata, Shirai, and Tsuchiya 1988), and underwater video, stereo, and shadow bar photography (for example Briggs 1989, and Boyd, Forbes and Heffler 1988). Underwater video and photography techniques have been

successful only in deeper water, as water turbidity and suspended sand reduce visibility in the near-shore zone. Thus the rotary head sidescan sonar images of the bed used in this study have provided a unique look at the bedforms as they are being formed in turbid water conditions.

In contrast with the field studies, laboratory studies tend to have very accurate measurements of wave or current parameters, but tend to be limited in their ranges of wave amplitude and period. These limitations have proved important because, as discussed in the section on ripple formation mechanisms, sand ripple formation is a highly non-linear process not particularly amenable to scaling down to model size. Three different types of laboratory apparatus have been employed in the study of ripple formation under oscillatory flows: wave tanks, oscillating sand trays, and oscillating water tunnels. The first studies were performed in small glass tanks with wave generation at one end (Hunt 1882), and with wave amplitudes and periods much smaller than those in field conditions. Only the most recent studies in large wave tanks have approached field wave conditions. Bagnold (1946) suggested that the near bed flow over an oscillating tray of sand in a tank of water is to first order equivalent to the flow caused by progressive water waves over a stationary bed of sand. His oscillating tray apparatus was capable of wave periods and amplitudes found in the field, limited only by the sliding of large quantities of sand off the tray at the largest amplitudes. However, recent studies have suggested that significant quantitative differences exist between oscillating bed results and wave-flume or field results (Miller and Komar 1980a, Nielsen 1992). Oscillating water tunnels have also been employed to obtain 'field scale' wave periods and amplitudes. The main limitation in the studies performed in water tunnels has been the size of the tunnels, which are typically rectangular in cross-section with dimensions less than 40 cm across and 20 cm high. There is also some question about the effects of the solid upper boundary of the tunnel. Comprehensive reviews of these studies are available in Nielsen (1981), and Sleath (1984).

These previous studies have provided classification schemes for bedform types,

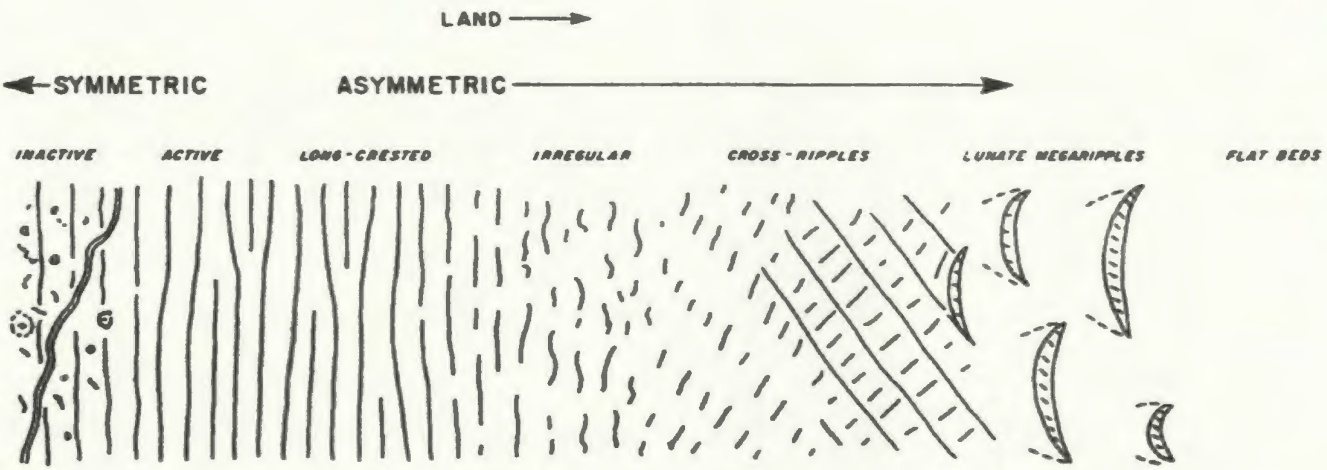

Figure 1.1: The sequence of bedform structures commonly observed as a function of distance off-shore (from Clifton 1976, observations from three different locations).

and have helped to define the conditions under which various bedforms occur. The conditions for the occurence of ripples of a given height, crest-crest length, and planform pattern provide information about the formative mechanisms indirectly, but there is considerable scatter in the field data. Detailed observation of ripple growth in wave tanks has shown that ripple formation is a highly non-linear interaction between the sand and waves. Thus there is considerable work to be done to understand the mechanisms of formation of these ripples.

1.2 Classification of Bottom Bedforms.

Sand bedforms come in a variety of sizes and shapes, depending on the characteristics of the sand and on the flow which forms them. Several classification and nomenclature schemes exist, such as those of Clifton (1976) and Allen (1982). The bedforms of principal interest in this thesis are those found in a nearshore barred beach environment under storm waves in moderately well sorted medium to fine grained sand (0.15-0.25 mm median diameter). The classification scheme postulated by Clifton in (1976) provides a useful conceptual basis for such a nearshore environment.

Using SCUBA, Clifton observed a variety of bedform sizes and shapes in the

nearshore under shoaling waves, and classified them according to an on-offshore sequence, as shown in Figure 1.1. In deepest waters offshore, inactive, or relict ripples (which were formed by earlier, longer wavelength waves) were observed. Then, in somewhat shallower water closer to shore, the bottom becomes influenced by the waves present at the time, and the bedforms are classified as active linear ripples. Still shallower and closer to shore, the ripple-crests become shorter and less regular, and the bedforms are classified as irregular ripples, which further shoreward grade into cross-ripples. On beaches with sufficiently energetic waves there has been observed a rather abrupt transition from cross-ripples to lunate megaripples, either with or without low amplitude linear ripples on their crests or diagonal ripple sets in their troughs. Finally closest to shore, flat bed may prevail. Though Clifton's classification system was conceived for planar, unbarred beaches, similar sequences have been observed on the offshore side of bars on barred beaches by Davidson-Arnott and Greenwood (1974) and Hunter, Clifton and Phillips (1979).

In the present work, the bedforms described in the Clifton scheme are denoted 'R' for relict ripples, 'L' for linear ripples, 'C' for cross-ripples, 'M' for lunate megaripples, and 'F' for flat bed. We have included another type, 'E' for evanescent, or short-lived linear ripples observed intermittently by the sonar. They have been described by Clifton as low amplitude ripples and would likely be the same type described in Dingler and Inman 1976 as "transitional ripples". Clifton postulated that this cross-shore progression of ripple patterns was related to the increase in wave height and asymmetry toward the beach.

For the purposes of investigating mechanisms of formation, bedforms in the Clifton classification scheme can be divided into symmetrical forms, intermediate forms, and asymmetrical bedforms. The symmetrical forms include: relict ripples, long-crested ripples and short-crested or brick pattern ripples. Then, with increasing wave asymmetry and height intermediate and asymmetrical forms occur: cross-ripples, evanescent ripples, and lunate megaripples. Figure 1.1 also illustrates that the three-dimensionality of bedform pattern increases as the waves become more asymmetrical.

Note that there is little mention of long-shore or cross-shore currents in this classification scheme. The effects of long-shore currents on cross-ripples is discussed further in the results section.

In the laboratory wave flume results of this thesis, the Clifton classification scheme was found to apply, but previous laboratory studies of ripples generally follow a different classification scheme developed out of work of Bagnold (1946) and expanded upon by others (Sleath 1984). This classification is based more on the mechanisms of formation as observed through the side windows in flumes. Bagnold describes rolling grain ripples which grow in crest-crest length over time and vortex, or orbital ripples which have crest to crest lengths λ proportional to the near bottom orbital diameter ($2a$, where a is orbital amplitude) of the forcing waves. He also observed that beyond a set orbital diameter which depends on sand size and composition, the ripple spacing reached a maximum (λ_m).

Inman (1957), Clifton (1976) and other observers noted that under some conditions the crest-crest spacing may grow beyond λ_m and then decline somewhat at even larger orbital diameters. When field results and laboratory results for linear ripples were plotted on the same graph, as shown in Figure 1.2, the laboratory ripples follow the line $\lambda = 1.3a$, and the majority of the field ripples appeared to be independent of the orbital diameter, with some overlap between the two types in which the crest-crest spacing is somewhere between. Clifton labelled these three domains orbital, suborbital, and anorbital, ripples. Bagnold's λ_m was very close to the anorbital ripple length. Inman and others have labeled the anorbital ripples as reversing current ripples. Wiberg and Harris (1994) used the ratio of ripple height to wave boundary layer thickness as a criterion for whether ripples were orbital (in which case the ripples were larger than the wave boundary layer as calculated using the sand grain roughness), anorbital (ripple heights less than a quarter of the wave boundary layer thickness), or suborbital (with ripple heights the same order of magnitude as the wave boundary layer thickness). Thus the classes can also be associated with different hydraulic domains under which different formative mechanisms may be expected to

apply.

1.3 Mechanisms of Formation.

A variety of mechanisms have been postulated in the literature to account for the variety of bedform patterns observed. In the idealized cases of sand ripples generated by constant currents and orbital ripples generated by purely oscillatory flow, distinctly different mechanisms of formation are observed. This distinction blurs for anorbital ripples and ripples under combined wave-current flows such as evanescent ripples. The distinction in formation mechanism is suggested by cross-sectional profiles of the ripples. Current ripples are characterised by a much larger slope on the lee (or downstream) side. This difference is less distinct in the case of sub-orbital and anorbital ripples, in which the lee sides of the ripples become steeper but alternate as the flow switches back and forth in each wave cycle. Thus both current-induced ripple formation and wave-induced ripple formation are reviewed here.

1.3.1 Ripples under Symmetrical Waves

Sinusoidal waves produce symmetrical ripples. The onset of ripple formation has been observed at low wave amplitude as rolling grains collecting into strips of low height. Mean drifts are set up around these strips (or any bottom irregularity). The time average of these drifts is in the direction of the crests of the strips. Under most conditions the crests grow further. At a certain height (typically around 0.1λ) vortices start to shed from the crests. These vortices scour and deposit sand with a spatial regularity close to the nearbed orbital diameter of the wave motion hence the title orbital, or vortex ripples. Under ideal conditions such as those found in an oscillating water tunnel, the height of these ripples grows until the slopes of the ripples reach the sand's angle of repose and the crest to crest length λ grows to $1.3a$. Typically, in fully developed vortex ripples, the crests are long, straight and transverse to the wave direction. Most investigators refrain from discussing the mechanism causing

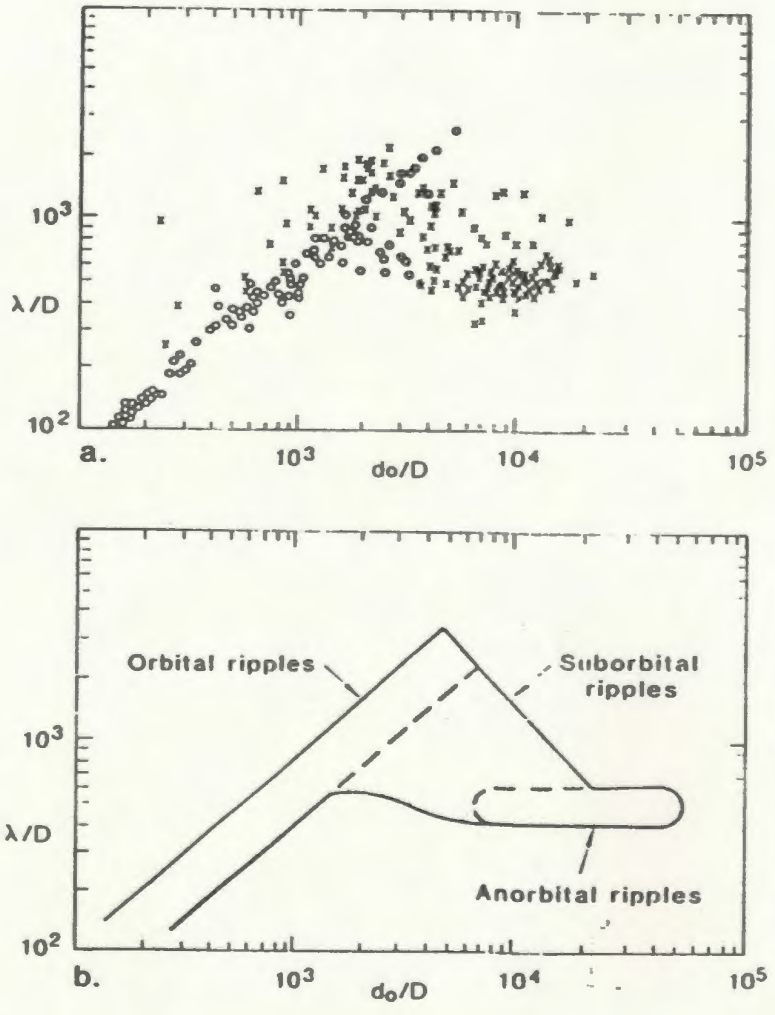

Figure 1.2: The variation in ripple crest-crest length λ with wave orbital diameter $2a$ (from Clifton and Dingler 1984). Plot (a) shows data from various sources. Circles denote data from laboratory studies, crosses are field data points. Plot (b) shows Clifton's nomenclature applied to the data. In both plots λ and $2a$ have been non-dimensionalized by dividing by the median sand grain size for the given data (see the section on dimensional analysis below for more detail).

the ripples to grow into long straight crests, but it appears to be a consequence of the growth of the ripples in height, then sand slipping down the sides of the ripple transverse to the flow direction, and then the ripple growth mechanism acting on those avalanched grains on the next wave such that a single bump grows into a long crest.

There are two exceptions to the long-crested ripple formation for oscillatory ripple growth. Bagnold (1946) noted that for orbital diameters less than one sixth of the maximum crest to crest spacing, the ripples formed a regular "brick pattern". Sleath (1984) noted that this pattern was stable for somewhat larger orbital diameters with somewhat less regularity in the ridges transverse to the flow. Sleath speculated that the formation mechanism for the brick pattern is related to the breaking up of the vortex shed by the ripple crest into "horseshoe" type vortices which may be more dynamically stable.

The other exception is the irregular, or brick pattern ripples described in detail by Lofquist (1978) and Southard et al. (1990). Lofquist noted that if the peak flow velocities exceeded a certain value (which was a function of the sand grain size) ripple crests broke into shorter and shorter crest lengths. This effect appeared to be independent of orbital diameter (with the requirement that period be decreased with increasing diameter to maintain a constant peak velocity). Though Lofquist and Southard refrain from speculating on the cause of this change in bedform pattern, evidence from the modelling portion of this thesis indicates that the balance between erosion and deposition of sand on transverse slopes may play a role. The influence of wave directionality on ripple pattern was checked in a multi-directional wave basin by Willis et al. (1993). They describe producing linear long-crested or intermediate-crested ripples using short crested waves and with uni-directional, long-crested waves, with wave short-crestedness having minimal effect on bedform pattern.

1.3.2 Ripples under Constant Currents

Though much studied, the mechanism of formation of current ripples is not completely understood. A recent review of current ripple formation has been given by McLean (1990). Once again flat beds under shear become unstable at some critical flow speed, but current ripples do not have a characteristic length scale imposed on them by the water motion. Small irregularities in the bottom cause variations in the shear stress exerted on the bottom. Because of the shear in the boundary layer, the location of the maximum bottom stress tends to be on the upstream side of the irregularity, rather than at the crest. The sand grains under the maximum bottom shear stress are preferentially dislodged, settling downstream in an area of lower bottom shear stress. When they settle, they add to the height of this down-stream location, which then has increased bottom stress, and the hopping process starts again (not necessarily with the same grains).

At increased flow speeds the flow separates at the crests of the ripples. This provides an additional stability mechanism, as the point of maximum bottom shear stress is moved from the crest of the ripple to the point of re-attachment downstream. In finite depth flow and still higher flow speeds, larger scale bedforms, often three dimensional in plan view and commonly called dunes, can be formed. Dune crest to crest length and height have been successfully modelled using simplified bottom boundary layers which cause a lag in the relationship between sediment transport and bedform height (Kennedy 1969). Dune size is also dependent on the depth of the flow. McLean and Smith (1986) showed good agreement between experiment and a theory that takes into consideration the wakes of the dunes interacting with the water surface to enhance a periodic variation in flow speed, and hence bottom shear.

1.3.3 Ripples Under Combined Waves and Currents

In combined wave-current flows very little theoretical work about bedform formation has been done. Bedforms are caused by bed shear stress, and there are several

competing theories to estimate the bed shear stress under combined waves and currents, such as Grant and Madsen (1979) and Sleath (1991). However, observations such as those of Amos et al. (1988) and Li and Amos (1995) indicate that the bed does not simply adjust to the net shear strength and direction. Rather, in flows with both current and wave action, wave induced bedforms and current induced bedforms coexist. Sleath (1984) summarized laboratory results for collinear currents and waves, and concluded that wave mechanisms dominate the ripple height and crest-crest length for current velocities up to 50% larger than maximum wave velocities, while the ripple profile becomes asymmetrical at much smaller current velocities. These results have been reinforced by the wave tunnel results of Arnott and Southard (1990).

1.3.4 Wave Ripples Under Field Conditions

The mechanism of formation of sand ripples in field conditions has been assumed to be similar to that observed in the laboratory. There are several features of field conditions which have not typically been simulated in the laboratory which cause differences between laboratory and field results.

Wave irregularity makes comparison between laboratory ripple studies (which normally use regular waves) and field studies difficult. Miller and Komar (1980a, 1980b), Nielsen (1981), and Wiberg and Harris (1994) compared ripple dimensions as measured by various authors in both field and laboratory and found that using 'significant' wave height (defined as the average of the highest third of the waves) as a measure of the irregular waves found in the field provided the best agreement with laboratory measurements of ripple size, initiation, and obliteration into flat bed. Recent laboratory studies by Sato and Horikawa (1988) and Ribberink and Al-Salem (1990) compared results obtained by driving flow in an oscillatory flow tunnel with either sinusoidal or irregular flows. Both of these studies found that the bedforms found under irregular forcing compared favourably with field results, whereas under sinusoidal forcing, only vortex ripples were created.

Sand grain size non-uniformity is often not discussed in the published results of

either field or laboratory studies, yet sand grain size is an important determining factor in ripple properties, and sand in the field is likely to be more heterogeneous than sand in the laboratory. Sand grain size heterogeneity has been studied in current ripples, and has been found to play a significant role (see, for example, Gilley, Kottwitz and Wieman 1992). Overall bed slope has also been shown to have an effect on current generated ripples. In field studies waves have a directional spread, which may influence whether ripples form in linear or brick pattern (Sleath, 1984).

In this study, the variables of wave irregularity, wave directionality, and sand size heterogeneity have been controlled by comparing field results with almost one-to-one scaled laboratory results. Nevertheless, the range of different conditions observed in this study was limited by experimental considerations, hence conclusions about the mechanisms associated with these field variables await more data. However, a distinct mechanism contributing to the crossed ripple set pattern formation has been found in this present study. This mechanism also appears to be capable of forming regular ripples, irregular ripples, and lunate forms.

1.3.5 Cross-Ripples.

Previous theories about the mechanisms of formation of cross-ripples are largely speculative. Clifton (1976) suggests that cross-ripples could be formed by uni-directional waves with asymmetrical on-offshore velocity. The greater velocity in the on-shore portion of the wave cycle creates helical vortices which appear to be shed at intersections of the two sets of crests. Allen (1982) suggests several other possibilities, including reflected obliquely incident waves, and an amplification of the short-crestedness of the wave field due to shoaling.

Previous laboratory observations of cross-ripples are also few. Hay and Wilson (1994) and Wilson and Hay (1995) describe cross-ripples and lunate megaripples as observed in the Wave Research Flume at the National Research Council in Ottawa, Canada. Even under the close to ideal conditions of the wave flume, the vigorous forcing conditions necessary to produce cross-ripples generate sufficient suspended

sand concentration to obscure the bed, making it difficult to make even qualitative visual observations which might suggest formative mechanisms. Nevertheless, the fact that cross-ripples occur in the wave flume under unidirectional waves and no longshore current negates wave and current directionality as principal formative mechanisms. Cross-ripples were observed under regular, grouped, and irregular waves, indicating that irregularity and bound group waves are not principal formative mechanisms. The fact that cross-ripples have not been reported in previous wave tank or oscillating water tunnel studies suggests that the scale of the tank and some difference in wave flume and water tunnel flows is significant. Also the fact that cross-ripples have not been reported in deeper waters (even though flat bed has been observed) suggests that the skewness or asymmetry of the wave motion may play a role in cross-ripple formation.

The central hypothesis of this thesis is that the formation of cross-ripples can be explained in terms of a self-organisation mechanism. In this self-organisation, the ripple forms deflect the sand moving along the bottom diagonally from the flow lines, and that sand is preferentially deposited along diagonal lines, so that the diagonal, diamond shaped pattern is self-reinforcing. The diamond pattern appears to be the dominant form under forcing conditions which are non-symmetrical. The water flow need not be deflected by the bedforms for this mechanism to work, as the sand is hypothesized to travel by ballistic trajectories which are influenced by the local bed slope and whether the slope is on the lee or stoss side of the bedforms. Variations in shear stress due to the patterns of flow over the bedforms are modelled implicitly by varying the amount of sand transported in each model time step as a function of bed slope.

1.4 Theory.

Ultimately, the physics of sand ripple formation is controlled by the stochastic movement of individual sand grains of irregular shape and size. These individual

grains are influenced by fluid flows which are accelerating and non-uniform in time or space, and are often turbulent or quasi-turbulent. Thus any analytical treatment of the formation of sand ripples requires that simplifying assumptions be made. Theoretical treatments often start by applying dimensional analysis to the problem. These dimensional arguments can be used to characterise field and wave tank observations, and can be used to determine scaling parameters for theoretical models.

Theoretical models for ripple initiation and growth come under four general categories; instability theory, semi-empirical fits to existing data, simplified flow models, and sand self-organisation models. The first three classes of models apply almost exclusively to uni-directional or pure oscillatory flows creating two-dimensional ripples. They calculate the fluid motions in detail, but have very simple assumptions about the sand motion. The self-organisation models have simplified flow assumptions, and treat the stochastic nature of the sand movement explicitly. An advantage of self-organisation models is that they can be driven by arbitrary forcing, hence this model type was adopted for this study.

1.4.1 Dimensional Analysis.

Dimensional analysis has been applied to the question of bedform size using various combinations of variables. Typically seven variables are identified as contributing to the problem (Yalin 1977), hence a property Q of the bedforms (such as ripple height or crest-crest length) may be described as

$$Q = f_Q(\rho, \mu, U_m, 2a, D, \rho_s, g), \tag{1.1}$$

where ρ and ρ_s are the densities of the water and sediments, μ is the molecular viscosity, U_m is the maximum orbital velocity, $2a$ is the near-bottom orbital diameter, and g is gravity. Note that in this parameterization the dependence on wave period is implicit in the combination of U_m and $2a$. D is the mean or median grain diameter, which is applicable for well sorted sand of fairly uniform shape. The quartz beach sand in the experiments presented here fits this description well.

A typical dimensional analysis yields

$$F_Q = F\left(\frac{U_m D}{\nu}, \frac{\rho U_m^2}{(\rho_s - \rho)gD}, \frac{\rho_s}{\rho}, \frac{2a}{D}\right). \tag{1.2}$$

The first of these parameters is the sand grain Reynolds number. The second is sometimes referred to as the mobility parameter ψ, and is a measure of the ratio of horizontal force on the sediment to the vertical buoyancy force. It is sometimes written in terms of nondimensionalized bottom shear stress and is called the Shields parameter after Shields (1936). Jonsson (1966) related bottom shear stress τ_w to bulk flow velocity U_m through a friction factor f_w, such that $\tau_w = f_w \rho U_m^2/2$. Thus Shields parameter θ_s can be written

$$\theta_s = \frac{f_w \rho U_m^2}{2(\rho_s - \rho)gD}. \tag{1.3}$$

f_w has been determined experimentally by several researchers (a summary is available in Nielsen 1992 p26-29). The existing data has been shown to be fitted reasonably well by an equation given by Swart (1974);

$$f_w = \exp\left(5.213\left(\frac{2.5D}{a}\right)^{0.194} - 5.977\right) \tag{1.4}$$

which is applicable for rough turbulent boundary conditions such as those under which bedforms are formed. Note that Jonsson and Swart use $2.5D_{50}$ for the hydraulic roughness of the bed, where D_{50} is the median diameter of the sand.

The third parameter ρ_s/ρ is usually taken as constant for a given environment, thus leaving three free parameters.

As yet, there is no general agreement in the literature as to the formulation of each of these non-dimensionalized parameters. Other parameterisations can be found in Yalin and Russell (1962) and Mogridge and Kamphuis (1972). Typically others also come out with a single parameter which contains the central variables in Shields parameter, but with explicit dependence on wave period as well. Dingler and Inman (1974), and Nielsen (1981) leave out Jonsson's friction factor in the nondimensionalization of bottom stress, using ψ instead. Often, as in Clifton (1976), the

waves are assumed to be sinusoidal, hence orbital diameter $2a$ is a simple function of maximum velocity u_m or vice-versa. Clifton, however, would add a parameter Δu_m to describe the asymmetry in the wave forcing, and Allen (1982) would add directions for the components of U, with the components not necessarily in phase. In this study surface height and velocity skewness, asymmetry and wave directionality can be measured directly, and these will provide non-dimensional measures of wave asymmetry and directional variability, as discussed in the results section.

1.4.2 Instability Theory.

Two-dimensional linear stability analysis has been applied to the ripple initiation and growth problem by several researchers, notably Kennedy (1969), Richards (1980) for current ripples, and by Sleath (1978) and Blondeaux (1990) for wave induced ripples. In these theories, the equations for the flow are linearized around a bed height or bed slope parameter. To calculate the bed shear, the flows are either assumed laminar, or the boundary layer is modeled using a turbulence closure scheme (McLean and Smith 1986), and sand movement is estimated according to a semi-empirical relationship such as: $q_b = C(\tau_o)^m$ where q_b is sand flux, τ_o is shear stress at the bed, and C and m are constants.

According to simple linear instability theory sand beds under waves or currents are unstable at all wavelengths of ripple growth. Due to the linearising approximations made, ripple prediction using instability theory is only successful during the early stages of ripple growth from initially flat conditions, or for describing "rolling grain ripples" as discussed in Blondeaux (1990). Linear instability theory does not explicitly consider the vortex shedding which occurs in larger amplitude, more developed ripple fields. However, Vittori and Blondeaux (1990, 1992) have extended the method using weakly non-linear analysis to follow the growth of the most rapidly growing ripple components to the point at which the ripple height is finite. Vittori and Blondeaux (1992) found that allowing an additional perturbation in the crest parallel direction resulted in a brick pattern ripple field under wave conditions in which the maximum

velocity U_m was greater than some threshold value. This corresponds to the second type of brick pattern as is observed in field data (including ours) and the laboratory data of Sleath (1990) and Lofquist (1978).

1.4.3 Semi-Empirical Theories.

Semi-empirical theories have been developed as practical aids for ripple size prediction, and can only handle relatively simple wave and bottom conditions. As suggested in the previous section on dimensional analysis, using simplifying assumptions such as the small amplitude wave approximation and uniform sand, functions of the ripple properties can be reduced from four independent variables to one dominant one. Nielsen (1981) and others use non-dimensionalized parameters such as Shield's parameter θ or mobility parameter ψ. As demonstrated in Figure 1.2, when plotted against one parameter there is quite a lot of scatter in the data from various sources.

Nielsen (1981) concluded that separate empirical fits were necessary for laboratory and field results. For laboratory results, equations for ripple crest-crest length (non-dimensionalized by wave orbital semi-excursion a) and ripple height η were given as

$$\lambda/a = 2.2 - 0.345\psi^{-0.34} \tag{1.5}$$

$$\eta/a = 0.275 - 0.022\sqrt{\psi}, \tag{1.6}$$

and under irregular field waves

$$\lambda/a = \exp\left(\frac{693 - 0.37\ln^7\psi}{1000 + 0.75\ln^8\psi}\right) \tag{1.7}$$

$$\eta/a = 21\psi^{-1.85}. \tag{1.8}$$

In these equations Nielsen found a better fit to the available historical data using ψ. However, the Jonsson friction factor does not change very much over the data range described by Nielsen, so in the present study the use of Shields parameter has been retained.

Wiberg and Harris (1994) approached ripple size prediction using the orbital, suborbital, and anorbital ripple classification scheme. After sorting the available data in the literature to exclude relict ripple forms, Wiberg and Harris obtained the relationships for ripple crest-crest length λ for orbital (or vortex) ripples and anorbital ripples as

$$\lambda_{orb} = 0.62(2a), \tag{1.9}$$

$$\lambda_{ano} = 535D, \tag{1.10}$$

and estimated the crest-crest length for suborbital ripples by using a weighted geometric average of λ_{orb} and λ_{ano},

$$\lambda_{sub} = \exp\left[\left(\frac{\ln(2a/\eta_{ano}) - \ln(100)}{\ln(20) - \ln(100)}\right)(\ln\lambda_{orb} - \ln\lambda_{ano}) + \ln\lambda_{ano}\right]. \tag{1.11}$$

The ripple heights are estimated for orbital ripples by

$$(\eta/\lambda)_{orb} = 0.17, \tag{1.12}$$

and for suborbital and anorbital ripples by

$$\frac{\eta}{\lambda} = \exp\left[-0.095(\ln\frac{2a}{\eta})^2 + 0.442\ln\frac{2a}{\eta} - 2.28\right]. \tag{1.13}$$

This equation must be solved iteratively.

The Wiberg-Harris criterion for determining which ripple type will occur for a given wave climate is based upon estimates of whether ripple height is greater than the wave boundary layer thickness. To estimate this, the anorbital ripple height is calculated, and it is argued that the wave boundary layer thickness is proportional to orbital diameter, so that for $2a/\eta_{ano} < 20$ orbital ripples are formed, for $2a/\eta_{ano} > 100$ anorbital ripples are formed, and for values of $20 < 2a/\eta_{ano} < 100$ sub-orbital ripples are formed. In application, η_{ano} is calculated first using λ_{ano}, then the ripple type criteria is applied, and the final ripple crest-crest length and height are calculated using the appropriate equation.

1.4.4 Simplified Flow Models.

The simplified flow models of McLean and Smith (1986) for unidirectional ripples and dunes and Fredsøe and Brøker (as described in Fredsøe and Deigaard 1992) for oscillatory flows combine empirical observations from flow separation studies over a backward step with a simplified model of bed shear stress. In the Fredsøe-Brøker model the assumption of no net sand movement is also made. The simplified bed shear stress is averaged over a wave cycle, then balanced against the component of gravity tangential to the bed. The Fredsøe-Brøker theory predicts ripple heights reasonably well for a given ripple length in the two dimensional case, and explores the underlying physics. Ripple lengths can also be obtained by making assumptions about dominant ripple growth rates. The concept of modelling separated flow in a simple manner has been used in the self-organised sand model computer simulation developed in this work.

1.4.5 A Self-Organised Sand Transport Model.

In the models discussed above, sand is modelled as a continuum, with sand motion not modelled directly (being assumed to move much slower than the water movement). In higher energy flows sand moves largely by saltation and suspension (see, for example Wiberg and Smith 1985). Thus to obtain a mechanism for three dimensional bedform generation under arbitrary wave conditions, a saltating sand model originally derived to describe aeolian sand dune formation by Nishimori and Ouchi (1993) was modified for near shore sub-aqueous sand ripple simulations. The model of Nishimori and Ouchi is intentionally very simple to elucidate the principal mechanisms of aeolian sand ripple formation. This simplicity has been retained in the version described in this study.

There are two fundamental features of the model. The first feature is movement of sand by discrete distances, which can be associated with the saltation mechanism, and the second feature is gentle smoothing of the sand bed, which can be associated with the redistribution of sand grains by the multiple impacts of the saltating grains.

The sand bed is modelled by a relatively coarse (compared to sand grain size) two dimensional rectangular grid of field variables which represent the average surface height $H(x_i, y_j)$ at each grid point x_i, y_j (the subscripts i, j have been used to represent the discrete nature of x and y). Periodic boundary conditions are used in both x and y directions.

Bedform evolution is observed by stepping the model forward in time. The fundamental mechanism of ripple formation in the model is a self-organisation of sand grains as time progresses. Small piles of sand grains influence the distance and amount of sand moved from a given pile in a systematic way, which produces other piles until bedforms fill the simulation domain. Any possible feedback to the fluid flow is ignored, so secondary flow patterns that might be induced by the ripples do not contribute to the ripple patterns produced by the model.

The Nishimori-Ouchi model was originally presented in two sub-types. The type I model used a scalar (bed elevation) as the criterion for quantity of erosion and distance of transport per time step. This simulated small scale aeolian ripple conditions with sand motion only in the direction of forcing by the wind. This model always produced long-crested ripples. The type II model used a vector (the bed slope) as a criterion for quantity of erosion and distance of transport in both transverse and along-flow directions. This bedslope criterion is a very simple parameterization of both variation of shear stress across the bedforms and variation in the trajectories of the sand grains due to gravitational effects (Fredsøe and Deigaard 1992). Nishimori and Ouchi produced crescentic shaped bedforms (barchan-type dunes) with the type II model. It is the type II model which was modified for use in this study.

1.5 Wave Analysis

As discussed in the section on dimensional analysis, the principal wave parameters of interest with respect to sand bedform formation are the maximum velocity U_m and the orbital diameter $2a$. Though considerable effort has gone into collapsing the

available data onto a single curve (see for example, Yalin and Karahan 1978, Nielsen 1981, Wiberg and Harris 1994), thus far combinations of the parameters discussed in the section on dimensional analysis only account for some of the variability in the ripple data. As discussed previously, many other wave properties may play a role in sand ripple formation. Thus eight other parameters have been extracted from the wave data in this study: mean longshore and cross-shore currents, the Longuet-Higgins directionality factor (Longuet-Higgins 1957), long-shore and cross-shore infra-gravity frequency band wave velocities (i.e. low frequency wave motions below wind wave frequencies, generally taken to be below 0.04 or 0.05 Hz), velocity skewness and asymmetry as defined below, and differences in maximum onshore and offshore flow velocities Δu as suggested by Clifton (1976). Clifton (1976) suggested the non-sinusoidal nature of the waves was the cause of cross-ripple and other asymmetric bedforms. Results from the calculation of Δu have been listed and plotted along with skewness and asymmetry in the results section to demonstrate the utility of this variable in characterizing the non-sinusoidal nature of the wave field.

Directional spectra were also calculated for the Burley Beach field data to determine if there was a relationship between the incoming direction of various frequency components of the waves and cross-ripple orientation directions. A single parameter describing the width of the incident wave direction variability is Longuet-Higgins' wave directionality factor (Longuet-Higgins 1957). Descriptions of the methods of calculation and sample results have been included in the Appendix.

Measures of Wave Asymmetry

The mathematical groundwork for describing wave skewness and asymmetry was laid in the 1950s when Oceanographers started studying the statistical properties of surface gravity waves. Higher moment statistical analysis of the ocean surface by Longuet-Higgins in several papers in the 1950s led to the description of 'skewness' of the wave surface being related to the peaked nature of the wave profile. Hasselmann et al. (1963) applied Fourier transforms to waves, and found that the phase of the

transform of the third order moments of the wave heights described differences in the leading and lagging surface slopes of the waves (how similar the wave profile is to a "sawtooth" shape) and defined this as wave 'asymmetry'.

For a time series of surface elevation ζ, skewness is defined as

$$S = \frac{\frac{1}{n}\sum_{i=1}^{n}(\zeta_i - \bar{\zeta})^3}{(\frac{1}{n}\sum_{i=1}^{n}(\zeta_i - \bar{\zeta})^2)^{3/2}} \tag{1.14}$$

where $\bar{\zeta}$ is the mean water surface elevation, $\bar{\zeta} = \sum_{i=1}^{n}\zeta_i/n$. Similar definitions can be employed for velocities u and v. Skewness can also be defined in terms of the third order terms in the frequency domain, or bispectral components. For the purposes of this study, the definitions of Elgar and Guza (1984) have been used. The Fourier transform of the time series of surface elevation ζ is given as

$$\zeta(x,t) = \sum_{n=1}^{N} \mathcal{A}_n e^{i(k_n x - \omega_n t)} + \mathcal{A}_n^* e^{-i(k_n x - \omega_n t)} \tag{1.15}$$

where the ω_n and k_n are the component frequencies and wave numbers. $\mathcal{A}_n$ and $\mathcal{A}_n^*$ are the Fourier coefficients. The auto-bispectrum is formally defined as the Fourier transform of the third order correlation function C of the time series such that

$$\mathcal{B}(\omega_1,\omega_2) = \left(\frac{1}{2\pi}\right)^2 \int_{-\infty}^{\infty}\int_{-\infty}^{\infty} C(\tau_1,\tau_2) e^{-i\omega_1\tau_1 - i\omega_2\tau_2} d\tau_1\tau_2, \tag{1.16}$$

where the correlation function coefficients are defined as

$$C(\tau_1,\tau_2) = E\left[\zeta(t)\zeta(t+\tau_1)\zeta(t+\tau_2)\right], \tag{1.17}$$

where E is the expectation, or averaging, operator. In the case of discrete sampled data with discrete spectra, the bispectrum coefficients can be calculated using the Fourier coefficients from 1.15,

$$\mathcal{B}(\omega_i,\omega_j) = E\left[\mathcal{A}(\omega_i)\mathcal{A}(\omega_j)\mathcal{A}^*(\omega_i+\omega_j)\right]. \tag{1.18}$$

Skewness S is defined as the integral over the real part of $\mathcal{B}$, which in discrete Fourier space can be calculated by

$$S = \frac{12\sum_{i>j}\sum_j \mathrm{Re}[\mathcal{B}(\omega_i,\omega_j)] + 6\sum_i \mathrm{Re}[\mathcal{B}(\omega_i,\omega_i)]}{E\left[\zeta^2\right]^{\frac{3}{2}}} \tag{1.19}$$

where in the sum $i > j$ indicates that only those terms $\mathcal{B}(\omega_i, \omega_j)$ in which $i > j$ are included in the sum, and Re signifies the real part.

The asymmetry can likewise be defined as the integral over the imaginary part of $\mathcal{B}$. In terms of the imaginary parts of the discrete bispectrum coefficients,

$$A = \frac{12 \sum_{i>j} \sum_j \mathrm{Im}[\mathcal{B}(\omega_i, \omega_j)] + 6 \sum_i \mathrm{Im}[\mathcal{B}(\omega_i, \omega_i)]}{E\left[\zeta^2\right]^{\frac{3}{2}}}. \tag{1.20}$$

The cross-power spectral moments Φ_{ij} required by the directional spectral analysis can now be defined as

$$\Phi_{ij}(\omega) = E\left[\mathcal{A}_i(\omega)\mathcal{A}_j(\omega)\right] \tag{1.21}$$

where $\mathcal{A}_i$ and $\mathcal{A}_j$ refer to the Fourier components of signals i and j.

Clifton suggested a different measure of wave asymmetry based on the difference between peak on-shore and off-shore velocities. In an irregular wave field the peak velocities change in magnitude, period, and direction for every wave, but in the nearshore region the waves tend to be nearly shore-normal due to refraction, and of a narrow frequency band, so an effective difference can be calculated as

$$\Delta u = u_{sig+} - u_{sig-}, \tag{1.22}$$

where u_{sig+} is the maximum on-shore velocity, and u_{sig-} is the absolute maximum off-shore velocity. For irregular waves the 'significant' wave velocities can be found by dividing the velocity record up into onshore and offshore components, then averaging the largest third of velocities in each direction. Another option is to sort the wave record into the waves with the highest third overall amplitude, then the onshore and offshore velocities from these waves can be averaged. A third approach is to take the difference of the means of the on-shore and off-shore components of the wave record. Each of these methods was tried, and gave similar results, with the difference of on-shore to off-shore significant velocities giving the largest differences.

Chapter 2

Experiments.

The experiments discussed in this thesis include the sediment transport study at Burley Beach in October 1992, a calibration study in the National Research Council Wave Research Flume in Ottawa, September 1993, and a second study in the Wave Research Flume in July 1995.

2.1 Equipment.

As mentioned in the Introduction, the bedform measurements in this study were made using a rotating head sonar unit with a fan-beam transducer. This sonar unit was mounted on a stationary frame and was connected to an on-shore computer and data acquisition system where it provided a continuously updated image of the bottom. Sensors for measuring wave height, cross-shore (x) and long-shore (y) velocities, and suspended sediment concentration were mounted on the same frame and on nearby frames. The data acquisition system includes a Simrad Mesotech Model 971 sonar head modified to operate at an acoustic frequency of 2.25 MHz, its controller, the RASTRAN data acquisition system (Hay et al. 1988), used to digitise and store image information, and Dalhousie University's UDATS system (Hazen et al. 1987).

2.1.1 The Sonar System.

The Mesotech 971 sonar system consists of two parts, the sonar head assembly which is deployed underwater, and the controller, which remains on shore. The sonar head consists of a waterproof housing for electronics and stepper motor, and the rotating transducer face which is driven by the stepper motor. For each angle step, the transducer emits a 10 microsecond long pulse at 2.25 MHz, then listens with a time varying gain to obtain the bottom return echo. A microprocessor in the housing controls the stepper motor, the driving circuit for the acoustic pulse, the receiver circuitry and time varying gain. The transducer is a rectangular piston of piezoelectric material, 5.0 cm long and 0.13 cm wide. The beam pattern from this transducer, as measured in the laboratory at a range of 60 centimetres is shown in Figure 2.1. It consists of a fan approximately 30 degrees wide in the vertical and 0.8 degrees wide (from 3 dB point to 3 dB point) in azimuth. The time varying gain in the receiver circuitry was necessary because the attenuation of sound in water is significant at 2.25 MHz.

The sonar head is connected by double armoured cable with coaxial signal line and power lines to the Mesotech 971 sonar controller. The sonar controller contains the analog circuitry needed to send commands to the sonar head over the signal line, and the circuitry to process the analog data returned by the sonar head and information about the direction the sonar head is pointing into an image. It also contains the necessary computer and video circuitry to display the data in a variety of formats on a video monitor in real time (i.e., while the data is being acquired). This display was converted to NTSC television format and recorded on VHS videotape. Our system was also factory modified to provide analog trigger out and signal lines which were used to digitise and store the data.

The data acquisition portion of the RASTRAN System I system (Hay et al. 1988) was used to digitise and store selected sweeps of the 971 sonar system. Trigger and signal lines from the 971 system were connected to the LeCroy 6810 waveform digitiser. The waveform digitiser was typically programmed to digitise 1350 samples

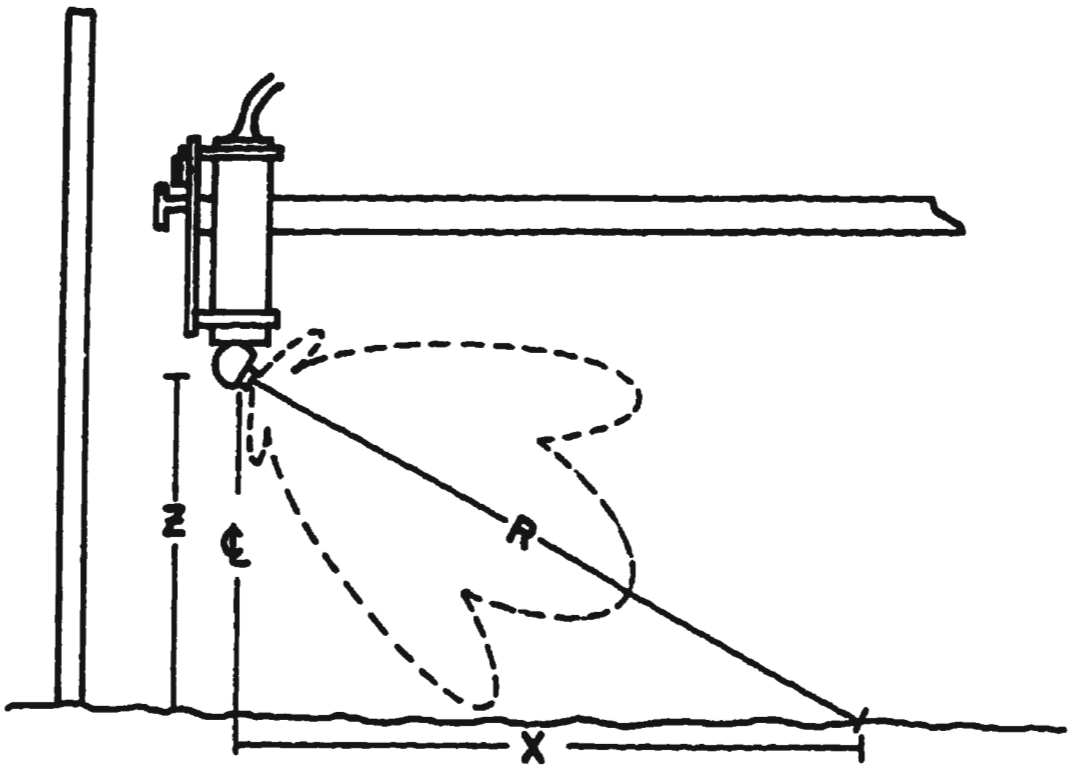

Figure 2.1: Field configuration of the Simrad Mesotech 971 Sonar Head. Also shown is the fan of the sound projection from the transducer face as measured at a range of 60 centimetres.

at 200 kSample/s (corresponding to a range of approximately 5 meters given a speed of sound in water of 1450 m/s) upon receipt of a trigger pulse. After digitising the return from a ping, the data were sent to the computer for averaging and storage. The data transfer, processing and storage took place quickly enough for the 6810 to be ready for the next trigger from the 971 system, approximately every 58 ms. The computer also had an OMEGA DAS-16 analog to digital board which was used to acquire eight channels of UDATS data after each waveform.

2.1.2 The UDATS System.

The Dalhousie UDATS system consists of multiple Marsh-McBirney model OEM512 electro-magnetic current meters (with 5 cm diameter spherical heads) and Model 1 OBS's (Optical Backscatter Sensors, which detect suspended sediments) connected to a pressure case which contains the electronics necessary to power the sensors and digitise their results (Hazen et al. 1987). The data acquisition and storage are controlled by an on-shore computer through RS232 serial communications lines. As the data come to shore already digitised, facility was made for a digital to analog conversion so that data could be re-acquired by the RASTRAN system. Sample rates for the Burley Beach experiment were approximately four samples per second. In the Ottawa 1993 experiment the sampling rate was approximately eleven samples per second. UDATS was not used in the Ottawa 1995 experiment due to technical difficulties and new acoustic techniques.

2.2 The Burley Beach Experiment

The Burley Beach field experiment was a collaborative effort between research groups from Dalhousie University, The University of Toronto, and Memorial University. Burley Beach is located in the southeast corner of Lake Huron, as shown in Figure 2.2.

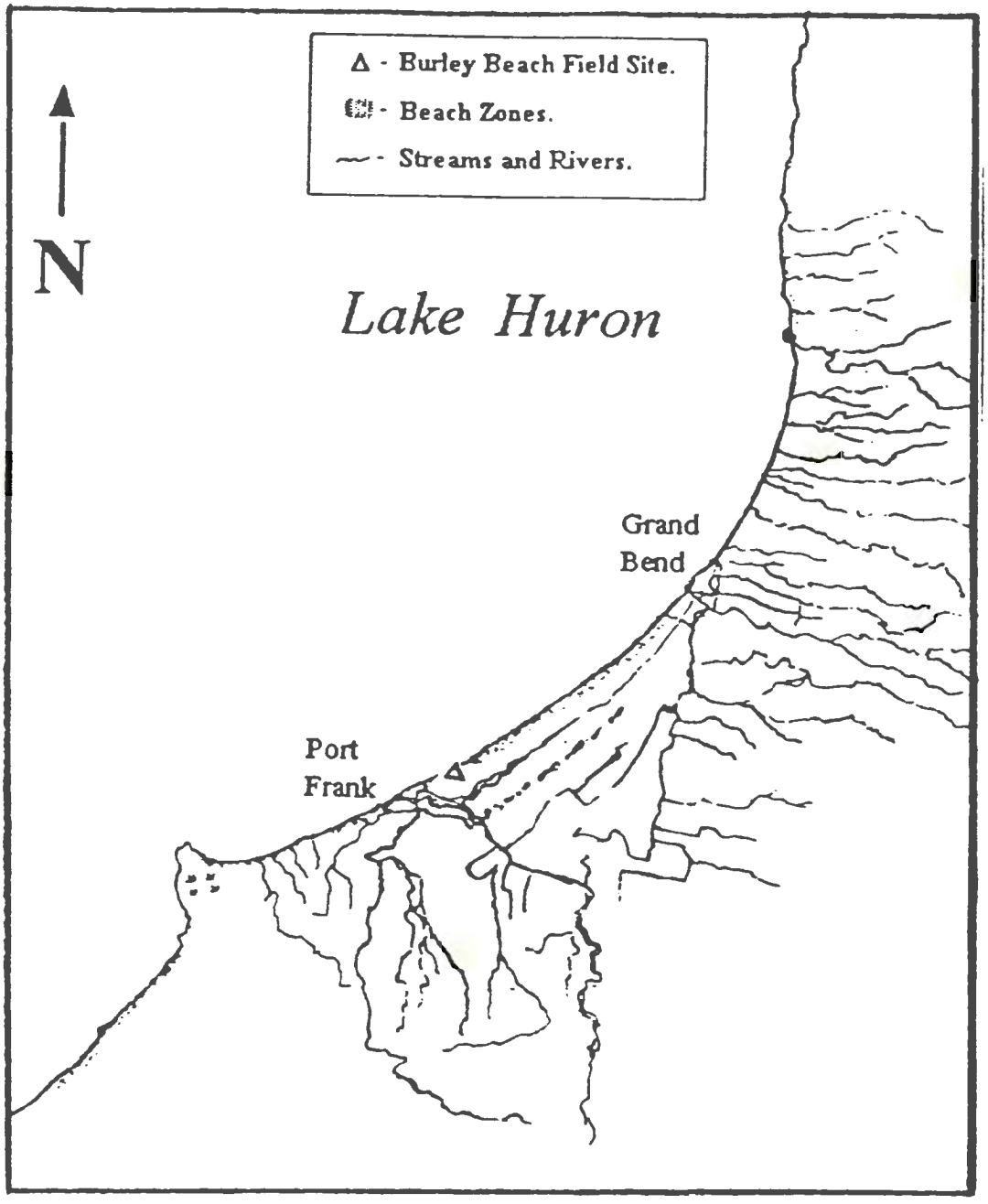

Figure 2.2: Map of Southeastern Lake Huron, showing Burley Beach and immediate area. Note the river mouths 1.2 kilometres southwest and 10.5 kilometres northeast of Burley Beach, which contributed significantly to water murkiness.

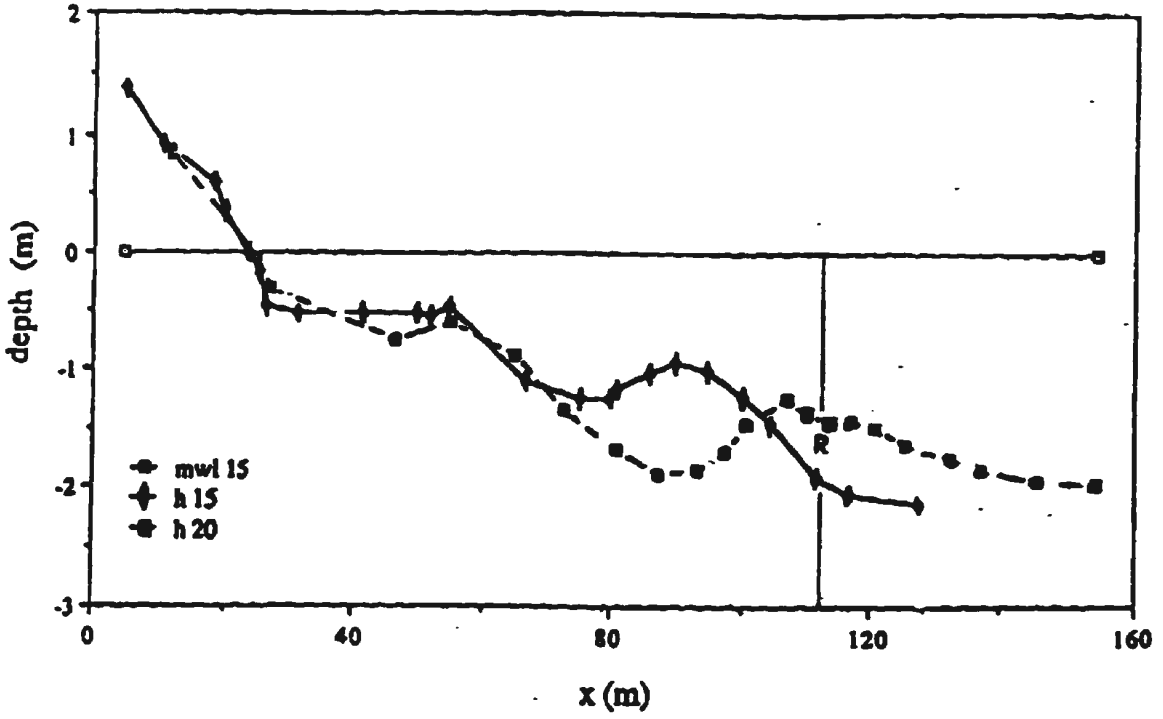

Figure 2.3: Cross-sectional profiles taken at the instrument line at Burley Beach, Ontario (Note exaggerated vertical scale). Diamonds are data from Oct. 15 (before data acquisition), squares are data from Oct.20 (after the first storm) showing the first two of the three bars. The horizontal line is the mean water level data from Oct. 15, and R is the RASTRAN instrument frame placement.

2.2.1 Burley Beach.

As shown in Figure 2.2, Burley Beach is a nearly straight coastline running south-west to northeast for approximately 10 kilometres. Figure 2.3 shows a cross-shore profile of the beach at the experiment site, with two well developed bars. A third bar (not shown) which was more of a broad undulation was located approximately 250 meters offshore. In October, 1992, the sand was moderately well sorted at the experiment site with a median diameter (D50) of 0.17 mm and a standard deviation of 0.05 mm. Surveyor observations indicated increasing sand size shore-ward of the experiment site below the water line, and a mixture of coarse sand and gravel at the shoreline.

2.2.2 Deployment of Apparatus.

The deployment location for the frame on which the Simrad Mesotech 971 sonar system was mounted was on the offshore side on the crest of the second bar, at approximately 1.8 meters depth (the position marked R in Figure 2.3). The frame was mounted approximately one meter above the bottom on four vertical posts. Each post had been jetted 2 meters into the sand to ensure stability. During the first storm, the bar moved twenty meters seaward, excavating some current meters, and burying others. The sidescan sonar was not buried completely, but the bed was so close at times that small surface features shadowed large areas. The posts and other instruments on the frame were clearly visible on the sidescan sonar image, and served as reference points throughout the experiment. The calm between storms two and three was used to raise the instrument frame, which had almost been buried in the shifting sand, and do minor repairs and checks on storm damaged equipment. The frame was raised 24 cm, and some erosion took place during the third storm such that the final distance to bottom was approximately sixty centimeters. A tilt meter mounted on the frame showed negligible frame movement throughout deployment.

2.2.3 Data Acquisition Protocol.

Data acquisition proceeded on a storm by storm basis, with data acquisition systems continuously monitored during storm events, and switched off between storms. The acquisition protocol consisted of four components: continuous videotaping of the Mesotech 971 controller screen; acoustical measurements of distance to bottom from four downward looking sonar heads every fifteen minutes, a suite of digitised acoustical measurements (including suspended sand concentration, bottom roughness, and digitised Mesotech 971 images) which were repeated hourly; and simultaneous operation of Dalhousie's UDATS system. The direct reading of the distance from the frame to the bottom was made with four downward looking sonar transducers pinging at 10 Hz. The signals from these transducers were observed on an oscilloscope, and the arrival time of the 100-ping average bottom return was recorded. The Simrad

Mesotech 971 controller was connected to the digitiser shortly after the distance to bottom measurement taken on the half hour, and several 360 degree sweeps of the bottom (sometimes up to 10 during interesting bed form events) were captured. Each sweep of the bottom took 47 seconds. Typically bedforms had not moved appreciably between sweeps, so that sequentially captured bed images could be averaged together. Current and pressure data were collected by the UDATS system typically 55 minutes out of every hour. In all, over 250 hours of data were collected. The protocol was switched to once every two hours when there was little change noted in the readings at the height of the storms and the calm periods near the end of the storms.

2.3 The Ottawa 1993 Wave Flume Experiments.

A second experiment took place in September 1993 in the 97 meter long Wave Research Flume of the National Research Council in Ottawa. The primary goal for the bedform portion of the study was to obtain sonar images of bottom bedforms under a variety of wave conditions, approaching those encountered in the field.

2.3.1 The Wave Flume.

The wave flume consists of a 2 meter wide by 2.7 meter deep channel with a 5 meter long Plexiglas walled test section near the middle. The wave paddle is hydraulically actuated and was operated in piston mode for all but one run, when hinged mode was tried. The wave absorber at the other end of the flume consists of multiple layers of expanded steel mesh which occupy the final 17 meters of the channel. The wave absorber was designed to reflect less than 5 % of the incident wave height for wave periods less than 5 seconds, and measurements indicated that considerably lower reflection coefficients were achieved for the 3.5 second period waves used in this experiment. The beach end of the flume can be opened up so that a front-end loader can be driven into the channel to move sand. For our experiments a ten meter long stretch of sand nominally 20 centimeters thick was placed from 2 meters before the

Plexiglas test section to 3 meters after. The median diameter of the sand (D50) was 0.095 millimeters. The advantage of having finer sand in the flume was that less wave energy was required to generate the bedforms, thus a greater range of bedform types could be observed. The water depth was set to 1.5 meters above the floor of the flume, i.e. approximately 1.3 meters above the sand bed.

2.3.2 Data Acquisition Protocol.

The general procedure at the NRC was to run the wave machine for two hours to allow the bedforms to stabilise. Then sonar data were acquired in a similar manner to that used at Burley Beach. Waves were made with three types of spectra: a modified natural sea wave spectrum (TMA modified JONSWAP time series), regular monochromatic waves, and regular bichromatic groups formed by the superposition of two sinusoidal signals of different period. Typical examples of time series of surface heights for the three different patterns are shown in Figure 3.15 of the Results section. The amplitudes were varied from near the onset of motion to the maximum that the wave maker could produce for all three types of wave spectra.

A time lapse video was set up to watch the bedforms through the Plexiglas side walls. Also the bed was measured and photographed each time the waves were turned off. A 25x25 cm grid of fine line was lowered onto the bedforms which the sidescan sonar was observing, and photographs were taken using lighting from various angles. Additional sonar images were also taken with the waves turned off, and for two different runs the whole instrument frame was tilted at various angles and sonar images were taken, to simulate sloping bottom conditions. In the final runs, (when conservation of sand was not such a priority) large amplitude waves were run to induce cross-ripples and megaripples. These runs were of shorter duration due to erosion of the bed (the sand was carried to the end of the tank) but because of the higher sand transport rates, cross-ripples and lunate megaripples formed quite well within the fifteen minutes of the run.

2.4 The Ottawa 1995 Wave Flume Experiments.

The experiment in July 1995 at the National Research Council in Ottawa was conducted in the same wave flume as the 1993 experiment. The same wave absorber was used as a beach, the same water depth, sand configuration, and similar types of waves were run. There were significant improvements in some of the equipment and data acquisition software for the 1995 experiment. Larger amplitude waves were possible, including waves which broke over the instrument frame. A larger sand size was thus possible, and the sand size chosen had a median diameter (D50) of 0.145 millimeters. In the 1995 experiment, the instrument frame was bolted directly to the walls of the wave tank, and was of considerably smaller cross-section in the flow directions. All instruments were also held in place well away from the supporting members of the frame by a section of radio tower, so that frame disturbances to the flow were kept to a minimum under the instrumentation. There were also virtually no surface piercing objects near the instrument frame, so that wave breaking would not be hindered or triggered.

A new, upgraded sonar controller was employed, and all new software acquired the data automatically. The angle of the sonar head was changed from 30 degrees below horizontal to 20 degrees below horizontal. This change meant some degradation in the data obtained within the first meter range along the bottom (as less sound reached this area) but a much improved evenness in the insonification of the rest of the range out to the five meter maximum.

Two other changes from the 1993 experiment worthy of note for the purposes of this study were the way in which wave measurements were made, and the data acquisition protocol for the 1995 experiment.

2.4.1 Wave Measurements

Wave heights were measured by an array of wave staffs as in the 1993 experiment, but velocity measurements were made with several acoustic Doppler velocity sensors

instead of Marsh-McBirney electro-magnetic current meters. The velocity data used in this thesis was obtained by a Sontek Acoustic Doppler Velocimeter (ADV). The sensing volume (of approximately one cubic centimetre) was positioned directly under the frame, approximately two meters towards the wave paddle from the rotary head sonar unit, and nominally ten centimetres from the bed. The system was set to sample at approximately 25 measurements per second, which were five sample bin averaged for an effective sample rate of five measurements per second.

2.4.2 Data Acquisition Protocol.

In the Ottawa 1995 experiment there were a total of 76 wave runs between 5 and 65 minutes long. Of these there were 32 which were of sufficient duration for the bedforms to be stable and for which there is sufficient wave and bedform data (either photographic or sonar image). A typical wave run consisted of starting waves, waiting for approximately a half hour or until the bedforms had changed to a new state, then acquiring wave staff and ADV data, and finally rotary sonar images as part of a suite of acoustic sediment transport measurements. As in the Ottawa 1993 experiment, waves were run in three basic patterns, regular, grouped, and irregular (TMA modified JONSWAP spectrum), with several different amplitudes each. These three wave patterns are illustrated in the results sectionin Figure 3.16. Wave groups were formed by modulating a 3.5 second wave train with a cosine taper function, and with a 30 second time gap between each group (to allow wave setup to relax). The JONSWAP type waves were also grouped, and for the highest energy runs the largest one or two waves in the sequence broke in the test section of the tank.

Chapter 3

Experimental Results.

The experimental results are presented in three sections, dealing with; bedform images from the fanbeam sonar and photographs; the associated current meter, pressure sensor, and wave staff results; and combined wave-bedform results. In each of these sections the results for the three experiments (Burley Beach, Ottlawa '93, and Ottawa '95) are discussed separately.

3.1 Sidescan Sonar Images.

3.1.1 Burley Beach Sidescan Sonar Images.

Six images of the bottom from the Burley Beach experiment are shown in Figures 3.1 through 3.6. These images were chosen to demonstrate the range of bedform types observed (with the exception of relict ripples, which have no specific pattern or appearance, but are defined rather by lack of sand movement on the bed). The data for these images have been dejittered and slant-range corrected as described in the Appendix. Each Figure consists of two images: the upper image is the full image with range rings every two meters; the lower image is an expanded view of a four meter by four meter square in the lower right quadrant of the full image, the location of which is denoted by the black square in the upper image.

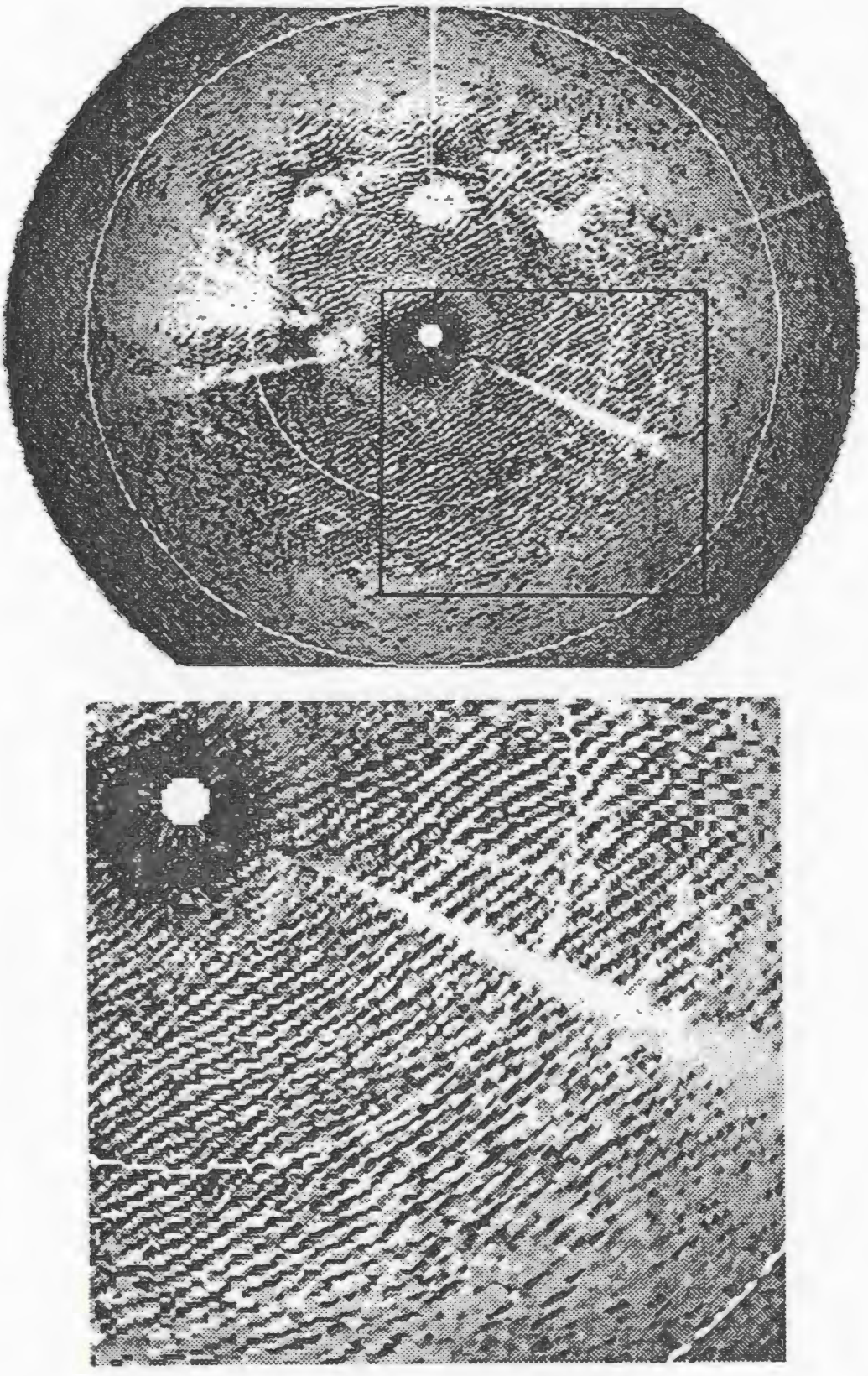

Figure 3.1: A sidescan sonar image of low wave energy linear ripple fields, taken at Burley Beach immediately before the third storm. The top of the page points offshore (NW). The white rings show range along the bottom of two meters and four meters from Sonar nadir. The lower image is an expanded view of the area denoted by the black box in the upper image. The Shields parameter and wave surface height skewness for this image were $\theta_s = 0.09$ and $S = 0.05$.

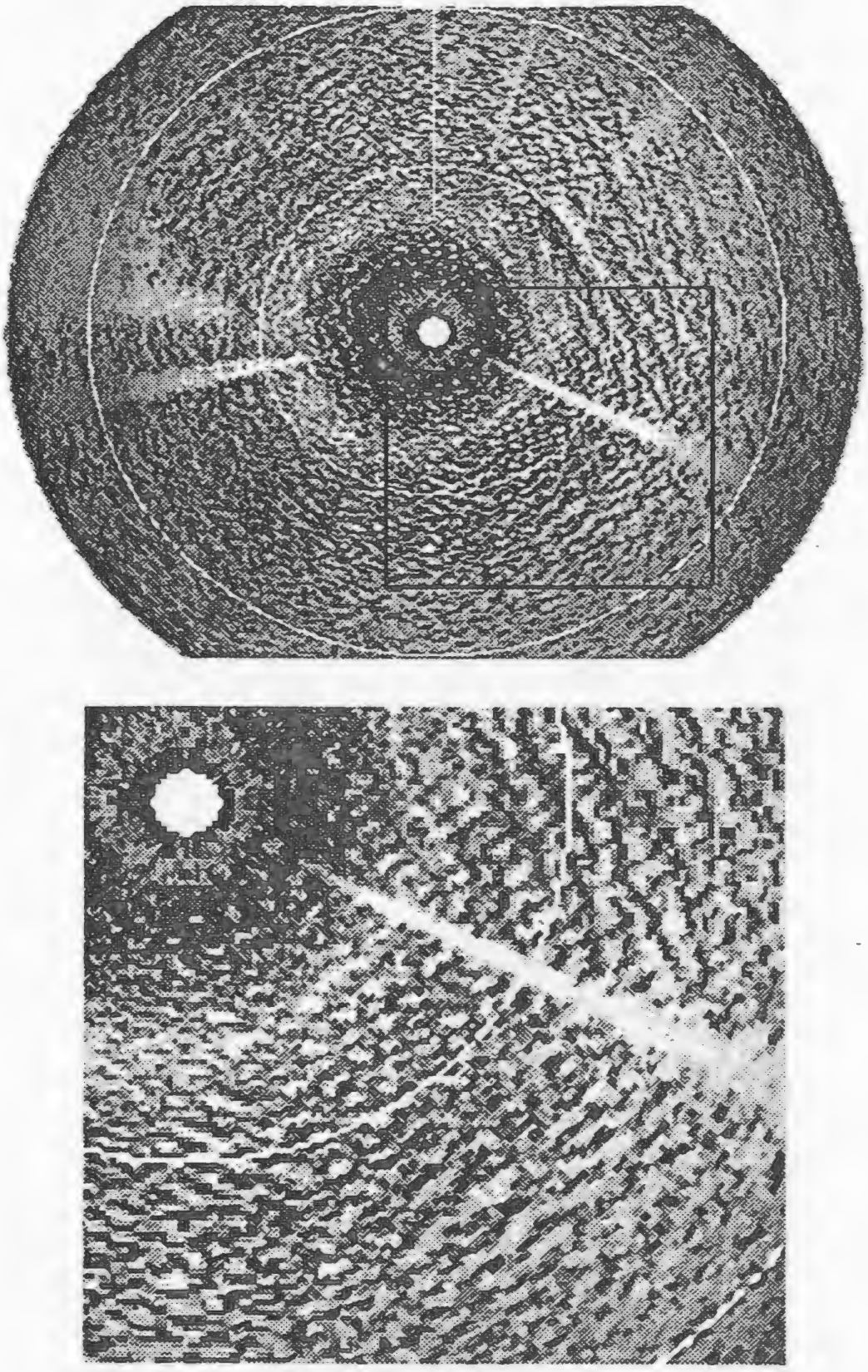

Figure 3.2: A sidescan sonar image of irregular ripples taken at Burley Beach near the end of the third storm. The Shields parameter and wave surface height skewness for this image were $\theta_s = 0.25$ and $S = 0.2$.

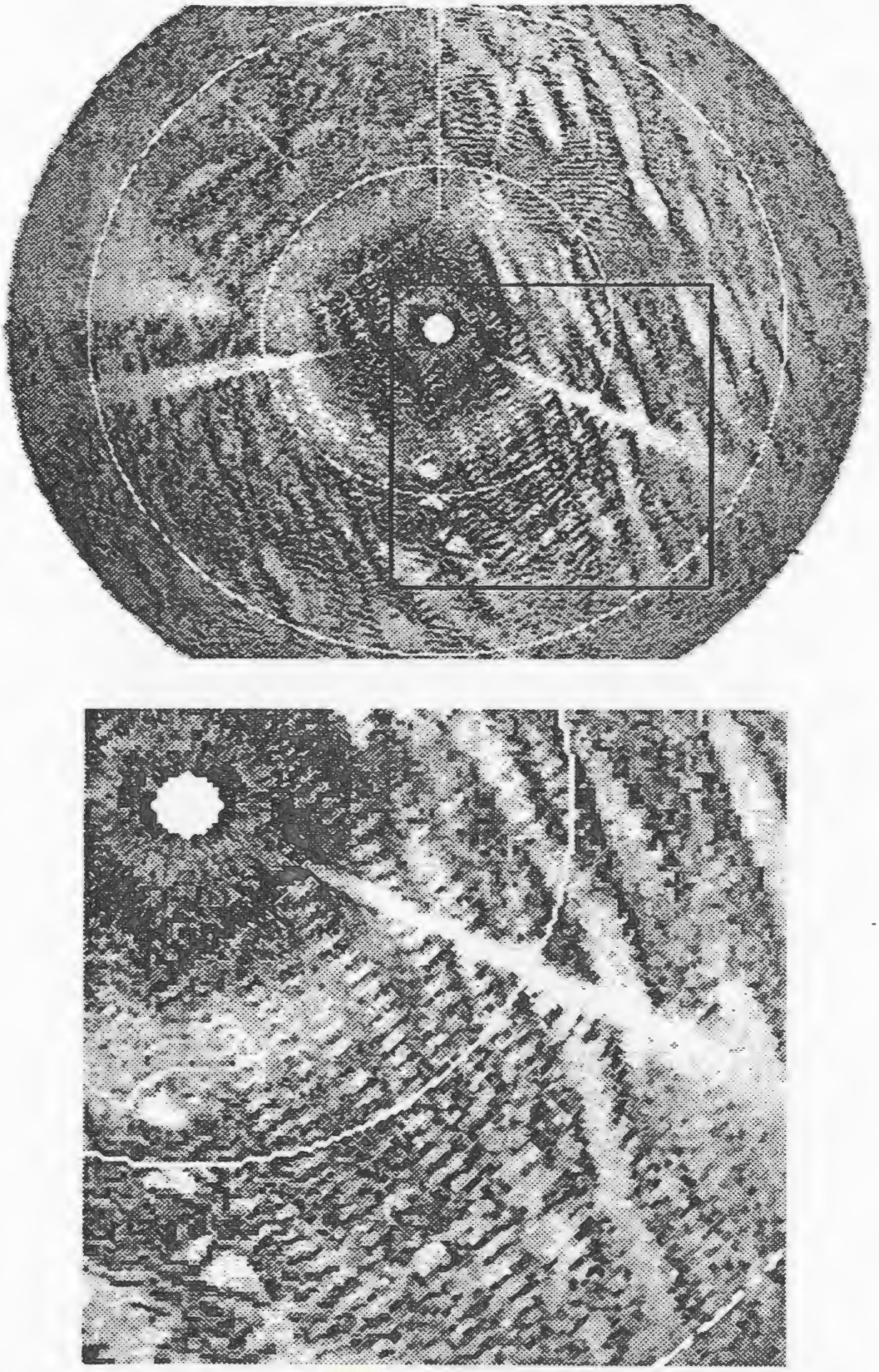

Figure 3.3: A sidescan sonar image showing cross-ripples, taken at Burley Beach two hours previous to the image in Figure 3.2. The wave parameters were $\theta_s = 0.50$ and $S = 0.30$.

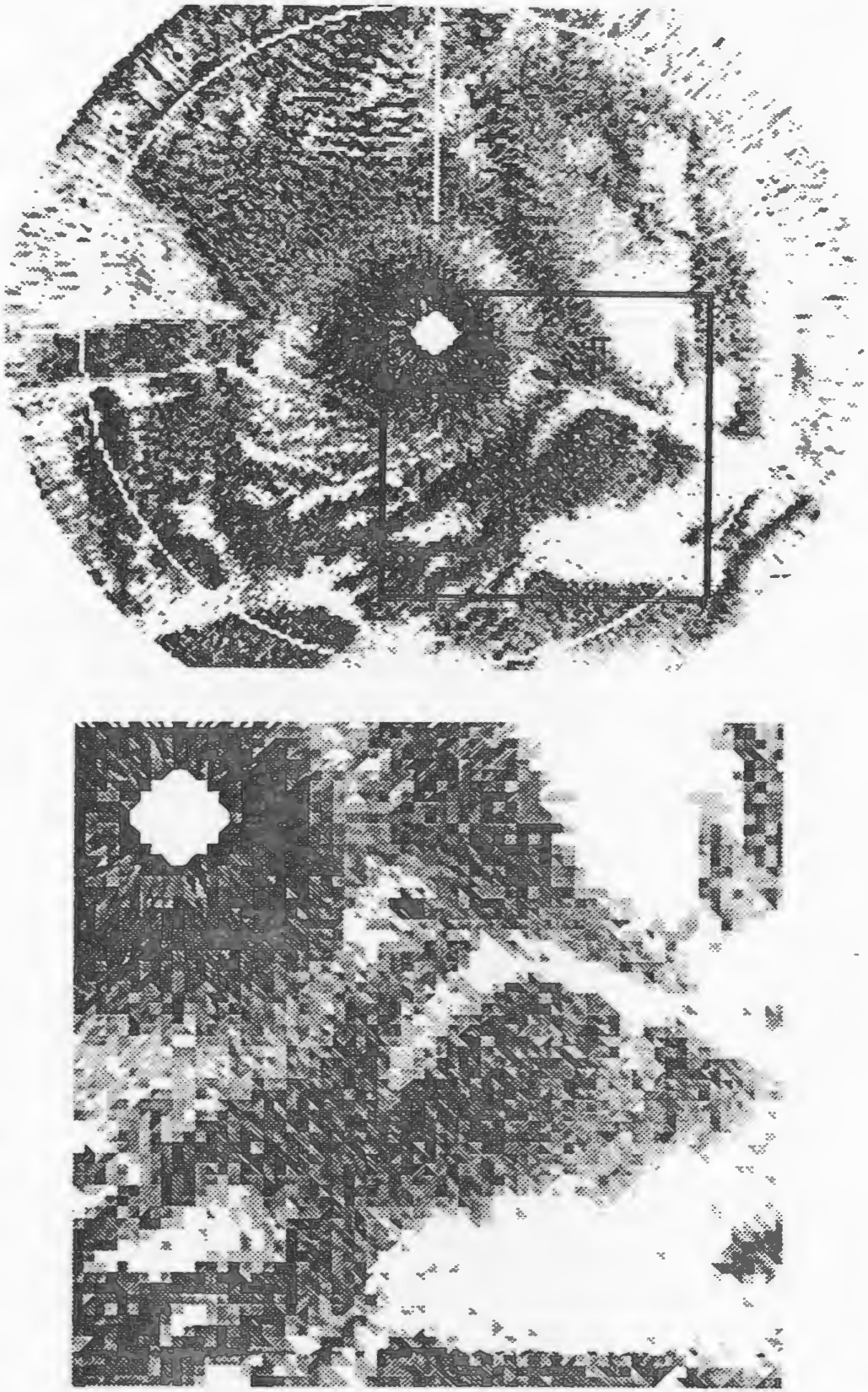

Figure 3.4: A sidescan sonar image of lunate megaripples. Note the scale in this image is different than the previous images, with the white range ring still at two meters from sonar nadir. This image is from the start of the second storm at Burley Beach. The wave parameters were $\theta_s = 0.6$ and $S = 0.4$.

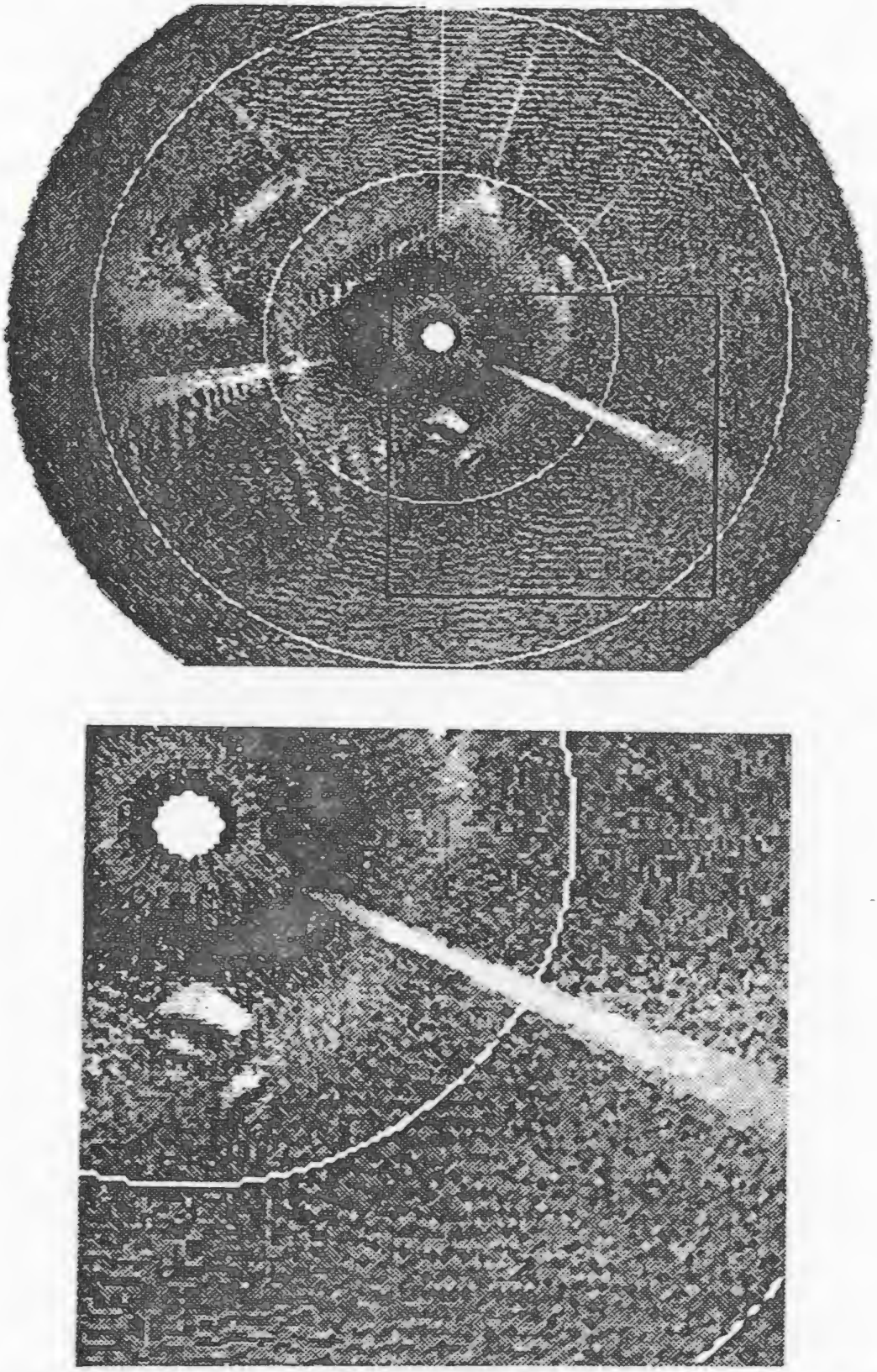

Figure 3.5: A sidescan sonar image of evanescent ripples. This image is from the decline of the third storm at Burley Beach. The wave parameters were $\theta_s = 0.8$ and $S = 0.5$. (Note that the scale is the same as the first three images.)

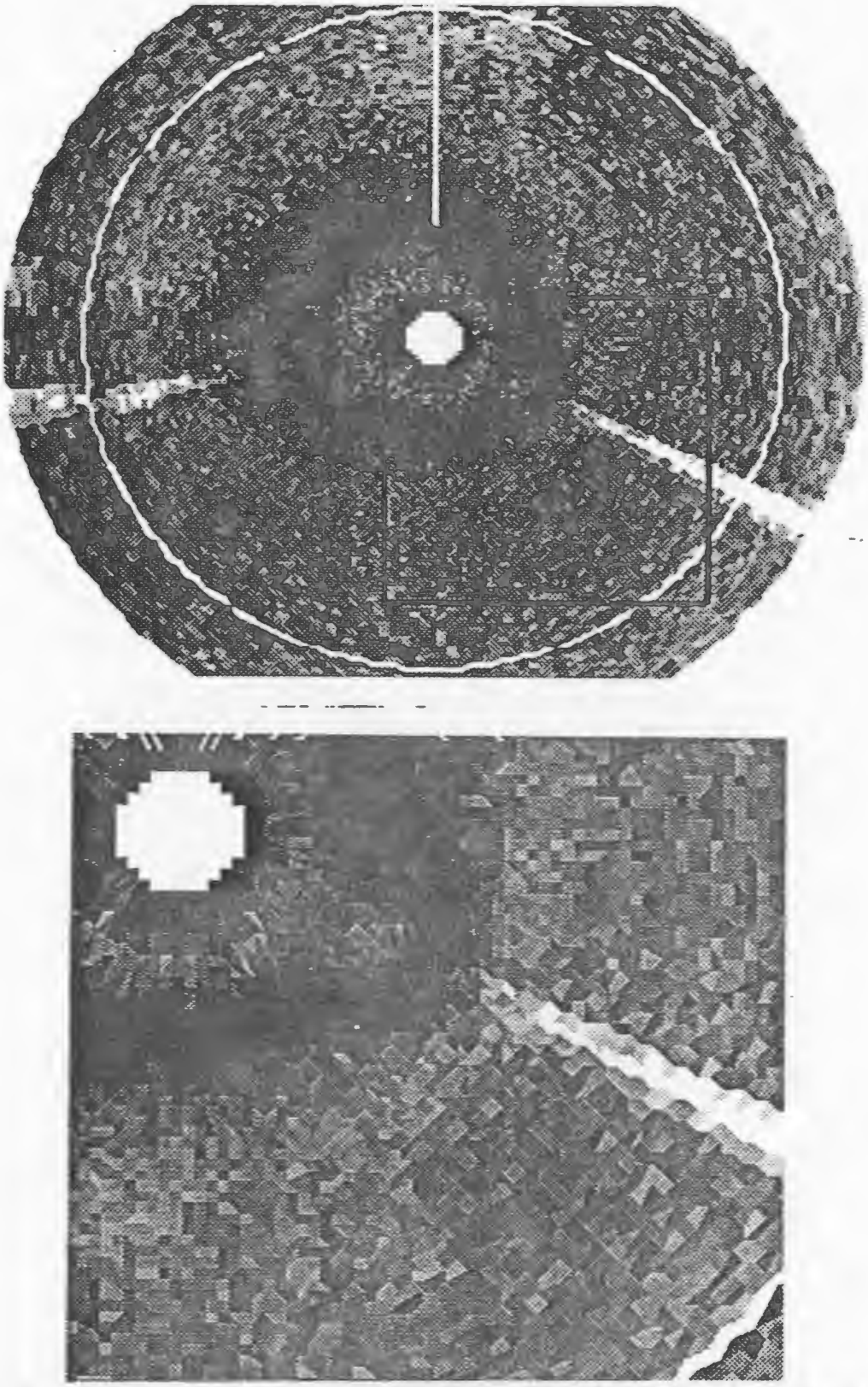

Figure 3.6: A sidescan sonar image of flat bed taken from the decline of the third storm at Burley Beach. The wave parameters were $\theta_s = 1.1$ and $S = 0.4$. (Note again the factor of two magnification in scale to show bottom detail.)

The sonar images are displayed using darker gray to show areas with greater acoustic backscatter. It was found that regular ripple features are most visible when the entire data set is imaged, while the irregular features such as megasripples are more easily seen when the data are plotted at higher magnification, as in Figure 3.4. The shadows from the frame, supports and instruments are readily identified as white areas which appear in the same spot in every image, radiating outward from the centre as sketched in Figure 3.7. The shadows of the guy wires in the right hand quadrant of the figure do not appear to be cast radially from the sonar head because they run from the frame to the bottom at an angle to both the vertical and horizontal. The large shadow in the left quadrant of the images is due to an angular sonar housing mounted 50 cm away from the rotary sidescan head and labelled A in Figure 3.7. The shadow at the top of the image (which corresponds to the offshore side of the image) is from a loop of cable attached to the frame. The white streak extending from the center to the top of the page is an artifact of the data plotting procedure. The remaining contrast is attributable to bedforms.

The interpretation and classification of these images is as follows. The long crested small scale ripples shown in Figure 3.1 are typical vortex ripples. Note that the offshore direction is towards the top of the page, so these ripples are not shore-parallel, but rather are aligned perpendicular to the direction of the incident waves. These ripples formed between the second and third storm under very low waves (in fact the water was sufficiently calm that the wave data acquisition system was shut down). The crest-crest length of these ripples is $\simeq$ 8 cm, which is somewhat less than the anorbital ripple crest-crest length observed or predicted by Nielsen's or Wiberg and Harris' formulae. The wave conditions were estimated by eye to be approximately 15 cm wave height and 3.5 second period. When these wave parameters are put into the Wiberg and Harris formula, the prediction is for orbital ripples of crest-crest length of 7.6 cm. Wave heights below $10-12$ cm are below the level of no motion, so for 3.5 second waves, ripples of shorter crest-crest length were not able to form. Note also that the contrast in the image varies with angle. When the sonar head points along

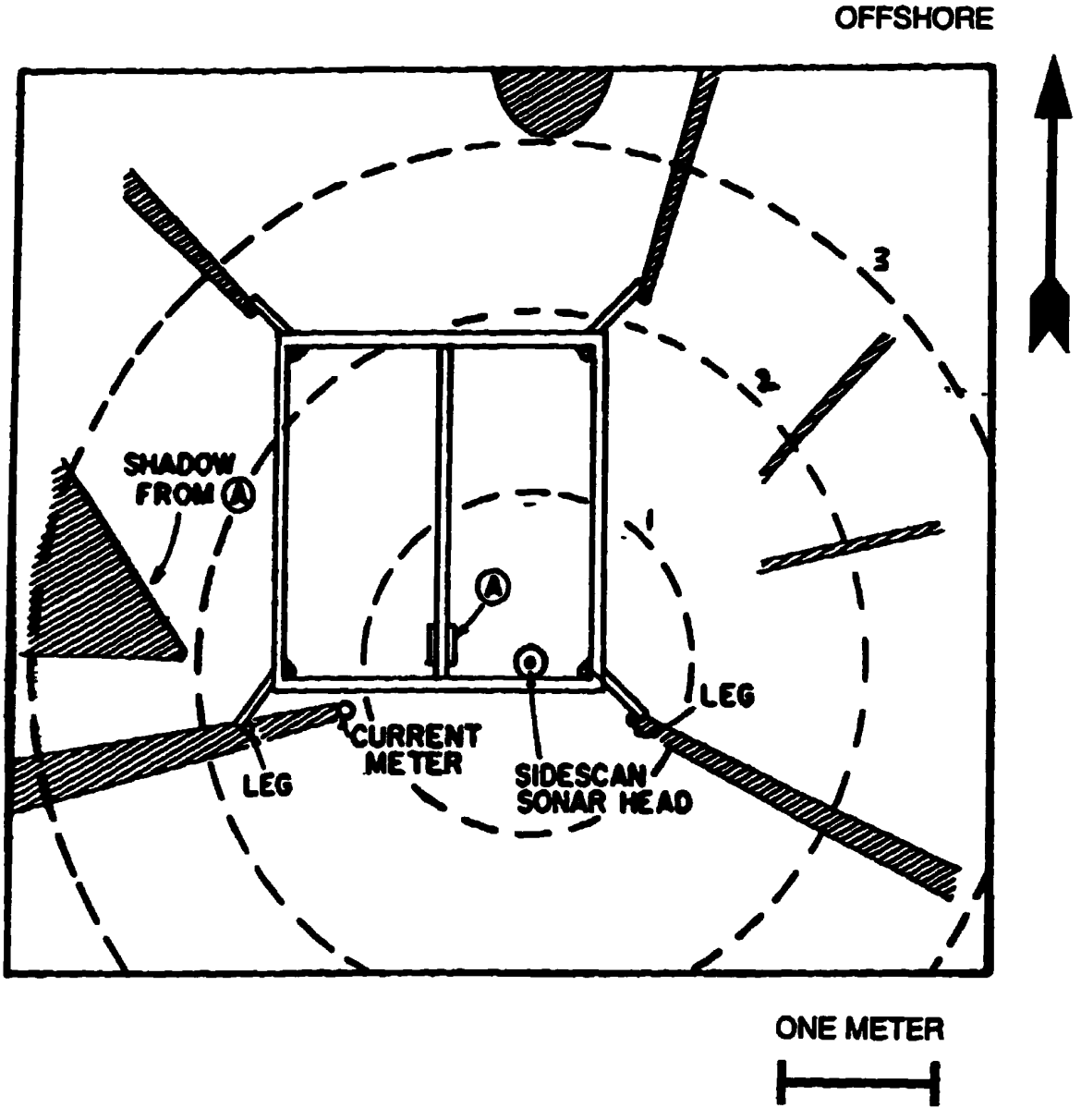

Figure 3.7: Sketch of sidescan sonar image, showing the shadows from the instrument support frame and other instruments shaded grey.

the crests very little contrast is generated.

Figure 3.2 is from the end of the third storm (22:00 on October 25, 1994, Year Day 299), and shows an almost completely uniform bed of type I irregular short crested ripples. These ripples form a brick-like pattern and thus give equal contrast in all 360 degrees of the beam direction. The spacing between crests changes as a function of azimuthal angle, being approximately 10 cm in the cross-shore direction and 20 cm in the longshore direction, thus indicating a 2:1 crest to span length ratio. The Shields parameter and wave surface skewness for this image were $\theta_s \approx 0.25$ and $S = 0.2$.

The third image, in Figure 3.3 is from 18:30, Year Day 299, during the decline of the third storm. It shows a field of cross-ripples with a patch of long crested ripples in the top right quadrant of the image. The larger scale cross set in the cross-ripple pattern has a crest-crest length of 30-40 cm at an angle of approximately 15 degrees counterclockwise from the shore-normal (which points towards the top of the page). The smaller scale cross set has a crest-crest length of 12-15 cm with an average orientation of approximately 58 degrees clockwise from the shore-normal. The large ripples in the upper right quadrant of the image appear to be continuations of the larger cross set. Though smaller cross set ripples can not been seen, they may be shadowed from view by the edges of the larger cross set. The continuous video recording showed that the patch of long-crested ripples was the remnant of the evanescent ripple field shown in Figure 3.5, which is from 14:30, Year Day 299, four hours earlier. The Shields parameter and wave surface height skewness for this time period were $\theta_s = 0.50$ and $S \approx 0.30$.

An example of lunate megaripples is shown in Figure 3.4. This image was taken at 16:30, Year Day 294, the start of the second storm. The Shields parameter and wave surface skewness for this time period were $\theta_s = 0.60$ and $S = 0.40$. It is interesting to note that during the decline of the third storm, the sand bed did not go through a stage of large numbers of lunate megaripples, though a few lunate forms (with their characteristic rapid shoreward progression) were observed. The lunate forms occur in a variety of sizes with no regularity of spacing in general. The lunate ripple forms

observed here moved towards the beach at a rate of approximately one meter per hour which is in accordance with the observations of Clifton et al. (1971). Note too that the range in this image is half that of the previous images. The proximity of the bottom made looking to a 5 meter range impractical, so the system was switched to a 2.5 meter range.

The evanescent ripples shown in Figure 3.5 have a crest-crest length of 9-10 cm, consistent with the theoretical crest-crest length for anorbital ripples in sand of this grain size (0.17 mm median diameter). The reason these ripples have been classified as evanescent is that during continuous observation with the sonar system, it was observed that the ripples were wiped out by the largest waves, but would return after a few smaller waves had passed. Also noticeable in this image are several larger scale bedforms. A crescent shaped depression (area of low signal intensity) located one meter shore-ward of the sonar head has the dimensions and shape of a megaripple. The wave-like structures in the lower left quadrant of the image between two and three meters in range are the first signs of cross-rippling. The Shields parameter and wave surface skewness for this time period were $\theta_s = 0.80$ and $S = 0.50$.

The final image in Figure 3.6 shows flat bed. The posts of the support frame are still visible, indicating that suspended sand has not obscured the field of view, but there is very little contrast otherwise. Acoustic contrast has been reduced, however, in the observations of evanescent ripples in Figure 3.5, so under the higher energy conditions of this image it is likely that the acoustic penetration to the bed is further reduced. It is possible that large megaripples may exist beyond the field of view (recent observations have indicated that megaripples increase in size with increasing wave and current velocities), but their rapid march shoreward would probably bring them into the field of view occasionally. Thus flat bed conditions described here are indicative of flatness within a four to six meter diameter field of view at one location over time periods of the order of several hours (clearly, at still larger scales the bed is not flat, as the sand bar on which the instrument frame was mounted moved but did not disappear). The Shields parameter and wave surface skewness for this time

period were $\theta_s = 1.1$ and $S = 0.40$, which are consistent with previous studies showing flat bed for Shields parameter greater than one. The radius in this image is also 2.5 meters, as in Figure 3.4. In this case the range was switched because of the lowered acoustic contrast due to suspended sand.

The images presented here have been slant-range corrected assuming a horizontal bed. Once this correction has been made, the circles drawn at two and four meter radii represent distances along the bottom. Though the sonar images are displayed in a manner similar to a photograph of the bottom, there are several differences worthy of note between these acoustic images and more familiar photographic images. The contrast is due to differences in the acoustic backscatter intensity from the bottom. As a single frequency sound source is used, and the sand is of relatively uniform size, all the contrast is due to variations in the angle of the bed with respect to the sonar head, and variations in the intensity of the sound striking the bottom due to the beam pattern of the head, as displayed in Figure 2.1. The beam pattern produces a strong variation in intensity of the returning signal with distance along the bottom. The very bright backscatter within the first meter is due to the principal side lobe of the beam pattern. There are a variety of possible image processing techniques available to normalise the intensity, however this variation can also be used to advantage in determining whether the bed is level and normal to the axis of rotation of the sonar head. If the bed is level, the variations in intensity will appear as circular rings, whereas if there is an overall slope they will appear as ellipses. Other distortions of the rings can show variations from the horizontal planar bed assumption. Thus the variations in insonification intensity have not been removed from the images displayed here.

The images displayed in Figures 3.1 through 3.6 have been chosen in part for their clarity, but there is some blurring due to intermittent sand suspension above the bottom. The period of the waves was 4 to 5 seconds over the time which the images were taken. In the 47 seconds of a single sweep approximately 10 to 12 waves go over the system, and some of these generate suspension events. The 2.25 MHz

frequency gives a wavelength of the sound in water of approximately 0.7 millimetres, which is on the same order as the sand grain circumference, so suspended sand grains act as individual, strong scatterers. This strong scatter also prevents the sound from travelling into the bed, ensuring that the surface of the bedform is what is seen.

Over 600 images were digitized and stored from the 250 hours of field data. These images and the supporting sonar screen videotape provided the ability to characterize the bedforms throughout the period of the experiment. The data were divided into three groups, one for each storm. To summarize the enormous amount of data present, images from each hour were classified according to seven bedform types using the modified Clifton classification scheme discussed in the Introduction. If more than one bedform type was present, more than one was included in the summary tables for that hour. The summary tables are presented in the current meter results section. The wave tank results were similarly analysed and classified.

3.1.2 Ottawa 1993 Sonar Images.

Figure 3.8 displays sonar results from five wave runs in the Ottawa'93 experiment. The images have been cropped so that reflections from the side walls are not displayed and only the beachward half of the image is presented. The images are from runs 11, 20, 21, 22, and 19 (see Table 3.1 for more detail) and are presented in order of increasing Shields parameter. In the 1993 Ottawa experiment, the range of bedforms from linear vortex ripples to evanescent forms was observed, but technical difficulties prevented the generation of sufficiently energetic JONSWAP waves, and time did not permit a full series of wave groups, so each ripple type was not generated by each of the three wave types. This deficiency was corrected in the Ottawa'95 experiment.

As can be seen from Figure 3.8a, the ripple crest-crest spacing for linear ripples was on the order of 11.5 cm. This wave run was done with regular 3.5 second, 20 cm high waves. Visual inspection (and photographic evidence) of the ripples after the waves were turned off indicated that they were more regular than the sonar image indicates, due to the limited resolution of the sonar system and contrast limitations

(especially in the lower left corner) from the angle of incidence of the sound on the bottom.

The irregular or brick pattern ripples displayed in Figure 3.8b had a crest-crest spacing of approximately 10 cm (this is less well defined as the ripples are less regular). They were produced with bimodal wave groups with a peak amplitude of 30 cm and a peak frequency of 3.3 seconds.

Cross-ripples are shown in Figure 3.8c. This image is from run 21, which was the second of the two grouped wave runs, with a peak wave period of 3.3 seconds and a maximum wave height of approximately 60 cm. Sonar images were taken with the waves on and then after the waves were turned off, and little difference was noted. The photograph in Figure 3.9 shows how the cross-ripples appeared to an observer looking down into the wave flume, with illumination coming through the test section observation window. The cross-ripples were much more distinct visually than in the sonar image because of the previously mentioned limitations and due to shadowing of the lower amplitude ripple set by the larger set. Though there was a distinctly larger (in both amplitude as observed visually, and crest-crest length) ripple set with smaller ripples in the troughs, there did not seem to be a single preferred direction for this set, leading to a somewhat more confused bed than was seen in the field (Figure 3.3). Results from the computer modelling indicate that this may be due to the complete lack of longshore current, and that a small longshore current helps establish the direction of the dominant set in cross-ripples.

The fourth image, Figure 3.8d, is from run 22, with regular 3.5 second waves and a wave height of approximately 55 cm. The large square in the upper third of this image is the sonar view of the square ripple measurement template as it rested on the bed. There are not very many bedforms with the characteristic lunate shape visible, however visual verification indicated that the features in the lower right and in the upper central part of the ripple measurement template were distinctly lunate shaped and had the characteristic onshore velocity (of approximately one meter per hour) of small lunate megaripples. Larger lunate megaripples were observed in the Ottawa'95

experiment.

The final image, Figure 3.8e, shows how evanescent ripples appeared to the sonar system. These ripples were produced by 5 second 50 cm high waves.

3.1.3 Ottawa 1995 Sonar Results.

The sonar results from the Ottawa'95 experiment were qualitatively similar to those from the Ottawa'93 experiment, with a few notable differences. A more comprehensive set of wave conditions was run in the Ottawa'95 experiment, and the sonar images were more evenly insonified due to the change in head angle from 30 degrees below horizontal to 20 degrees below horizontal. Figure 3.10 shows examples of the sonar images obtained, with a progression of low amplitude to high amplitude regular waves. Similar progressions were observed for grouped waves and irregular waves. The different sand, with a 0.15 mm median grain size rather than 0.095 mm used in the Ottawa'93 experiment, affected the type of bedform observed for a given wave height, and affected the size of the lunate megaripple forms. In the Ottawa'93 experiment the lunate megaripples took the form of discrete crescentic scour pits of dimensions approximately 0.5 m from horn tip to horn tip. In the Ottawa'95 experiment the lunate forms were more varied in size and shape, including forms that spanned the full width of the tank. These were observed under 3.5 second waves at 60 and 70 cm wave height regular and grouped waves.

The regular and grouped wave runs produced very similar bedforms for the same wave heights. Irregular wave runs in general produced ripple forms characteristic of somewhat lower wave height for significant wave height equal to that of regular or grouped waves. It is felt that the irregular waves may have produced similar features, but only one or two large waves per minute were generated, and the waves were only run for 45 minutes, so they may not have established a steady state bed. As the regular and grouped wave runs produced such similar results, only the results from the regular waves have been shown.

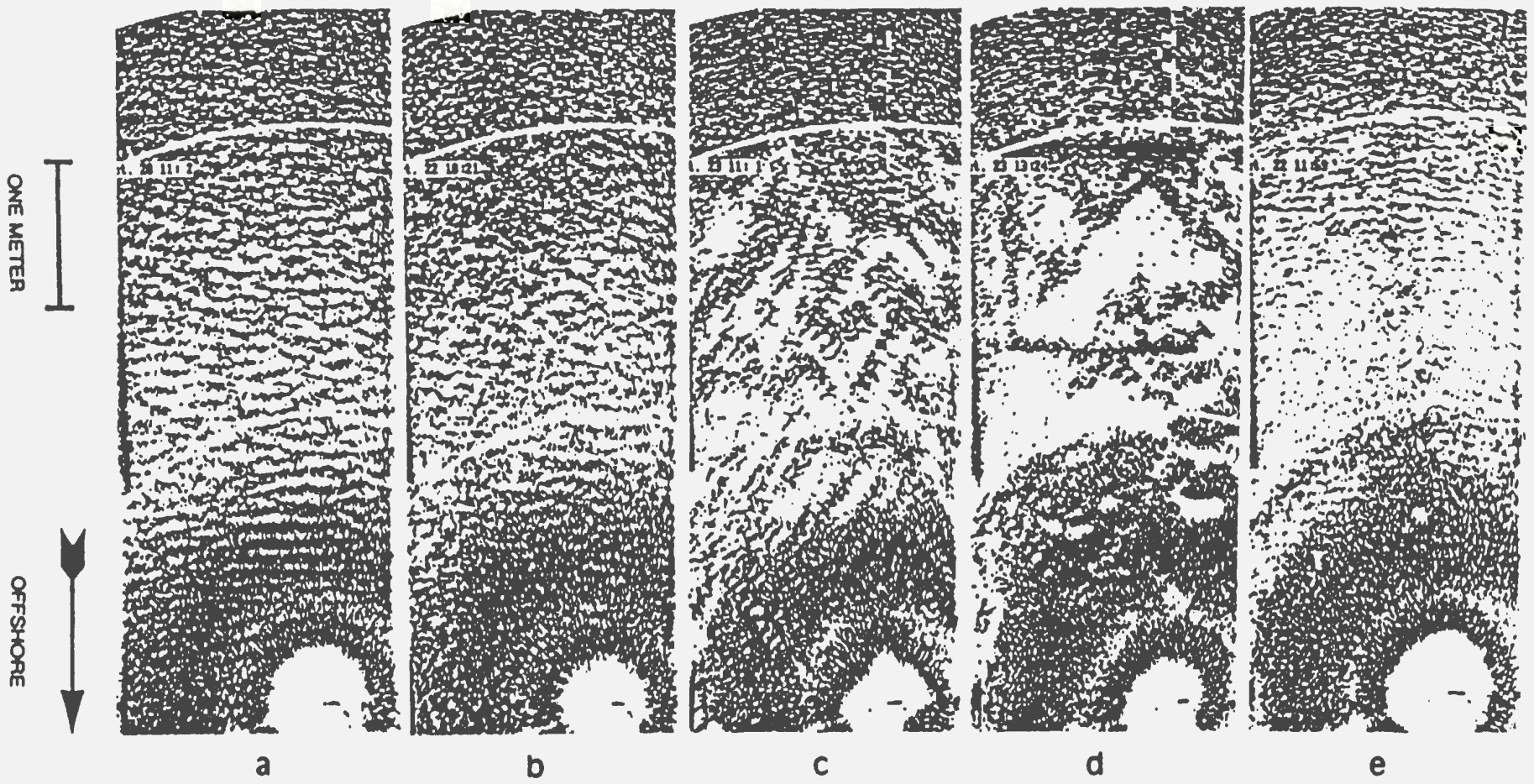

Figure 3.8: Five rotary sidescan sonar images obtained during the Ottawa'93 experiment. The bedforms in images a-e were generated by wave runs 11, 20, 21, 22, and 19 respectively. The Shields parameters for the runs were 0.19, 0.40, 1.02, 1.12, 1.62, and the skewnesses were 0.38, 0.45, 0.72, 0.98, and 0.42.

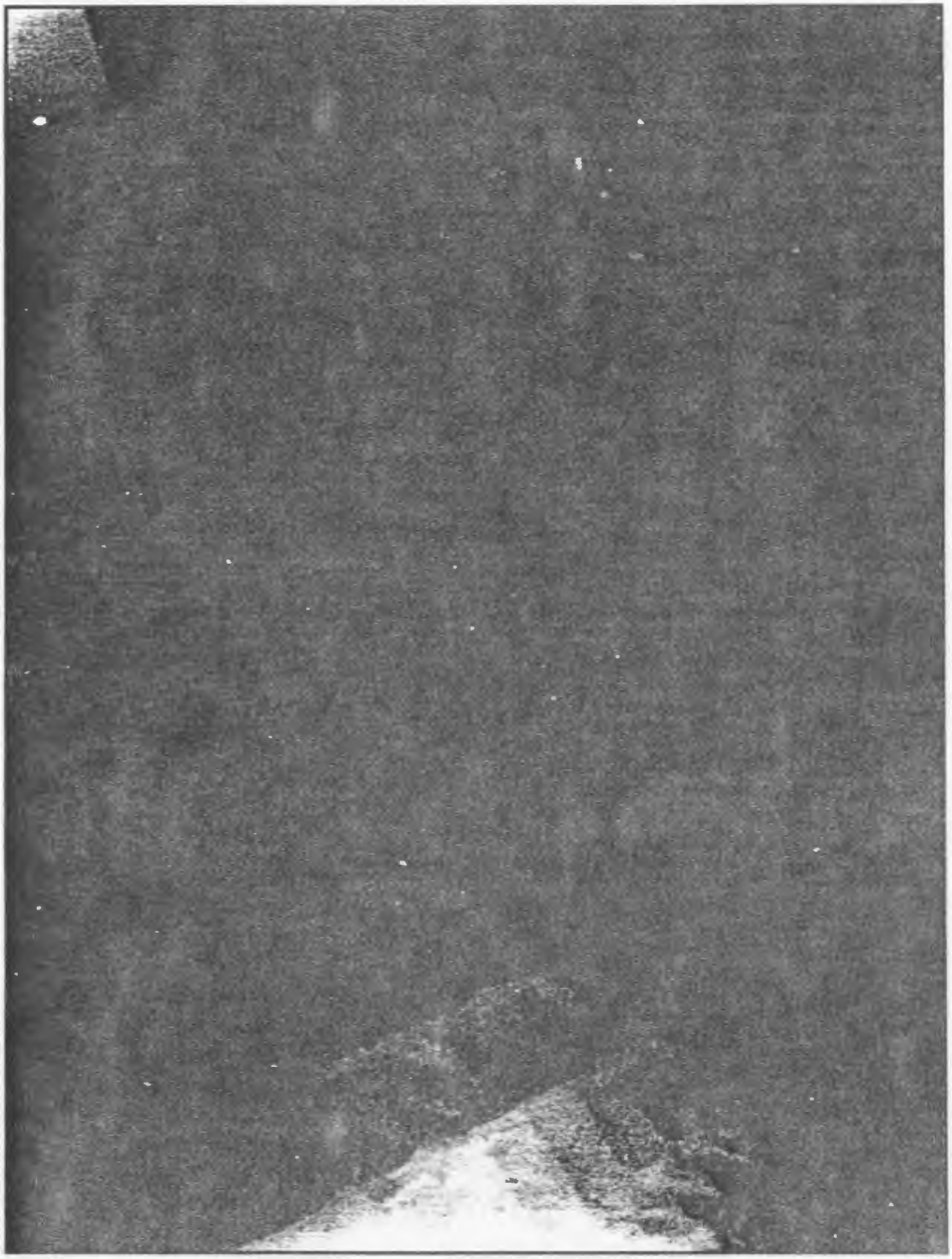

Figure 3.9: Photograph of Cross-ripples in the Ottawa Wave Research Flume. The photograph was taken from above, with lighting from the side through the plexiglass observation windows and from above by the overhead fluorescent lighting. The image is oriented with the wave paddle and instrument frame on the right and the beach on the left of the image.

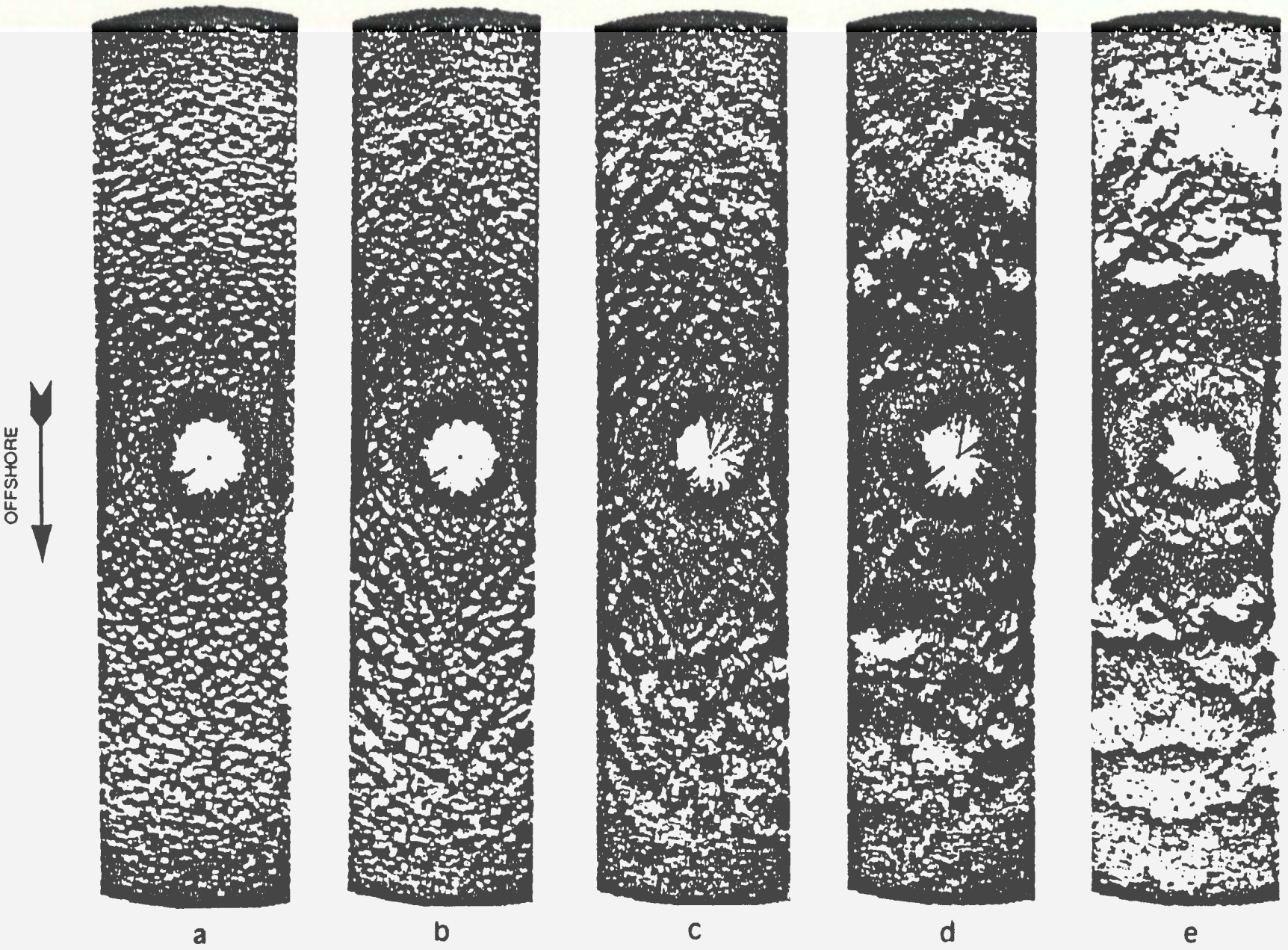

Figure 3.10: A sequence of six rotary sidescan sonar images obtained during the Ottawa 1995 experiment. These bedforms were generated by regular waves with wave heights 20, 30, 40, 50, 60 and 70 cm. Shields parameters of 0.30, 0.38, 0.52 0.84, and 0.87 and skewness of 0.35, 0.34, 0.40, 0.50, 0.63.

3.2 Wave and Current Meter Results.

Part of the process of understanding the mechanisms of formation of cross-ripples and other bedforms must be the analysis of wave conditions under which various bedforms occur. The wave and current conditions at Burley Beach have been summarised as time series of 15 minute averages, whereas the wave conditions in the Ottawa wave tank are more conveniently summarised in tabular form. The differences in measuring equipment, and their relative accuracies and calibrations are discussed in the analysis section.

In general, the wave results were analysed to obtain mean and standard deviations of velocities, velocity and surface height skewness and asymmetry, peak wave periods (which were already well known for some of the mono-chromatic wave tank results) and derived quantities such as Shields parameter and near-bottom orbital diameter. In addition, the field results were analysed for several other influences which may have contributed to the observed bedforms. These factors include various wave direction properties such as mean and principal wave incident directions, directional spectra, and Longuet-Higgins directional spreading factor. These other influences do not receive a lot of attention in this work due to the similarities observed in the field results and wavetank results (where waves are unidirectional). Also of interest is the level of infra-gravity wave energy and Clifton's wave velocity asymmetry. Yet these two possible influences will be shown to have little correlation with observed bedform pattern.

3.2.1 Burley Beach.

Figure 3.11 summarises the root mean square and mean velocity results from current meter CM849, mounted nominally 50 cm above the bed approximately 2 m offshore from the sidescan sonar head. The shadow from this current meter, the mounting rod, and CM845 mounted on the same rod at 20 cm from the bed is shown in Figure 3.7 in the top left of the diagram (where the top of the page is looking

off-shore). Means and standard deviations from the on-offshore direction x (where positive x is on-shore) and along-shore direction y (where positive y points towards the south-west) have been calculated from 15 minute long segments (approximately 3600 points over roughly two hundred waves). Time has been plotted in Year Days, with day 290 corresponding to October 16, 1992, and day 300 corresponding to October 26, 1992. The gaps in the record are periods of calm in general, although there are a few points missing on days 290, 293 and 299 due to equipment malfunction.

Similar gaps appear in the pressure sensor record, as shown in Figure 3.12. In addition, comparison between pressure sensor and current meter data indicates that the current meter CM849 was buried briefly near the end of day 292. There appear to be four storms over the ten day period, with no period of calm between the first two storm fronts. Thus for the purposes of this analysis the first two storms have been merged together so that three distinct storm events will be discussed. The first storm event occurred between Year Days 290 and 294, the second between Year Days 294 and 296, and the third between Year Days 298 and 300.

Skewness and asymmetry have been plotted in Figure 3.13 as calculated from the pressure sensor. The relationship between skewness calculated from the pressure sensor, S_p, and that calculated from the Marsh-McBirney current meter CM849x, S_v, has been plotted in the appendix. Linear regression gives $S_p = 0.94S_v + 0.195$, with a correlation of $R_s = 0.91$. Similar plots and analysis for asymmetry give $A_z = 0.46A_v + 0.675$ with a correlation of $R_a = 0.84$. Typically in the literature skewness and asymmetry are quoted from surface height measurements, probably because there are many more such observations and they are easier to obtain, but also because there is no ambiguity as to wave direction involved. It was also found that the pressure sensor data were cleaner, with fewer dropouts and spikes. Such noise becomes very important when calculating third and higher moments. In Figure 3.13 the skewness and asymmetry were calculated from the entire 55 minute long record, to obtain reasonable stability in the asymmetry values which were very sensitive to noise in the data.

The distance from the frame and instruments to the bottom varied throughout the experiment. This change in distance to bottom was due to the deposition and erosion of sand associated with the onshore-offshore movement of the sand bar on which the frame was mounted (as determined by rod and transit surveys on calm days, Figure 2.3). The distance to bottom was accurately tracked with the four downward looking sonars. The distance from the bottom to the most reliable Marsh-McBirney current meter, CM849, as calculated from the closest downward looking sonar head (which was approximately 50 cm away parallel to shore) has been plotted in Figure 3.14.

Derived Dimensionless Bed Shear Stress.

In this study Shields parameters were calculated several different ways and results were compared. Since the Shields parameter was originally derived for steady unidirectional flow in which the bulk flow velocity u_m could be easily characterized, some adaptation to wave dominated flows was necessary. As mentioned in the introduction, Miller and Komar 1980b found that velocities derived from 'significant' wave height provided the best correlation for bottom bedforms with regular wave induced laboratory bedforms. In this experiment velocities were measured directly, hence an analogous 'significant velocity', $u_{1/3}$ was defined. $u_{1/3}$ was obtained directly by dividing the wave velocity time series (the velocity time series after removal of the mean current velocity) into individual waves by upward sloping zero crossings, finding the maximum and minimum velocities in each individual wave (after filtering out very short waves which could be noise related), sorting these, taking absolute values and averaging the highest third. Absolute values were necessary because the shoreward velocities tend to be larger than off-shore velocities, while the net bottom stress is caused by both on-shore and off-shore velocities.

Because of the vector nature of the wave velocities, several possibilities exist for corrections due to wave directionality. Initially, the mean wave direction was found (using the method discribed in the Appendix), and components of u and v (corresponding to on-offshore and along-shore directions) added vectorially for each time

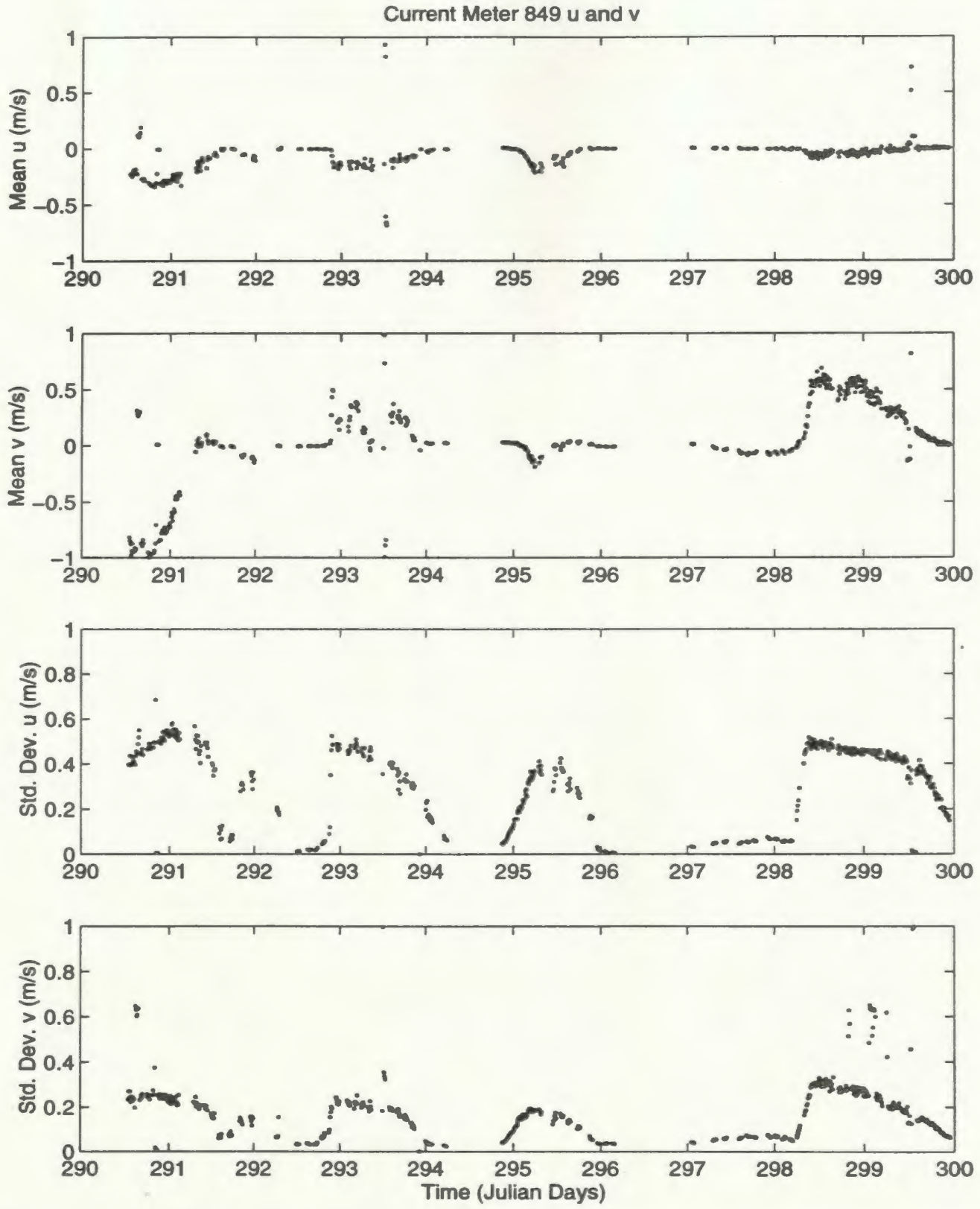

Figure 3.11: Fifteen minute means and standard deviations of the wave record from current meter CM849. The positive u direction corresponds to on-shore (pointing southeast), and the positive v direction corresponds to along-shore pointing southwest.

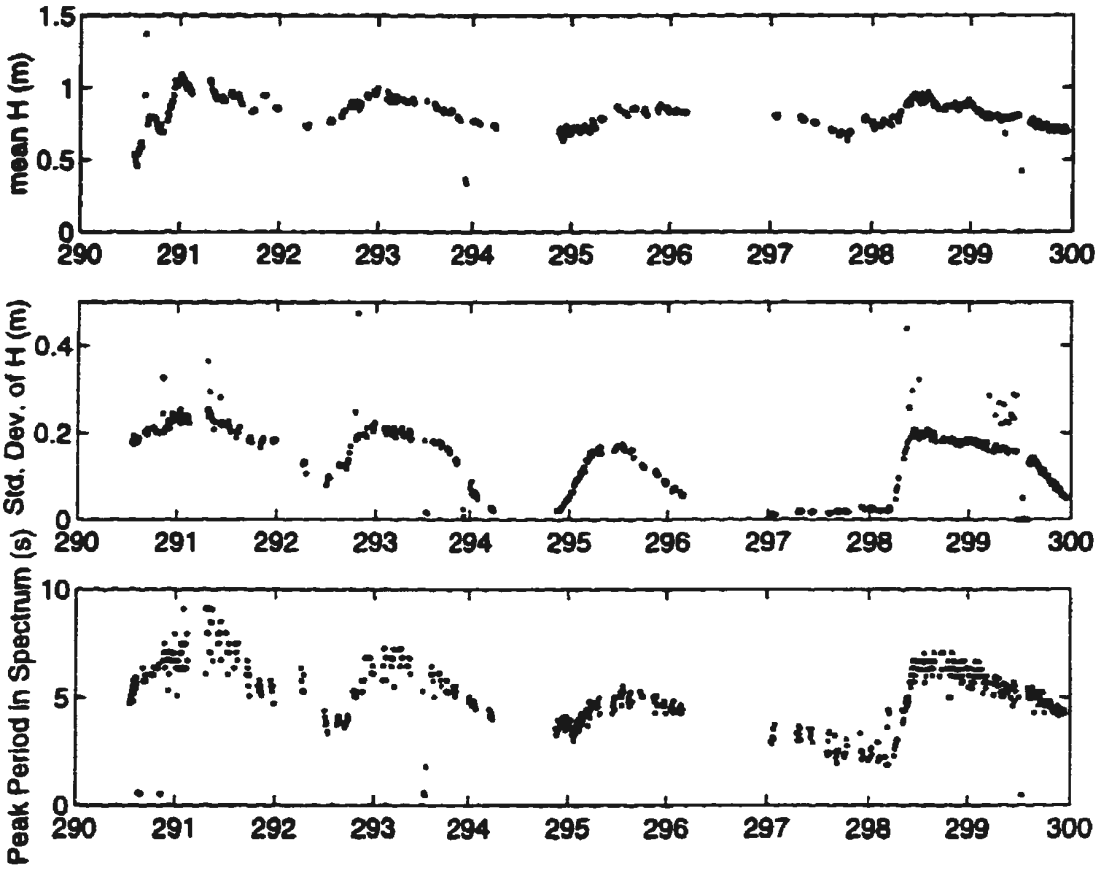

Figure 3.12: Fifteen minute means, standard deviations, and peak wave periods of the wave record from pressure gauge P500. The pressure values have been converted to sea surface elevation H above the sensor (which was nominally one meter below the surface in still water) by the UDATS system using calibration values (Hazen et al. 1988).

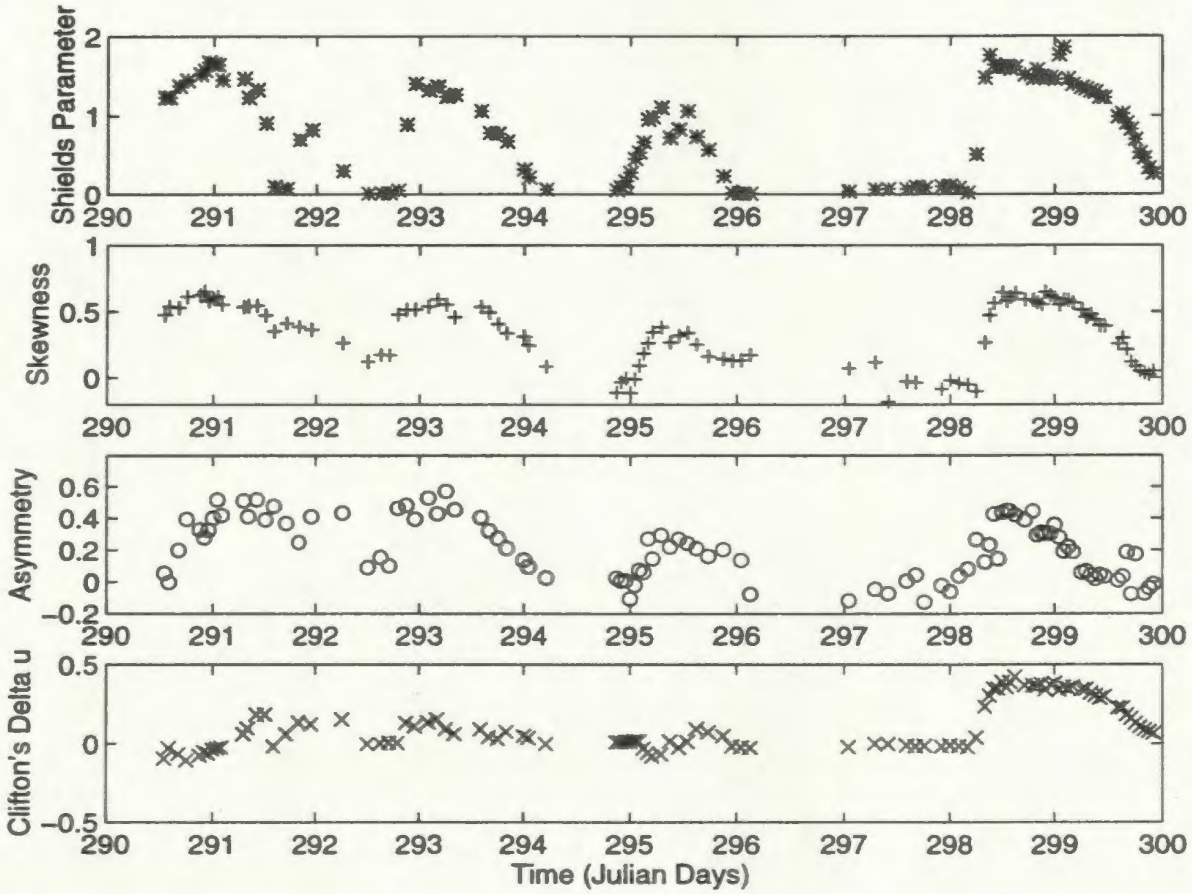

Figure 3.13: Skewness and Asymmetry of P500 pressure sensor data for hour long records. Shields parameter and Clifton's Δu_s as derived from Marsh-McBirney Current meter CM849 have also been plotted for reference.

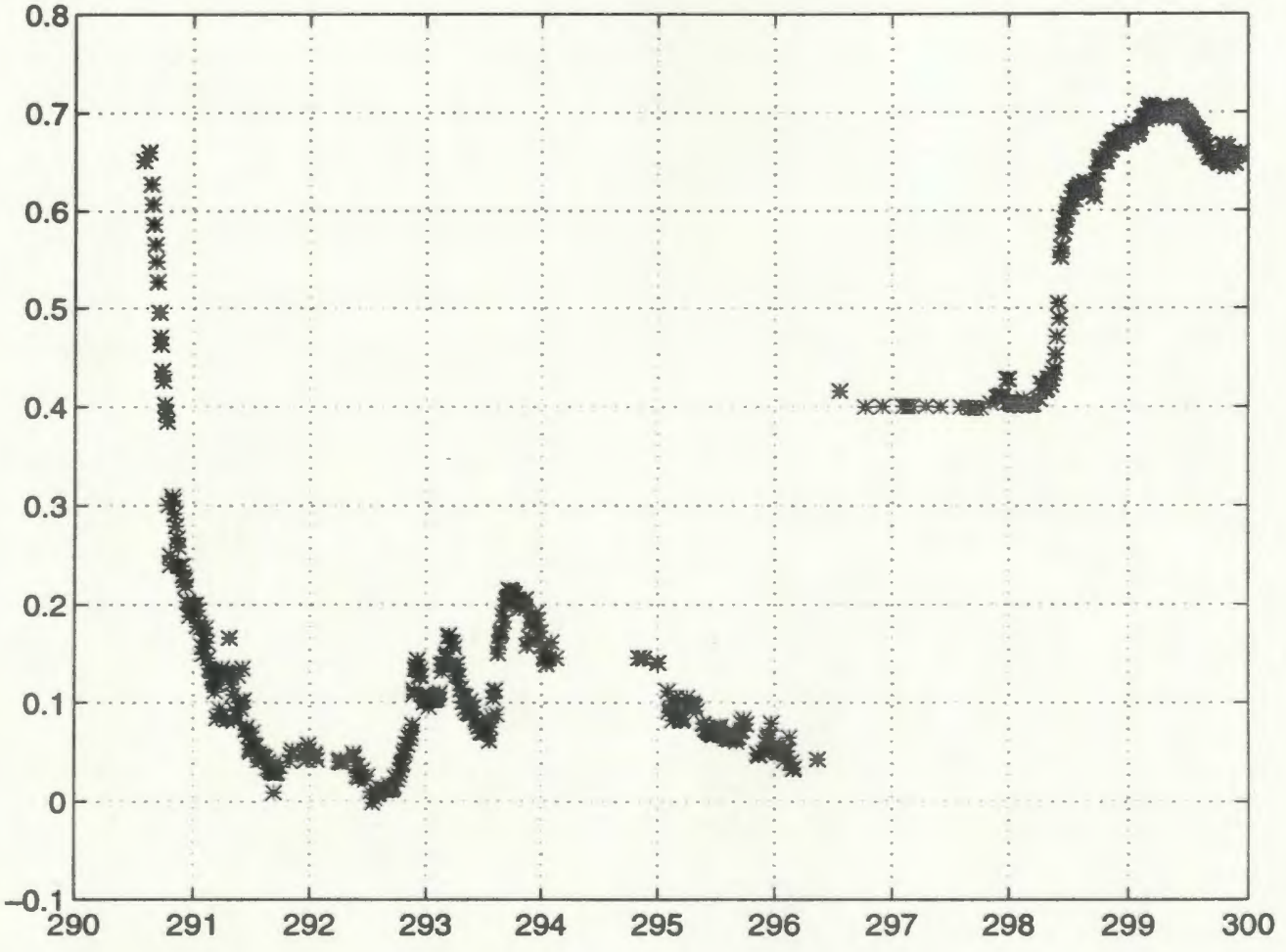

Figure 3.14: Estimated distance from the center of Marsh-McBirney Current Meter CM849 to the bottom, as measured from the closest sonar altimeter on the same experiment frame (approximately 50 cm away). Note that the jump in height in the middle of day 296 is from the repositioning of the instrument frame.

point to produce the single wave time series required. This approach assumes that the effects of velocities pointed towards either side of the mean wave direction vector cancel over time. Care must be taken when making this assumption in sediment transport situations, as the actual sand transport is a function of a high power of the velocity.

Thus in an effort to include the effects of all velocity components, the statistically derived formula

$$u_s = 2\sqrt{u_{rms}^2 + v_{rms}^2} \tag{3.1}$$

suggested in Guza and Thornton (1980) was used to calculate significant velocity. u_{rms} and v_{rms} were the standard deviation of the on-offshore and alongshore velocity records. u_s was chosen to display the data because it takes all the velocity variance into consideration.

The Shields parameter was then calculated using

$$\theta_s = \frac{f_w \rho u_{sig}^2}{2(\rho_s - \rho)gD}. \tag{3.2}$$

with either $u_{1/3} = u_{sig}$ or $u_s = u_{sig}$. As expected, for the Burley Beach wave data, these two calculation methods for u_{sig} yielded results within 10% of one another, with the value from u_s consistently smaller.

It is important to note that, as mentioned in the Introduction, investigators have established that the flow in the bulk fluid may be different than that very close to the bed. Grant and Madsen (1979) suggested that since the wave boundary layer was much thinner than the current boundary layer in most wind wave situations, the shear due to wave motions may be the dominant influence on the bed even under currents with velocity equal to the peak wave induced velocity. Thus wave surface height may be a more reliable indicator of the shear at the bed than velocity measurements in the bulk flow. Also, as will be discussed in the section on combining bedform and flow data, there were no bedforms at Burley Beach during the periods of significant cross-shore and long-shore flow velocities. Hence for this study Shields parameters without mean currents have been quoted and compared with those of other studies which use wave height (and hence no measure of current effects).

3.2.2 Ottawa 1993.

The wave conditions in the National Research Council 97 meter wave flume were extremely stable, so values of relevant wave parameters have been listed in tabular form in Table 3.1. Waves were run over a 10 day period, however technical difficulties with current meters and water clarity meant re-running the conditions for runs 1 to 5, thus the table begins at run 6.

The Shields parameter has been calculated using the Marsh-McBirney Current meter located on the wave paddle side of the instrument frame, approximately 30 cm above the bed. The Shields parameters for the three types of waves were calculated using $u_{1/3}$ rather than the statistically derived form of u_s from Equation 3.1 because the statistics of the grouped and regular waves do not follow the Gaussean assumptions.

The Marsh-McBirney current meter records were only ten minutes long in the Ottawa'93 experiments. These records were very noisy due to the use of fresh water in the tank and the noise of electronics in the laboratory, so these records could not be used to calculate skewness and asymmetry. The wave staff records were also ten minutes long, but they were of excellent quality so provided reasonable estimates of asymmetry. As in the Burley Beach data, the asymmetry was quite small until the waves started breaking. In the Ottawa'93 experiment none of the waves were breaking, so asymmetry values do not contain very much information. Asymmetry does appear to be significant for the five second period waves and for the highest energy runs in 3.5 second waves and the JONSWAP spectrum waves. However, the five second period wave runs had wave reflection amplitudes calculated to be greater than 5% indicating that wave reflections and possibly standing waves may have interfered with results. Thus the five second period wave runs have been excluded from further analysis.

The ten minute wave data runs contain approximately 170 waves for the 3.5 second wave period runs. Example time series for each of the three wave patterns is shown in Figure 3.15 . For regular and grouped waves the derived quantities were statistically stable. Shields parameters calculated from repeat runs and the third order moments

calculated for the irregular JONSWAP data were less significant, with an uncertainty of 15-20% if the wave heights were assumed to be randomly distributed variables.

There also appear to be significant differences between the wave skewness and asymmetry results for regular, group, and JONSWAP irregular waves. The irregular waves have smaller skewness and larger asymmetry when compared to regular waves of a given wave height or Shields parameter. Though not surprising, results from the next section indicate that the bedforms generated by the different types of waves tend to follow the Shields parameter variable, so that different skewness/asymmetry combinations appear to be able to produce the same bedform. This trend is consistent with the theory that these bedforms are self-organized, at least in part.

3.2.3 Ottawa 1995.

Wave and current results from the various runs in the Ottawa'95 experiment are shown in Table 3.2. As in the Ottawa'93 experiment, many of the initial runs were used to test and debug the various sensors in the tank. Other runs not listed were used by collaborators and were either of too short duration or some of the sensors were turned off to prevent interference with our collaborators' equipment. There are 15 runs with cosine-tapered type wave groups (the wave pattern of which is shown in Figure 3.16), including three repeats of 0.4 meter waves and two repeats of all others. There are 5 runs of regular waves at 4 different heights, and 8 JONSWAP type wave runs at 5 different wave heights. The repeat runs have been listed to demonstrate the statistical reliability of the derived wave parameters. As in the Ottawa'93 experiment, wave records were ten minutes long, so the regular and group wave patterns have very accurate and stable parameters, while the JONSWAP spectrum wave runs have more variability.

The irregular wave results in The Ottawa'95 wave data set contain different features than the Ottawa'93 set. The Shields parameters calculated for the JONSWAP type waves were quite low in comparison to those of similar peak wave height in the Ottawa'93 wave data. This is because in 1995, a section of the wave record with a

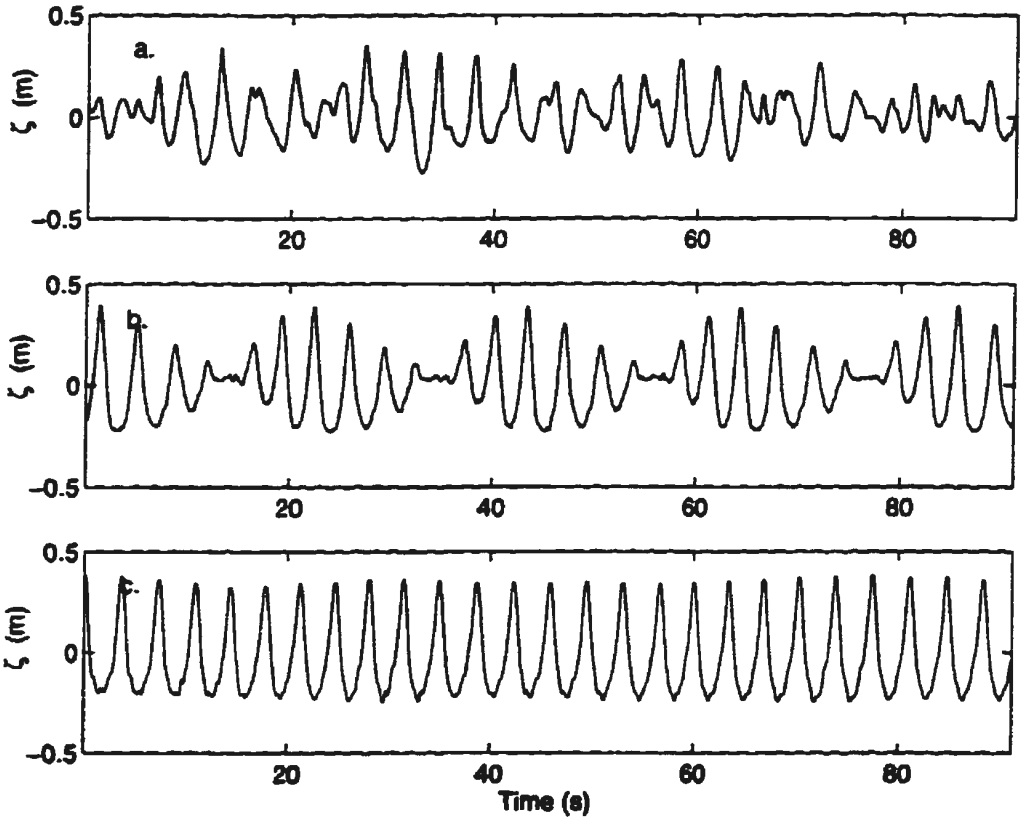

Figure 3.15: Two minute time series of surface elevation ζ from a capacitance type wave gauge mounted above the test section of the wave flume for three different runs. The time series in (a) shows JONSWAP spectral type waves from run 8, with a significant wave height of .45 meters. (b) shows data from run 21, where wave groups were formed by combining wave paddle forcing periods of 3.0 and 3.5 seconds. The maximum height is 0.60 meters. (c) shows regular waves from run 22 where regular waves of nominal height 0.55 meters were run. Note that heights deviate somewhat from their nominal (wave paddle) values due to peakiness, or Stokes interactions.

Run	Day, Time	T(s)	H(m)	Wave Type	θ_s	S	A	Δu_s	Bed
6	260,1730	3.5	0.30	JONSWAP	0.31	0.26	0.04	0.051	L
7	260,2140	3.5	0.40	JONSWAP	0.42	0.30	0.01	0.079	I.L
8	261,1150	3.5	0.45	JONSWAP	0.78	0.27	0.32	0.085	C.I
9	261,1500	3.5	0.50	JONSWAP	0.89	0.30	0.13	0.127	C.I
10	261,1830	3.5	0.35	JONSWAP	0.48	0.25	0.09	0.058	I
11	263,1045	3.5	0.20	Regular	0.19	0.38	0.00	0.014	L.I
12	263,1505	3.5	0.30	Regular	0.28	0.52	0.00	0.007	L
13	263,1810	3.5	0.40	Regular	0.46	0.69	0.07	0.003	I
14	264,0945	3.5	0.30	Regular*	0.45	0.20	0.11	0.042	I,C
15	264,1255	2.0	0.20	Regular	0.12	0.08	-0.11	-0.002	I
16	264,1620	2.0	0.30	Regular	0.24	0.13	0.03	-0.004	L
17	264,1945	2.0	0.45	Regular	0.27	0.31	0.04	-0.010	L
18	265,1020	5.0	0.30	Regular	0.78	0.45	0.40	-0.014	C.I
19	265,1200	5.0	0.50	Regular	1.62	0.41	0.38	-0.211	M.E
20	265,1810	3.25	0.30	Groups	0.40	0.45	0.15	0.025	I
21	266,0940	3.25	0.60	Groups	1.02	0.72	0.41	0.167	C
22	266,1230	3.5	0.55	Regular	1.12	0.98	0.11	0.015	M.E

Table 3.1: Summary of wave conditions for the runs in the Ottawa National Research Council Wave flume, September 1993 experiment. T is the period at which the wave paddle was driven (for JONSWAP spectrum waves it was the maximum wave energy period of the wave paddle driving signal), H is the wave height at the wave paddle, θ_s is Shields parameter (± 0.04), S and A are surface elevation skewness and asymmetry from the Capacitance wave gauges (with uncertainties of approximately 5 % for regular and groupy waves, 15-20 % for JONSWAP waves, as discussed in the text), and Δu_s is the difference in on and offshore velocities after removal of the mean (± 0.04 cm/s). Also included in this table is the dominant bedform type observed to form under these waves. For a key to the bedform symbols, see the Introduction. Run 14 was unique in that the waves were generated with the wave paddle in flapper mode rather than the piston mode used in all the other runs.

few exceptionally large waves was chosen to study the effect of wave breaking (Figure 3.16). The skewness is larger for the JONSWAP and Group waves in the 1995 data set. The wave groups were constructed artificially using cosine tapering on 3.5 second waves. This led to large variations in the water depth (due to radiation stress under the wave groups) which altered the total wave skewness significantly. These 'bound' waves did not appear to contribute to bed formation, as similar bedforms were observed under groups and regular waves with the same peak amplitudes, however, they did modify the calculated value of skewness. Attempts were made to filter these low frequency waves out of the wave record and the results of these efforts are listed in Table 3.2.

3.3 Combined Wave-Bedform Results.

Time sequences of wave parameters and bedform types have been plotted for the field data to demonstrate the sequence of bedforms observed. In the wave tank a similar sequence of bedform types was observed as a function of wave height, or Shields parameter. All the data have been plotted as a function of dimensionless parameters. Distinctions are made between the data of the three different experiments by using different symbols.

3.3.1 Burley Beach.

Examples of the bedform classes observed at the rise and decline of the storms at Burley Beach are shown in Figures 3.17 and 3.18. These figures list the bedforms observed over the 18 hour periods at the beginning of the second storm and end of the third storm. Plotted on the same time scale are the Shields parameter and velocity skewness as calculated from the Marsh-McBirney current meter data.

As discussed in the previous figure, more than one ripple type has been listed for many of the times because more than one ripple type was often observed in the same image. Thus the stability criteria for the different bedforms appear to overlap

Run	Day, Time	T(s)	H(m)	Wave Type	θ_s	S	A	Δu_s	Bed
18	188a,1355	3.5	0.40	Groups	0.36	0.52	0.08	-0.04	I
19	188b,1455	3.5	0.32	Groups	0.23	0.40	0.04	-0.03	I,L
25	189a,0855	3.5	0.32	Groups	0.25	0.41	0.08	-0.01	L,I
26	189b,1040	3.5	0.40	Groups	0.33	0.50	0.09	-0.03	I
27	189c,1150	3.5	0.50	Groups	0.40	0.61	0.09	-0.05	I,C
28	189d,1300	3.5	0.60	Groups	0.51	0.74	0.22	-0.02	C
29	189e,1430	3.5	0.70	Groups	0.56	1.22	0.24	-0.02	C,M
30	189f,1540	3.5	0.80	Groups	0.66	1.03	-0.10	-0.02	M
37	190e,1649	3.5	0.30	regular	0.29	0.35	-0.04	-0.02	L,I
54	191a,1505	3.5	0.50	JONSWAP	0.17	0.58	-0.20	0.00	I,L
55	191b,1545	3.5	0.60	JONSWAP	0.20	0.58	0.18	0.01	I
56	191c,1615	3.5	0.70	JONSWAP	0.25	0.52	0.00	0.01	I,C
59	192a,1125	3.5	0.20	Groups	0.08	0.21	0.02	0.00	L
60	192b,1230	3.5	0.25	JONSWAP	0.25	0.47	0.10	-0.02	L
62	192d,1425	3.5	0.40	Groups	0.33	0.47	0.07	-0.03	I
63	192e,1500	3.5	0.40	JONSWAP	0.20	0.61	0.03	-0.01	I,L
64	192f,1535	3.5	0.40	Regular	0.38	0.34	-0.03	-0.07	I
65	192g,1615	3.5	0.40	Groups	0.41	0.52	0.07	-0.04	I,C
66	192h,1645	3.5	0.50	JONSWAP	0.25	0.63	-0.10	-0.01	I
68	193a,1200	3.5	0.50	Regular	0.52	0.40	-0.08	-0.09	C
69	193b,1235	3.5	0.50	Groups	0.51	0.62	0.15	-0.03	C
70	193c,1300	3.5	0.60	JONSWAP	0.26	0.40	0.20	-0.01	I
71	193d,1330	3.5	0.60	Regular	0.84	0.50	0.01	-0.08	M
72	193e,1355	3.5	0.60	Groups	0.63	1.00	0.25	-0.05	M
73	193f,1425	3.5	0.70	JONSWAP	0.29	0.52	0.02	-0.01	C
74	193g,1500	3.5	0.70	Regular	0.87	0.63	0.04	-0.11	M
75	193h,1540	3.5	0.70	Groups	0.65	0.99	-0.08	-0.03	M

Table 3.2: Summary of wave conditions for the runs in the Ottawa'95 experiment. T is the period at which the wave paddle was driven (for JONSWAP spectrum waves it was the maximum wave energy period of the wave paddle driving signal), H is the wave height at the wave paddle, θ_s is Shields parameter (± 0.04), S and A are surface elevation skewness and asymmetry from the Capacitance wave gauges (with uncertainties of approximately 5 % for regular and groupy waves, 15-20 % for JONSWAP waves, as discussed in the text), and Δu_s is the difference in on and offshore velocities after removal of the mean (± 0.04 cm/s). Also included in this table is the dominant bedform type observed to form under these waves. For a key to the bedform symbols, see the Introduction.

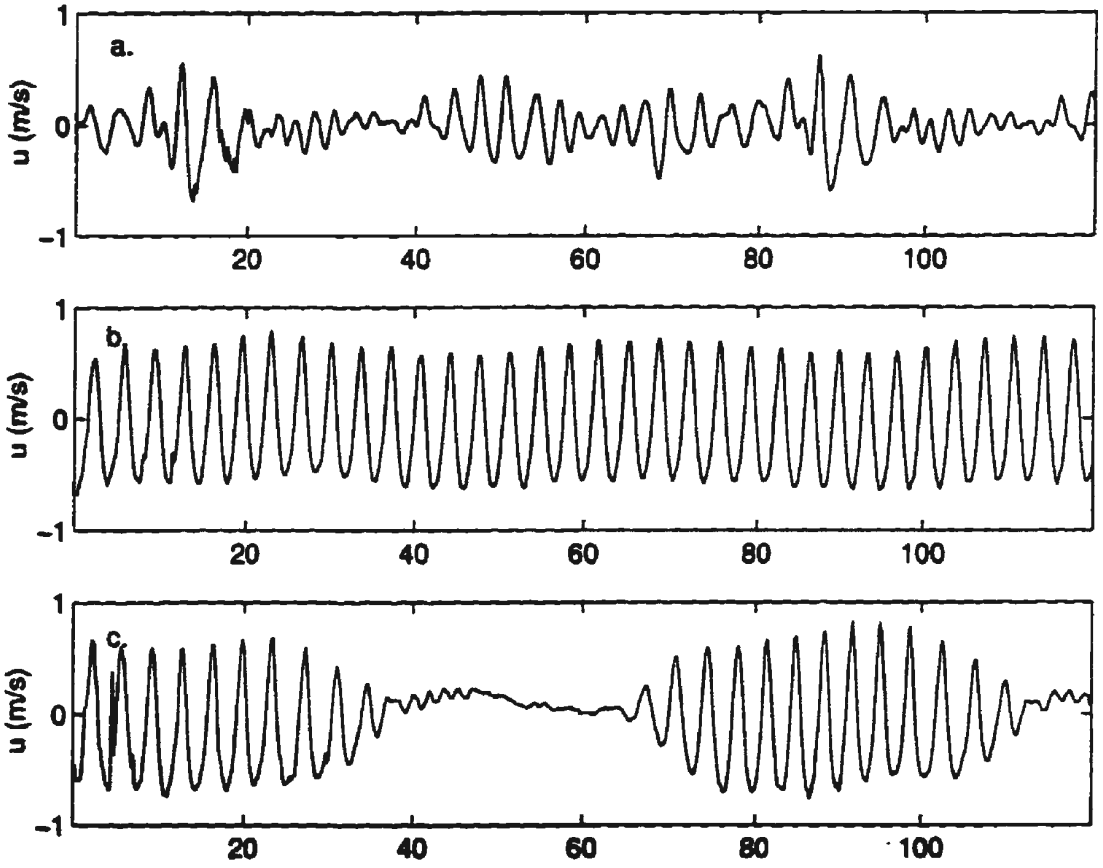

Figure 3.16: Two minute time series of ADV data for three different runs. In (a) the data from run 70 shows JONSWAP spectral type waves with a significant wave height of .60 meters. (b) shows the data from run 71, where regular waves of nominal height 0.60 meters were run (heights deviate somewhat due to peakiness, or Stokes interactions). (c) shows the wave groups formed by cosine tapering a group of fifteen waves with thirty second gaps between each group. For 3.5 second waves a wave height of 0.60 m generates a maximum velocity of approximately 0.6 m/s.

under natural, irregular waves. The criterion for the difference between relict ripples and linear ripples was not very strict in the field. Under natural, irregular waves the ripples may be active for short periods under

large groups, then inactive, so there is some latitude of interpretation in this classification step.

3.3.2 Effects of Currents

The effects of currents on the formation of various ripple types is difficult to determine because vertical structure in the flow field means that the currents acting on the bed may be quite different from those in the bulk flow. The fact that similar bedforms were observed in the Ottawa wave tank as in the field for similar wave conditions indicates that longshore currents are not necessary for the formation of any of the bedforms in Clifton's classification scheme. Some small secondary cross-tank circulations were noted in the wave tank under regular waves, but not under irregular waves. As shown in Figure 3.21, cross-shore mean currents in the bulk of the fluid show an off-shore trend, as expected from the need to balance the wave induced on-shore mass-transport on the surface. Figures 3.19 and 3.20 show that at Burley Beach small scale ripples such as cross-ripples are found before strong currents start and after strong currents have abated, however, further field data are needed before conclusions can be drawn.

Alongshore currents show some correlation with the alongshore component of the wave action. However, there is some difference between the southward (positive) and northward flows. This may be due to differences in the period of the waves, as waves travelling southward have a much greater fetch and hence longer periods, which may have moved the breaker zone and peak of the longshore current seaward of the current meter during the height of the storms. The central point to note in Figures 3.19, 3.20 and 3.21 is that cross-ripples occurred in the Burley Beach data only at very small values of mean current.

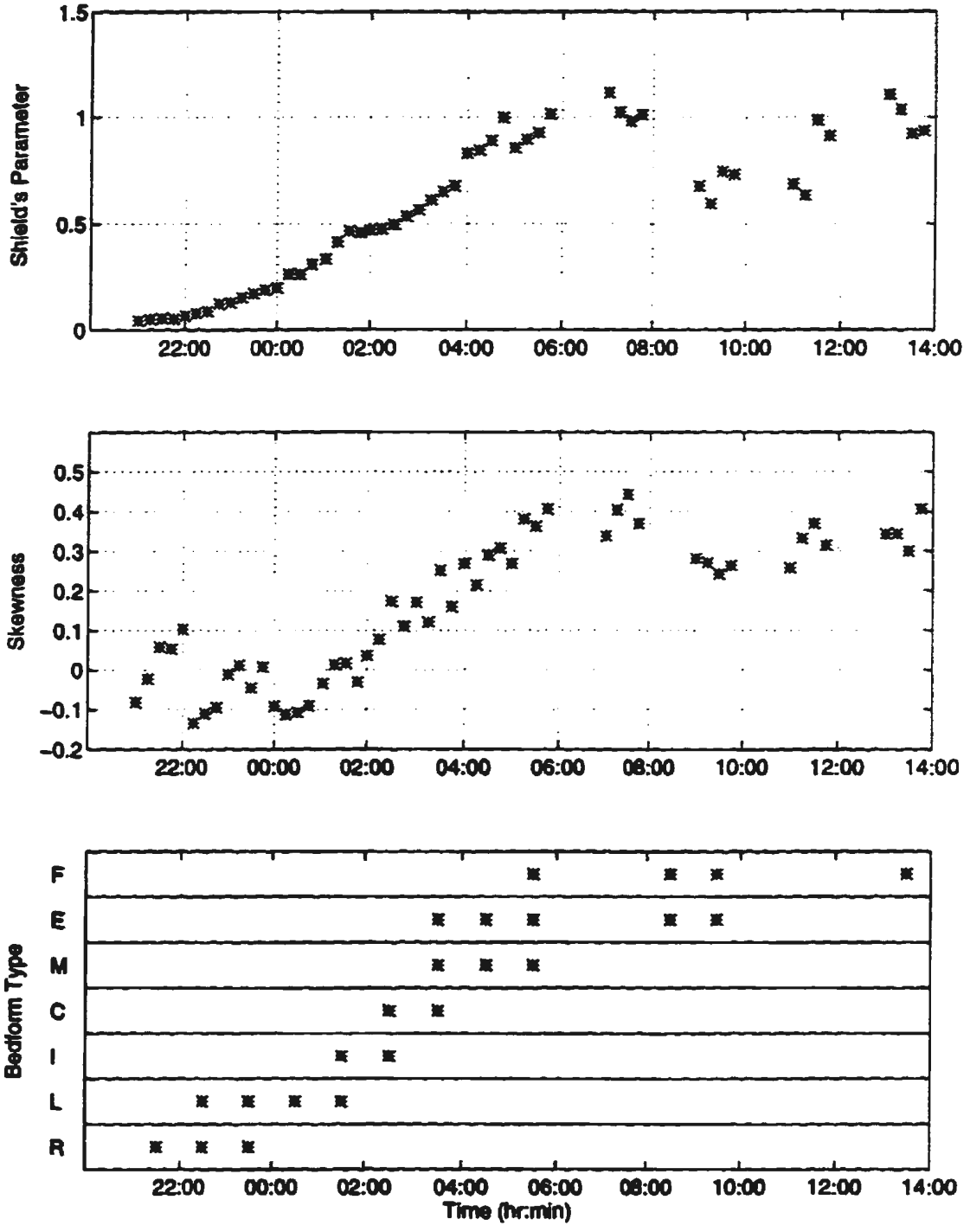

Figure 3.17: Summary of bedform types and current meter data for October 22, the start of the second storm. R, L, I, C, M, E, and F stand for: Relict ripples from a previous storm, Long-crested ripples, Irregular ripples, Cross-ripples, megaripples, Evanescent (short lived) ripples, and Flat bed respectively.

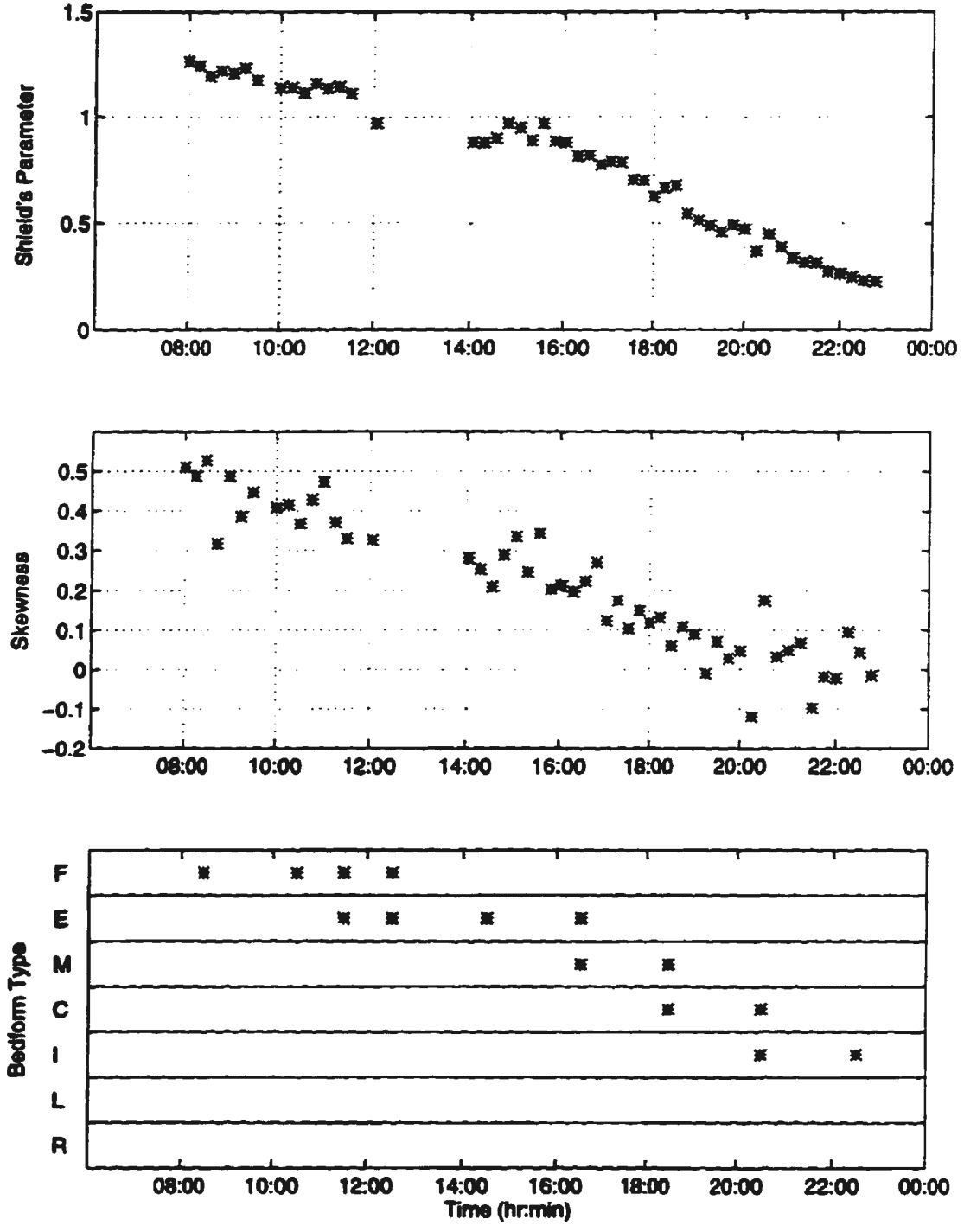

Figure 3.18: Summary of bedform types and current meter data for October 25, the end of the third storm.

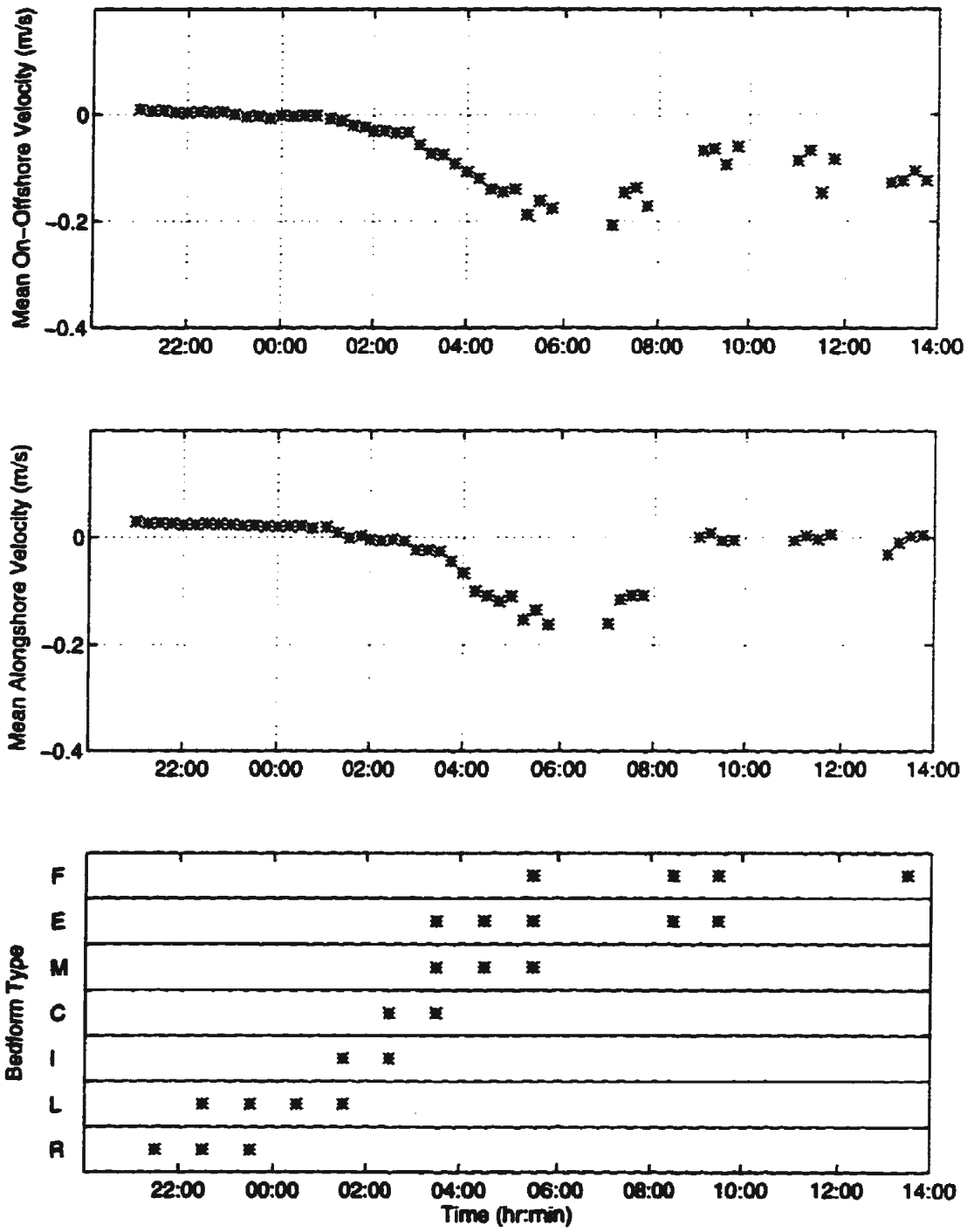

Figure 3.19: Summary of bedform types and mean currents for October 22, the start of the second storm. Mean currents were obtained from fifteen minute averages of Marsh McBirney current meter CM849, approximately 25 cm above the bottom. The bedforms have been classified as R, L, I, C, M, E, and F as in the previous figure.

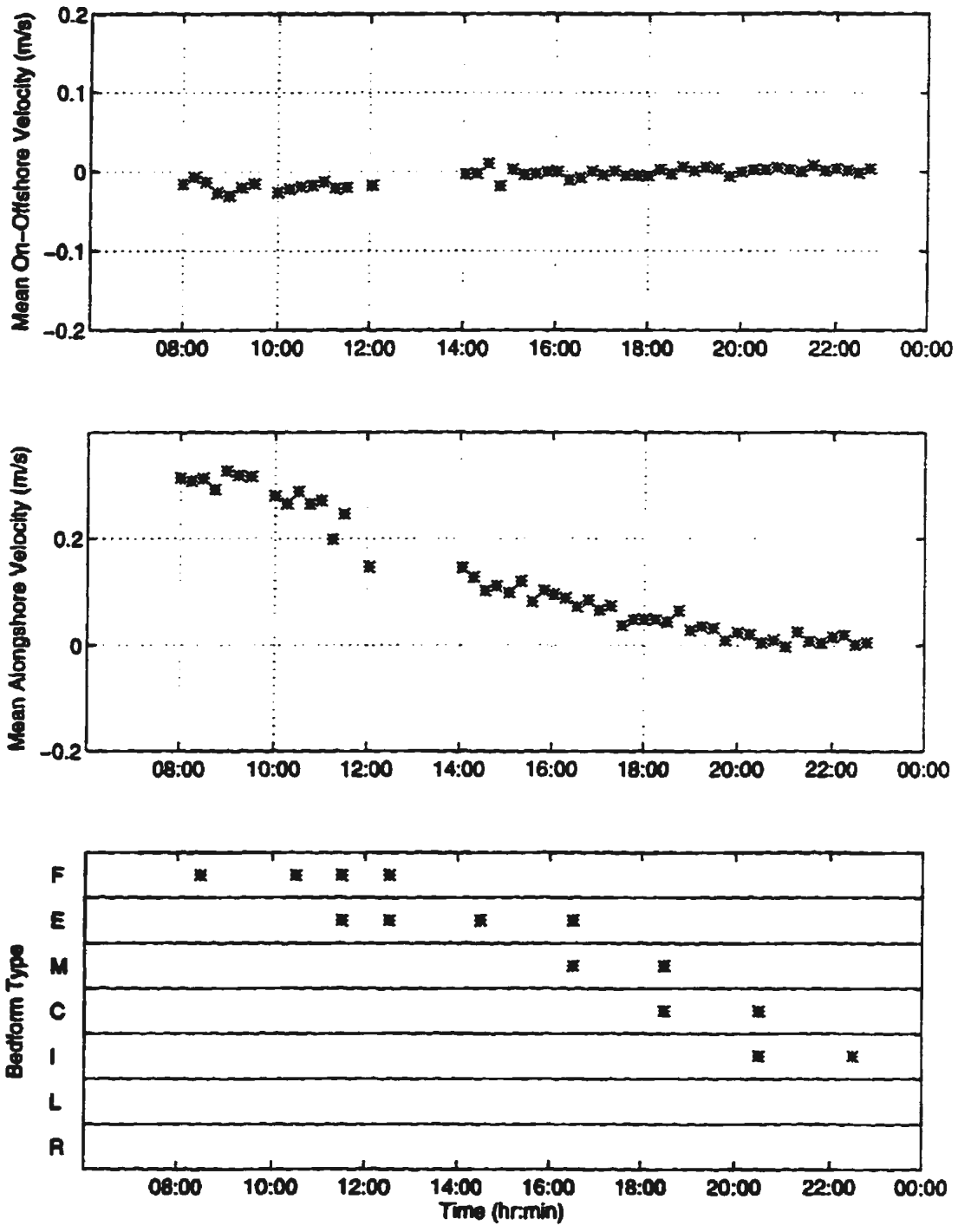

Figure 3.20: Summary of bedform types and mean currents for October 25, the end of the third storm. Mean currents were obtained from fifteen minute averages of Marsh McBirney current meter CM849, approximately 50 cm above the bottom.

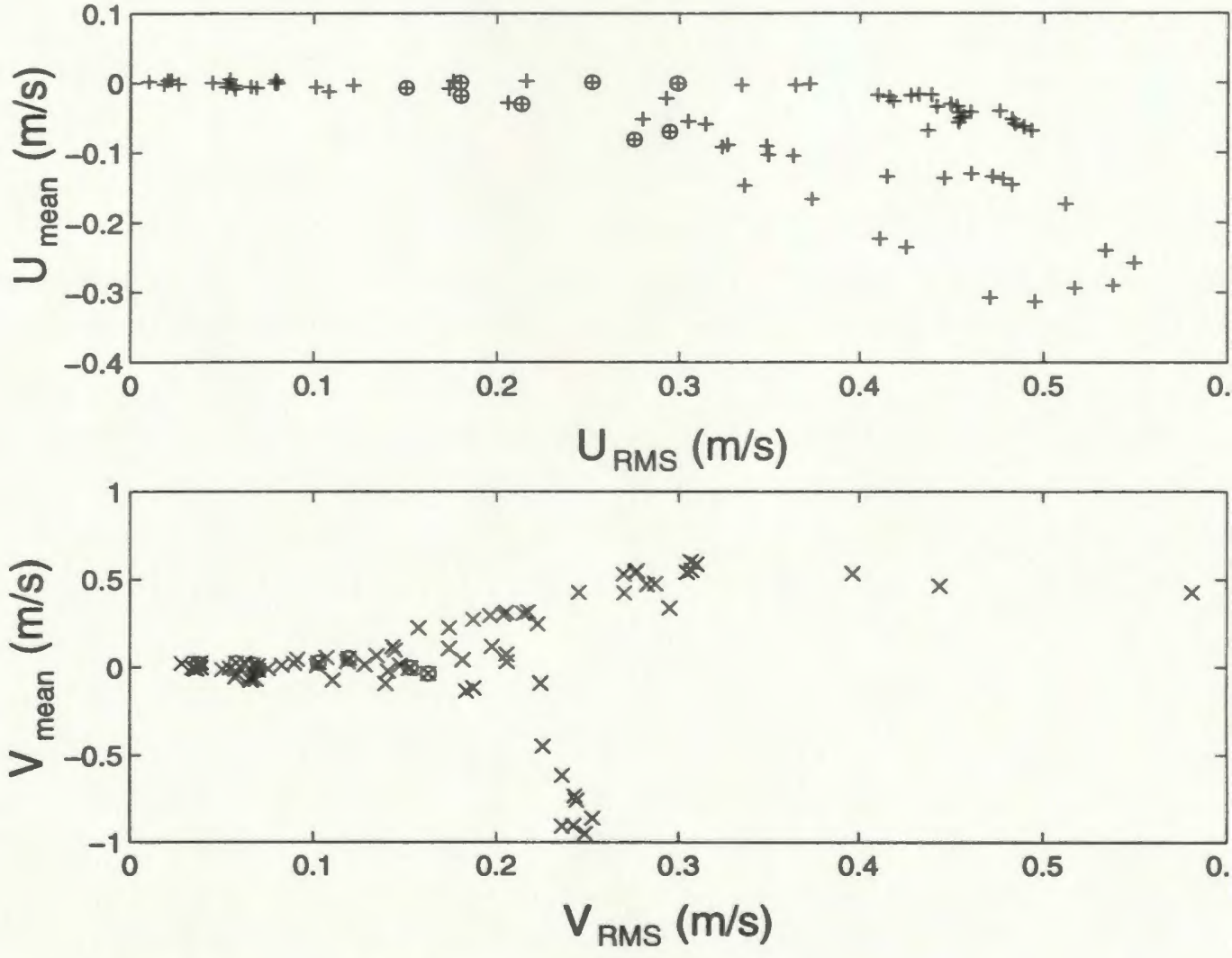

Figure 3.21: Summary of mean currents in the on-offshore and longshore directions at Burley Beach as a function of RMS wave velocity in the on-offshore and longshore directions. Note the different vertical axis scales for on-offshore and longshore directions. Each point represents a 50 minute record, and the points for times when cross-ripples were the dominant bedform have been circled.

3.3.3 Infra-gravity Energy.

There is growing interest in the contribution of infra-gravity frequency waves to sediment transport and bedform development (see for example Beach and Sternberg 1988). For the purpose of this study, infra-gravity waves are defined as surface gravity waves of periods greater than about 20 seconds. They are typically associated with different forcing mechanisms than the incident wind waves, including edge waves, bound waves associated with wave groups and shear waves associated with instability in the longshore current shear. A measure of infragravity wave action was obtained by low pass filtering (using an 8th order Butterworth filter with a 0.05 Hz cutoff) the velocity records from CM849 taking the standard deviation of the resulting low frequency signal.

The RMS infragravity wave velocities presented in Figures 3.22 and 3.23 have been obtained from the 50 minute long records, with stars plotted at the center of the interval. Velocities associated with the infra-gravity frequency band slowly fall off near the end of the storm, but remain at roughly 0.1 m/s during the cross-ripple formation period. In the start of the second storm, velocity associated with infra-gravity frequencies are somewhat slow to start up, but are between 0.06 and 0.1 m/s during cross-ripple formation.

Results for RMS velocities in the infragravity frequency band from the entire Burley Beach CM849 data set are shown in Figure 3.24 plotted as a function of the on-offshore and long-shore RMS velocity. On-offshore velocities have been plotted as +, and longshore velocities as ×. The data runs (each of which represent approximately one hour of data) in which cross-ripples occurred have been circled. During periods of energetic incident waves, infragravity frequency velocities were approximately 1/5 to 1/3 the total velocities in the on-offshore direction and 1/4 to 1/2 in the long-shore direction. During less energetic periods such as those when cross-ripples were present, this fraction was reduced to 1/10 to 1/4.

Similar calculations done for the Ottawa'95 experiment have been plotted in Figure 3.25. The infragravity RMS velocity has been plotted as a function of total RMS

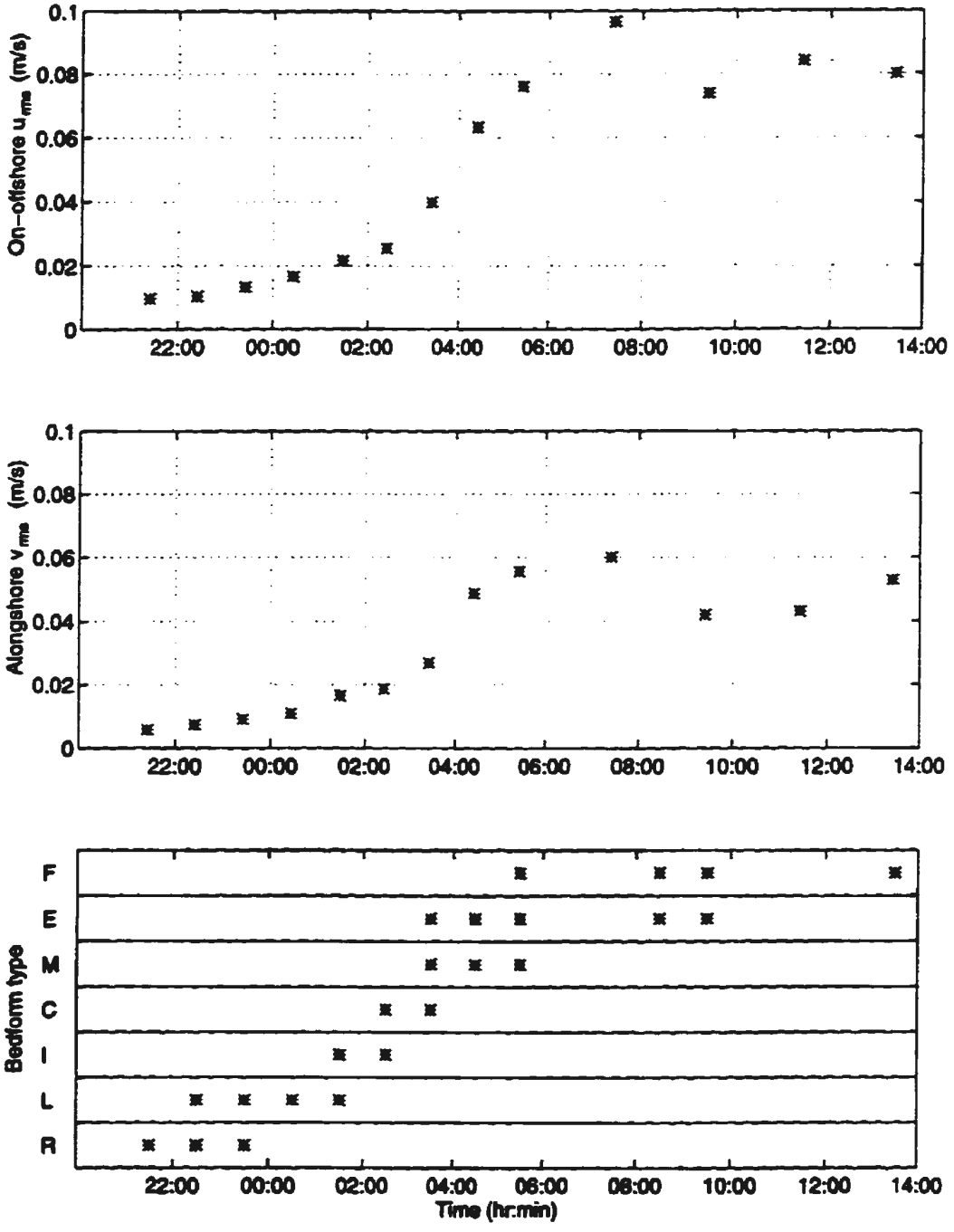

Figure 3.22: The upper two graphs show time series of Infra-gravity frequency root mean square velocities in the on-offshore and along-shore directions for the beginning of the second storm at Burley Beach 1992. Plotted in the lower graph is the dominant bedform type corresponding to the same time period.

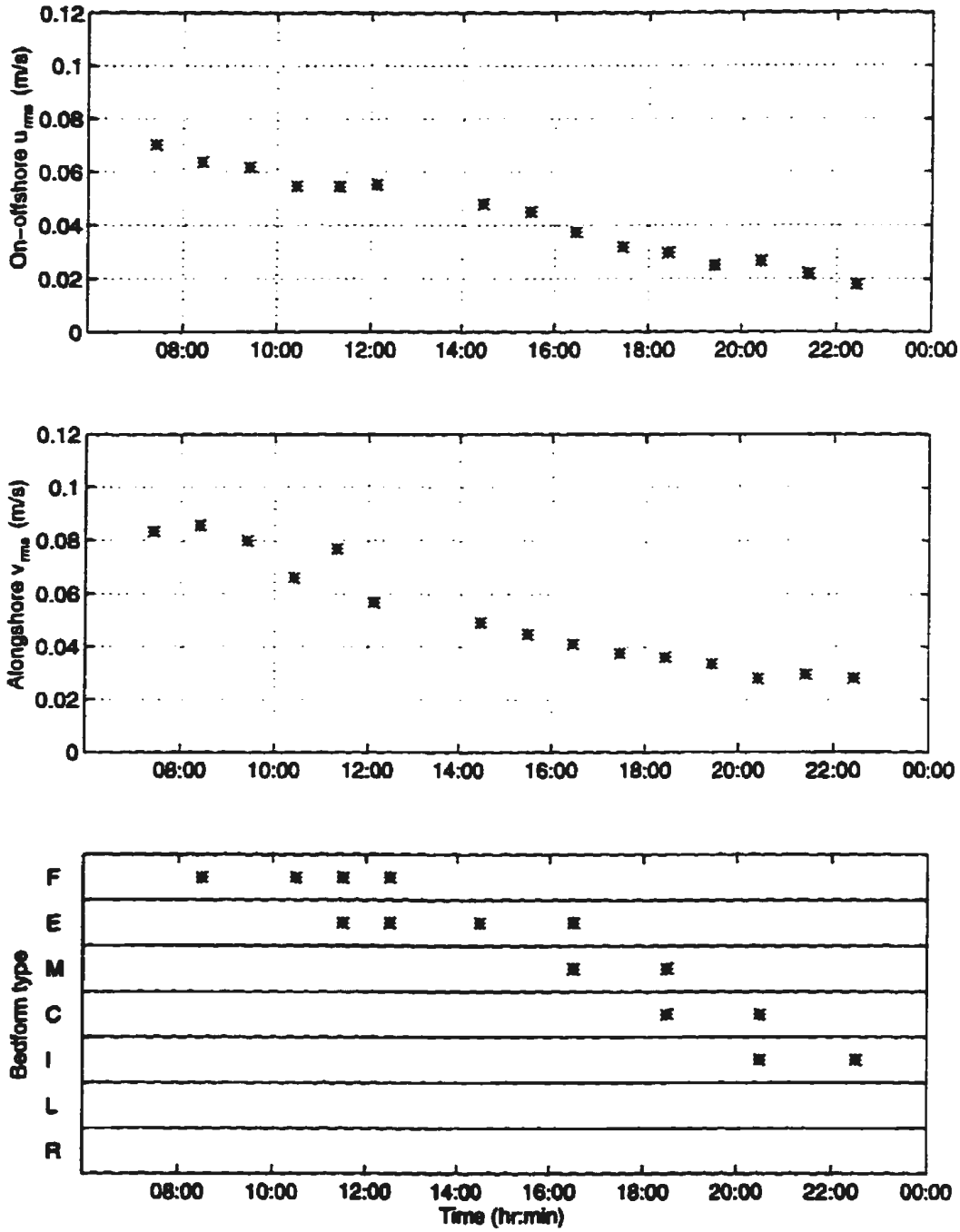

Figure 3.23: The upper two graphs show time series of Infra-gravity frequency root mean square velocities in the on-offshore and along-shore directions for the end of the third storm at Burley Beach 1992. Plotted in the lower graph is the dominant bedform type corresponding to the same time period.

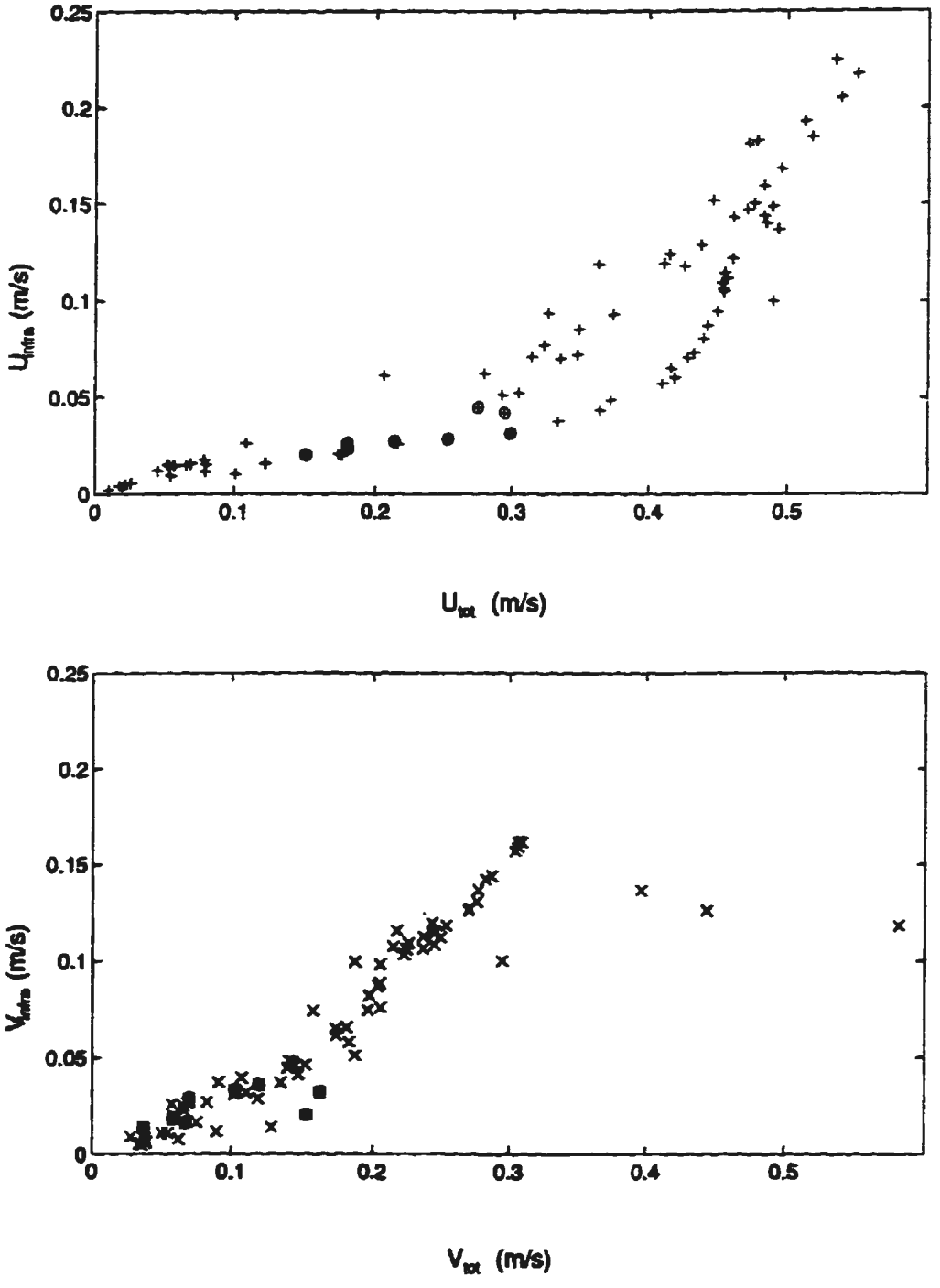

Figure 3.24: A comparison of infragravity frequency rms velocity u_{infra} and v_{infra} with total rms velocity u_{tot} and v_{tot} for all the 55 minute wave records from the Burley Beach experiment. On-offshore velocities have been plotted as +, and longshore velocities have been plotted as ×. The wave records in which cross-ripples were observed have been circled.

velocity for each wave run. There is a strong correlation of infra-gravity frequency wave velocity and wave pattern. The regular waves (plotted as +) had low RMS infra-gravity velocity, less than 10% of the total RMS velocity (or 3% of the wave energy, which is proportional to the square of the RMS velocity), while the JONSWAP and the cosine tapered group wave patterns (plotted as $*$ and $\times$) had much larger infra-gravity wave velocities, especially in the larger waves. As discussed in the previous section, these infragravity waves were due to 'bound' waves, (Longuet-Higgins and Stewart 1964) and wave tank seiches, and were the cause of anomalous values of skewness, while the regular waves would only have the wave tank seiche generated by the start of the wave paddle.

There were almost no differences in ripple types and sizes noted between different wave patterns of similar Shields parameter. This indicates that ripple pattern is not sensitive to infra-gravity frequency motion in the cross-shore or long-shore directions.

3.3.4 Bedform Type and Dimensionless Parameters.

Field and wave tank ripple observations have been plotted as a function of Shields parameter in Figure 3.26. Results from the wave tank were similar to the field results for the larger, 0.15 millimetre sand (open circles) in Figure 3.26, but rather different for the fine sand, Ottawa'93 runs (plotted as stars). Shields parameter has both an explicit inverse relationship to the median sand grain size and an implicit weakly positive relationship to grain size through the Jonsson friction factor (which increases approximately 20 % between grain sizes of 0.1 mm and 0.2mm), so these plots tend to be fairly sensitive to this value. In the field sand grain sizes may have changed somewhat during the periods of erosion and deposition at the height of the storms, but the difference in the two wave tank experiments is harder to explain. It is possible that biological fouling increased the effective grain size (Grant and Gust, 1987), or that the fines in the Ottawa'93 experiment provided some cohesive effects which influenced the bedforms to the equivalent of larger grain sizes. Crest to crest lengths in the 1993 experiment were considerably larger than were predicted for .09 millimeter

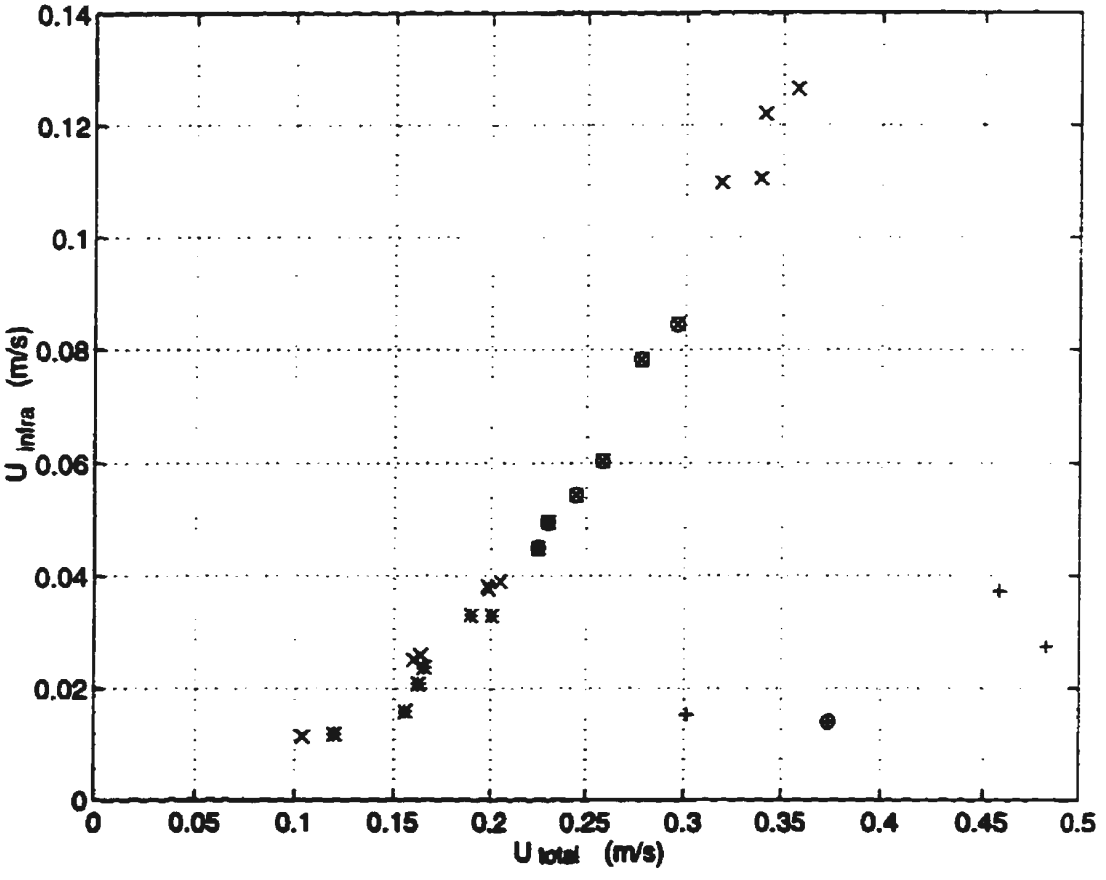

Figure 3.25: A comparison of infragravity frequency rms velocity u_{infra} with total rms velocity u_{total} for each of the wave runs in the Ottawa'95 experiment. Regular wave type runs have been plotted as stars, group wave type runs have been plotted as crosses, and irregular type wave runs have been plotted as pluses. Those runs which produced cross-ripples have had their symbols circled.

sand, further supporting the idea that the grain size-ripple form scaling breaks down or is different for this sand.

The relationship between wave velocity skewness and bedform type has been plotted in Figure 3.27. In trend the skewness follows Shields parameter. This is not surprising given that the wave period and depth do not change very much over the data presented. Though there is again considerable scatter in the results, it would appear that cross-ripples do not appear for skewness less than 0.1, on average. The fact that cross-ripples and megaripples have not been observed in the studies done in deeper waters tends to confirm that the wave skewness and asymmetry induced by the shallow water is influential in forming these bedforms. Furthermore, the observations of cross-ripples at relatively low values of wave asymmetry both in the field and in the wave-flume indicates that skewness is of greater influence than asymmetry in cross-ripple generation.

A comparison between the field skewness and laboratory skewness indicate that for a given Shields parameter, the skewness in the laboratory is greater. This is in keeping the theory and with the observations of others that for a given wave height and period, skewness increases with decreasing water depth (for example Guza and Thornton 1985). As can be seen from Tables 3.1 and 3.2, for a given Shields parameter there is considerable variation in skewness according to which wave type (JONSWAP, grouped, or regular) is being run. As discussed previously, some of this skewness may have been leakage from lower frequency motions in the wavetank, and some of the skewness variability may come from the short length of the time series available. This makes conclusions drawn from wavetank skewness values rather tentative.

3.4 Conditions of Formation of Cross-Ripples.

Cross-ripple formation was observed during the rise and fall of each of the storm events during the Burley Beach experiment, and for a specific range of wave heights in each of the Ottawa wave tank experiments. The Shields parameter range for

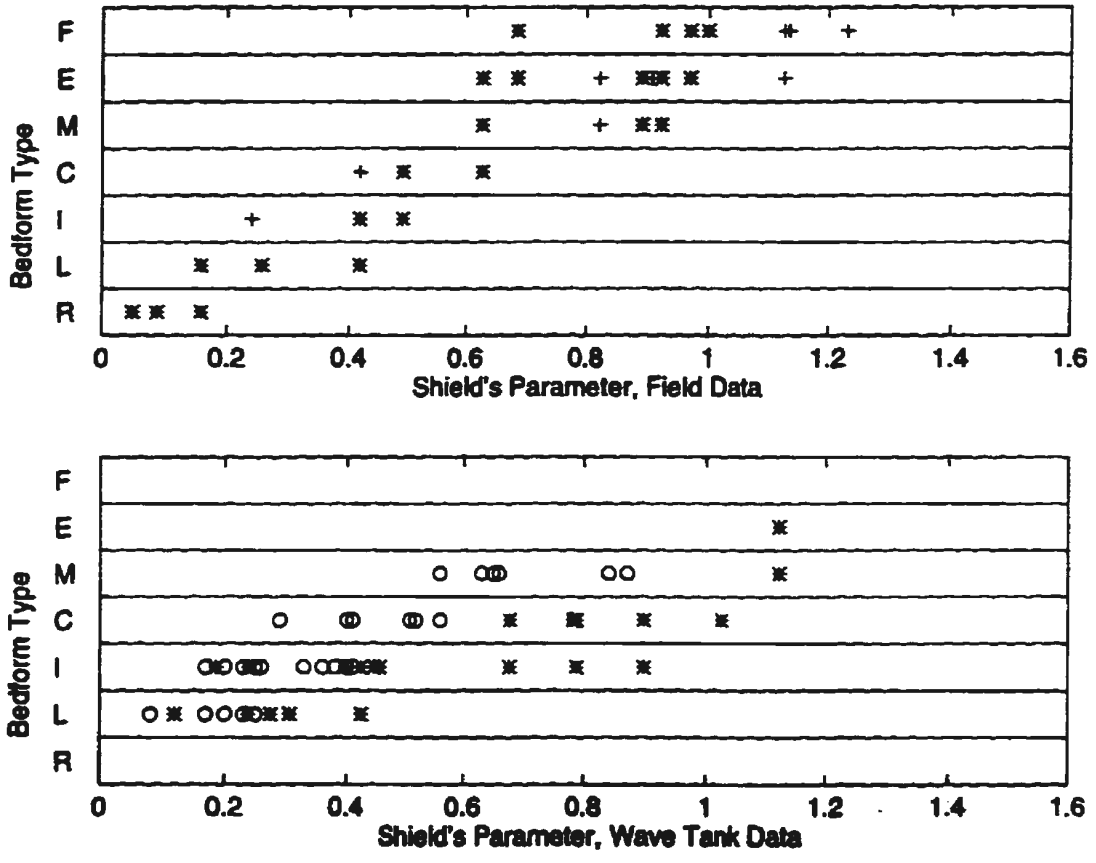

Figure 3.26: Summary of bedform types and as a function of Shields parameter for field data and wave tank data. The field data (for which the median sand size was 0.170 mm) have been plotted as crosses for the beginning of storm 2, and stars for the end of storm 3. The wave tank data has been plotted as stars for the Ottawa'93 experiment (sand size 0.095 mm), and open circles for a portion of the Ottawa'95 experiment (sand size 0.15 mm).

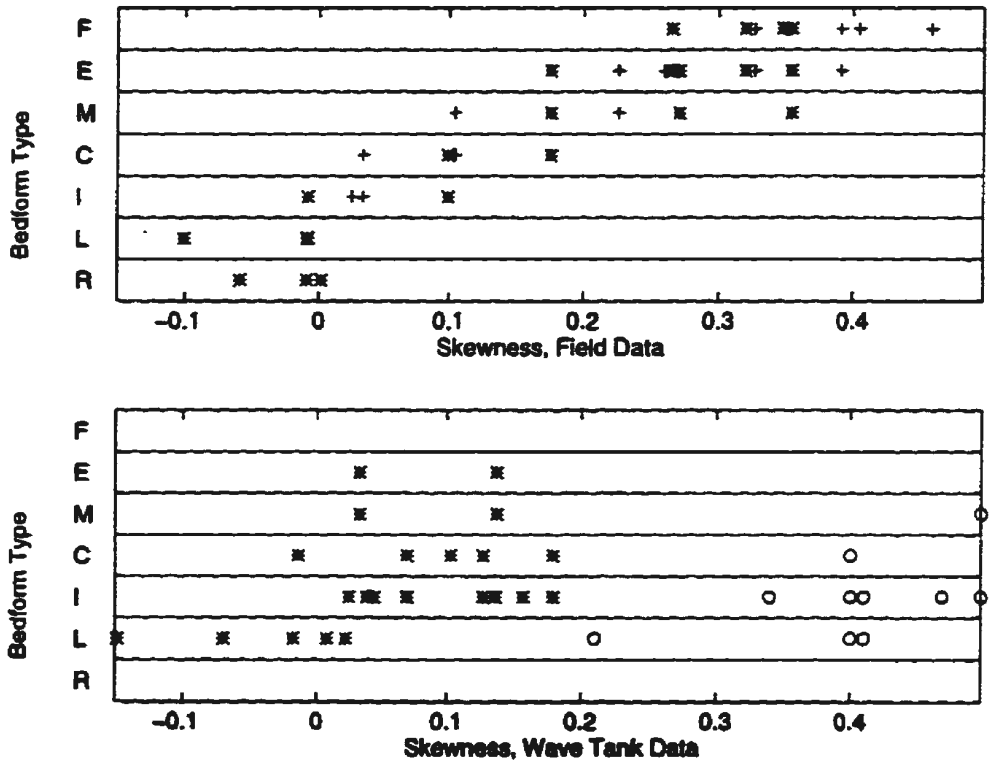

Figure 3.27: Summary of bedform types and as a function of wave velocity skewness for field data and wave tank data. The field data (for which the median sand size was 0.170 mm) have been plotted as crosses for the beginning of storm 2, and stars for the end of storm 3. The wave tank data has been plotted as stars for the Ottawa'93 experiment (median sand size 0.095 mm), and open circles for a portion of the Ottawa'95 experiment (median sand size 0.15 mm).

the formation of cross-ripples appears to change with sediment grain size, as seen by comparing results in the two wave flume experiments. Likewise, velocity skewness and asymmetry are largely a function of wave height for a given wave period and water depth, so cross-ripples appear for a certain range of these parameters. Cross-ripples were not seen to form under strong long-shore currents, although, once again, the long-shore current is largely a function of incident wave energy. Long-shore current is also a function of incident wave direction, but unless the wave direction changes on the scale of the cross-ripple dimensions, the wave direction alone should have little effect on cross-ripple formation.

3.5 Comparison With Previous Results.

Comparisons are also possible with results from the theories summarised in the Introduction. This sort of comparison shows some of the strengths and shortfalls of the currently available theories, and thus points the way towards further refinement of these theories.

The summaries of the data in the literature typically only consider linear, long-crested ripples and short crested, or irregular ripples, and are usually classified according to a mean crest-crest length and crest-trough height, with some consideration to the symmetry in the ripple profile. In the nearshore, ripples are usually considered to be of anorbital type (Nielsen 1981), so their crest-crest length is a function of the sand parameters and not of the orbital diameter of the waves. In the data presented here, all orbital diameters were much larger than the crest spacing. According to the Wiberg and Harris (Wiberg and Harris 1994) and Clifton and Dingler (Clifton and Dingler 1984) classification criteria, many of the ripples observed in the three experiments presented here fit into the "sub-orbital" class. Crest to crest lengths for linear and irregular ripples in this study were typically 11, 8, and 10 cm for the Burley Beach, Ottawa'93, and Ottawa'95 experiments respectively.

The Wiberg-Harris semi-empirical theory (equation 1.11) shows very good agreement with experiment, as it predicts the crest-crest lengths to be 10.7, 7.5, and 9.6 cm for typical long and short-crested anorbital ripples at Burley Beach, Ottawa'93 and Ottawa'95 respectively. The Nielsen (1981) and Grant and Madsen (1982) theories over or underpredict the crest-crest spacing, particularly for the Ottawa'93 experiment. For example, where Nielsen's laboratory theory, equation 1.6, predicted ripple spacing of 14 cm for regular (laboratory) waves and Nielsen's theory for ripples in the field, equation 1.8, predicted 3.6 cm for irregular (field) waves.

Previous studies have concluded that ripples are planed off for Shields parameter greater than one (Nielsen 1981). Field and wave tank ripple observations have been plotted as a function of Shields parameter in Figure 3.26. The field ripples occurrence falls within the Shields parameter bounds of previous data available for ripples (wherein ripples appear at Shields parameters less than 1-1.2), though lunate megaripples and evanescent ripples dominate at Shields parameters greater than 0.7. As noted earlier, results from the wave tank were similar to the field results for the larger, 0.15 millimeter sand (open circles) in Figure 3.26, but rather different for the fine sand, Ottawa'93 runs (plotted as stars). There are very few published results in the literature for sand of this size. The graphs in Yalin and Karahan (1978) indicate a trend to the breakdown of Shields parameter scaling of bedforms as the median sand size gets smaller than 0.1 mm, but provide no suggested mechanisms for this breakdown. The ripple pattern results also suggest that there is a breakdown in the Shields parameter scaling. Cross-ripples and lunate forms appear for relatively high Shields parameter (0.9 to 1.1) in the Ottawa'93 results, and ripple patterns have the same sequence as those observed in larger sands but at higher Shields parameters in the Ottawa'93 experiment. This breakdown in Shields parameter scaling in fine sand which may be of interest in future studies.

Chapter 4

Computer Simulations.

Further understanding of the mechanisms of formation of cross-ripples and other bedforms may be obtained through the use of computer models. Recent work using computer simulations has suggested that self-organisation is an important mechanism in the formation of aeolian sand ripples (Landry and Werner 1994, Nishimori and Ouchi 1993). In these simulations, grains or groups of grains were followed and parameters and different physical forcing effects have been altered or removed to establish which are dominant. Though the scales of motion are different between aeolian and aqueous sand ripples, the basic motions of the sand grains are analogous. Thus a coupled map lattice type model of aeolian ripple formation due to Nishimori and Ouchi has been modified and adapted to help determine that self-organization and velocity asymmetry play a role in the formation of different ripple types.

4.1 The Modified Nishimori-Ouchi Model.

To adapt the Nishimori-Ouchi model to the undersea environment, their large scale model II (used to describe barchan sand dunes) was modified by adding periodic forcing and altering the scales of relevent parameters. The Nishimori-Ouchi model uses two mechanisms for the movement of sand: saltation and creep. Both of these mechanisms occur for sand in the nearshore subaqueous environment, though different

length scales are associated with each of these motions due to the different densities of air and water. The forcing in the Nishimori-Ouchi study was constant. In this study the forcing varies with time, so the model must also contain relationships between the forcing amplitude (as related to the wave velocity through a turbulent bottom shear stress term) and the other model parameters. Other modifications include separate coefficients for transverse and along-flow saltation, or hop distance, the addition of transverse flow (to simulate long-shore currents), and adoption of a parameter range suitable to the scales and forces in the undersea environment.

The model has been formulated as a discrete model in space and time with an array of continuous field variables $H(x_i, y_j)$ which represent the average bed elevation centered about each point x_i, y_j (Note that arrays are denoted by capital letters, and scalar constants by lower case). It is stepped forward in time through two alternating saltation and creep substeps. The saltation substep simulates the hopping of sand by subtracting a quantity of sand $Q(x, y)$ from each grid point x, y and adding it to a down-stream location $x + L_x(x, y), y + L_y(x, y)$. Thus the saltation substep in time step n of the model can be calculated in two steps by;

$$H_{n'}(x, y) = H_n(x, y) - Q(x, y), \tag{4.1}$$

$$H_{n''}(x + L_x, y + L_y) = H_{n'}(x + L_x, y + L_y) + Q(x, y), \tag{4.2}$$

where n' and n'' represent intermediate substeps. The variable Q has the dimensions of bed height due to the regular grid of the model and the neglect of variations in surface area due to slopes.

The model allows the saltation or hop distance $\vec{L}(x, y)$ and amount of sand moved per unit time $Q(x, y)$ for each grid square x, y to be a function of the local bed slope. If the forcing is defined to be in the $\pm x$ direction, these functional relationships are given by

$$\vec{L}(x, y) = \vec{L_o} - \beta_L \nabla H(x, y), \tag{4.3}$$

$$Q(x, y) = Q_o + \beta_q \frac{\partial H(x, y)}{\partial x} + \beta_{qt} \left| \frac{\partial H(x, y)}{\partial y} \right|, \tag{4.4}$$

where $\vec{L}_o$ and Q_o are constants which reflect the average saltation distance and quantity of sand moved in a time step if the bed were flat. $\nabla H(x,y)$ is the two dimensional gradient of the bed elevation $H(x,y)$. β_L, β_q and β_{qt} are adjustable parameters which are functions of the flow intensity and sand grain size. Note that the saltation length $\vec{L}$ and quantity of sand moved Q are both functions of the slopes in both the x and y directions.

The idea that L should be proportional to the slope of the starting point of movement stems from the fact that if the bedforms are sufficiently large, a sand grain moving upslope with a ballistic trajectory will collide with the surface after a shorter distance of travel than if the grain were moving to a downslope position. A similar effect is simulated in the direction transverse to the fluid flow, so that sand grains in motion tend to be deflected down transverse slopes due to gravitational effects (see, for example Fredsøe and Deigaard 1992, chapter 7.4).

The dependence of Q on slope can be understood as a first approximation to effects of the variation of shear stress on the bottom with slope. The regular derivative in the x direction reflects the increased shear on the stoss (upstream side) slopes, which will move larger quantities of sand, while the negative slopes on the lee side mean smaller amounts of sand are moved. The absolute value of the slope in the direction transverse to the flow direction reflects the increase in sediment mobility on transverse slopes due to lower critical shear stress for initiation of sand grain movement on transversely sloped surfaces (see, for example, Fredsøe and Deigaard 1992, chapter 7.3). There is also a slope effect due to the increase in surface area exposed to the flow on a sloped grid square as compared to a level one. This effect has been neglected in this model, though it follows the same trend as the other slope effects, except on the lee side, where shear stress effects are minimal anyway.

The second substep simulates small scale sand movements, or creep. For time step n, the creep substep consists of adding to each grid point a portion β_c of the difference in elevation between each grid point and the average of the eight nearest neighboring

grid points, hence smoothing localized bumps and filling grid scale hollows. In practice, this is accomplished using two dimensional convolution with a weighted filter C,

$$H_{n+1}(x_i, y_j) = H_{n'}(x_i, y_j) + \beta_c \left(\sum_{k=i-1}^{i+1} \sum_{l=j-1}^{j+1} H_{n''}(x_k, y_l) C(x_{k-i+1}, y_{l-j+1}) \right) \tag{4.5}$$

where C is given by:

$$C = \frac{1}{12} \begin{bmatrix} 1 & 2 & 1 \\ 2 & -12 & 2 \\ 1 & 2 & 1 \end{bmatrix}. \tag{4.6}$$

In the physical system being modelled the term β_c is related to the amount of time in each time step and the intensity of the saltation bombardment, or sediment flux.

Typically the model was run with a 104 by 107 point array initialized with very small amplitude randomly generated noise. The model was not sensitive to the amplitude of the initialization noise, so it was chosen to be of the order of the sand grain size, or 10^{-3} times the amplitude of the final state of the rippled bed. The model is then forward stepped in time using positive direction $\vec{L_{op}}$ for t_p time steps and then stepping t_n time steps using a reverse direction $\vec{L_{on}}$. This very simplified forcing can be justified by the fact that bedload transport is usually considered to be a function of at least the cube of the free stream velocity, so only the highest velocity parts of the wave cycle would contribute significantly to sand motion. More sophisticated model driving signals such as sinusoidally varying $\vec{L_o}$ and stochastically variable $\vec{L_o}$ are discussed in the Model Tests section.

It is reasonable to assume that the slope effect parameters β_L and β_q are functions of the shear at the bed, and hence $\vec{L_o}$ in the model. Unfortunately, these relationships are largely unknown. For this study a linear relationship has been chosen as a first approximation for each, such that $\beta_q = b_q \vec{L_o}$ and $\beta_L = b_e \vec{L_o}$. Note that this implies that the slope effect in the along-flow (x) direction β_{Lx} is the same as that in the transverse direction β_{Ly}. Calculations performed using Fredsøe and Deigaard's small

slope approximations indicate that for the flow regime considered here, β_{Lx} and β_{Ly} are of the same order of magnitude, but again, both are poorly constrained experimentally for oscillatory flow over ripples. The effect of changing the ratio of β_{Lx} to β_{Ly} in the model is discussed in the test results section.

A constant longshore current was added to the model by including a constant y component to $\vec{L}_o$. L_{oy} was chosen to be small compared to L_{ox} to correspond with the observations of cross-ripples. Increasing longshore currents to see if combined wave-current ripples are formed, or if there is a transition between forms (as Amos et al. 1988 seem to have observed) is an interesting area for further research with the model.

4.1.1 Model Parameters and Scaling.

The relationship between the model parameters and those measured in the field can be approximated by establishing *a priori* a physical scale for the grid spacing and the height variable (which need not have the same scale), then using known measurements for saltation length per unit time step for a given shear stress and quantity of sand moved for that same shear stress. For this study the scales of interest were to be equivalent to the Burley Beach experiment, hence a grid spacing of one cm intervals was chosen, such that five to ten ripples are modelled in the domain and there are ten to twenty grid points per ripple waveform. It was found that the model produced linear to lunate bedforms for hop lengths $\vec{L}$ of 5 to 18 grid spacings. If the time step size was chosen to be one second, then saltation velocities (hop lengths per time step) were 6 to 18 cm/s. An effective Shields parameter for the model runs can be derived from Nielsen's semi-empirical relationship for bedload velocity (Nielsen 1992, p.115)

$$u_B \simeq 4.8 u_*. \tag{4.7}$$

Since the Shields parameter is

$$\theta_s = \frac{u_*^2}{(s-1)gd}, \tag{4.8}$$

the Shields parameters for which the model produces bedforms is between 0.1 and 0.6, in reasonable agreement with those observed in the field and wavetank studies.

The notion that saltation velocities would be closely related to shear stress velocity is supported by high speed photographic evidence (Fernandez-Luque and VanBeek 1974, for example) and theoretical trajectory calculations (Wiberg and Smith 1985). These studies also indicate that typical trajectories of saltating sand grains in water have a maximum height of one to three grain diameters, and lengths of ten to thirty grain diameters. These distances are significantly less than those modelled by $\vec{L}(x,y)$. For sand of 0.017 cm grain size a long hop is approximately 5 mm. At a speed of 15 cm/s this hop occurs in 0.033 seconds. However, in unidirectional currents and in the Ottawa wave flume, grains are often seen making many hops before coming to rest. In effect the coarse scale of the model serves to approximate these many small bouncing hops with one movement. It is not known how closely related the trajectories of subsequent hops are to the initial hop. In this model they are assumed to be the same (i.e. no bed effect on subsequent hops).

The units for the bed elevation variable $H(x,y)$ can also be chosen to be centimeters. Once this scale is established, a pickup function p similar to that defined by Nielsen (1988) can be defined where $p\delta t$ is the amount of sand per unit area moved in a time interval δt. p is conceptually the same as Q_o in the model. According to Fredsøe and Deigaard (1992 p.213) regression of various data sets indicates that p increases with Shields parameter such that the average thickness of the moving sand is between 0.1 and 0.9 times the thickness of the topmost layer (i.e. $\beta_q = 0.1d$ to $0.9d$). Choosing the sand grain size to be similar to that of the field and Ottawa'95 experiments gave the values of b_q (which equals β_q/L_o) listed in Table 4.1.

Once p and $\vec{L}$ have been established, total bedload transport q_B can be found from

$$q_B = p\vec{L} \tag{4.9}$$

(see, for example, Nielsen 1992, p.115). This can be compared to an empirical bedload transport equation such as the Meyer-Peter and Muller formula (Meyer-Peter and

Muller 1948). In terms of volumetric sand transport, the Meyer-Peter formula is

$$q_B = 8\frac{(u_*^2 - u_{*c}^2)^{3/2}}{(s-1)g}, \tag{4.10}$$

where $(s-1)$ is the relative specific gravity of the sand, and g and d are the acceleration due to gravity and the characteristic sand diameter as defined in the Introduction. u_{*c} is the critical friction velocity for the initiation of movement for the sediment. Typical values for these parameters are $(s-1) \simeq 1.6$ (for sand composed mainly of quartz grains), and $u_{*c} \simeq 1$ cm/s. The values of u_* at which cross-ripples occur ($\theta_s \simeq 0.5$ and $u_* = \sqrt{(s-1)gd\theta_s}$) give $q_B \simeq 0.01 - 0.16\text{cm}^2/\text{s}$. At higher transport rates. the Meyer-Peter formula underestimates the bedload transport, so a coefficient of 12 is suggested by Nielsen (1992) to give a better fit to the data. Equation 4.9 gives values for q_B of 0.01-0.26. These numbers match well with those obtained from Equation 4.10 if a coefficient of 8 is used for low transport conditions, and a coefficient of 12 is used for higher transport rate conditions.

4.1.2 Model Tests.

The model has been developed to study bedforms which generally have a periodic structure. However, the model itself imposes some periodicity due to the finite domain size and the choice of periodic boundary conditions. The effect of the periodic boundary conditions was tested both by increasing grid size, and by rotating the direction of model forcing to a direction not parallel to the grid. Typically the grid could be as small as 90 by 90 points with minimal effects on the bedform pattern. The direction of forcing was changed to a non-parallel of the grid the bedform patterns rotated with the forcing angle. Another effect of finite domain size is the spatial uniformity of the wave forcing shear (and hence $\vec{L}_o$). Typical wave lengths for waves in the nearshore zone are 15-30 meters, much greater than the 1-2 meter length scale of the model domain. It has long been accepted that the approximation of uniform shear stress (discounting local perturbations) over the sand bed test area in wave flume studies which have similar scales is thus valid (see for example Sleath

1984).

The simplified forcing implemented by alternating $\vec{L_{op}}$ and $\vec{L_{on}}$ was checked by running the model with sinusoidally varying $\vec{L_o}$, and with stochastically varying $\vec{L_o}$ and Q as well. As long as there was a difference between the positive and negative peak saltation lengths of the wave there was little difference in the patterns generated by the model. For the stochastic variation case, the asymmetry was maintained by adding a normally distributed random number with an adjustable standard deviation to L_{ox} and L_{oy} at each time step. The main result of adding randomization of 10% to 20% to the hop lengths is that ripples grow more rapidly to their final state. This may be because the domain size is chosen such that it is not an integral multiple of the hop length. The periodic boundary conditions tend to force an integral number of ripples to form within the model domain, so varying the hop length gives the model more freedom to satisfy this condition.

4.2 Computer Simulation Results.

The results from four different model runs are shown in Figures 4.1 through 4.4. Table 4.1 summarizes the parameters used for each of these figures. These images have been oriented to correspond to the sonar images, that is with the top of the page offshore. Darker grey represents topographically higher surfaces. This is in contrast with the sonar images, which have the insonification source at an angle to the bottom surface, hence maximum return signal is from slopes perpendicular to the source. In the sonar images this insonification from an angle results in shadows which complicate the interpretation of the image, so a simple grey scale proportional to height has been chosen to display the model results.

When the model is started with low amplitude random noise, the bedforms grow over a period of several hundred time steps. The first type of bedform to appear is usually linear ripples. As shown in Figure 4.1, for values of $\beta_L < 0.4$, $\beta_c > 0.15$, and $L \simeq 5$ grid steps, linear bifurcating ripples are the final state of the bed. For larger L

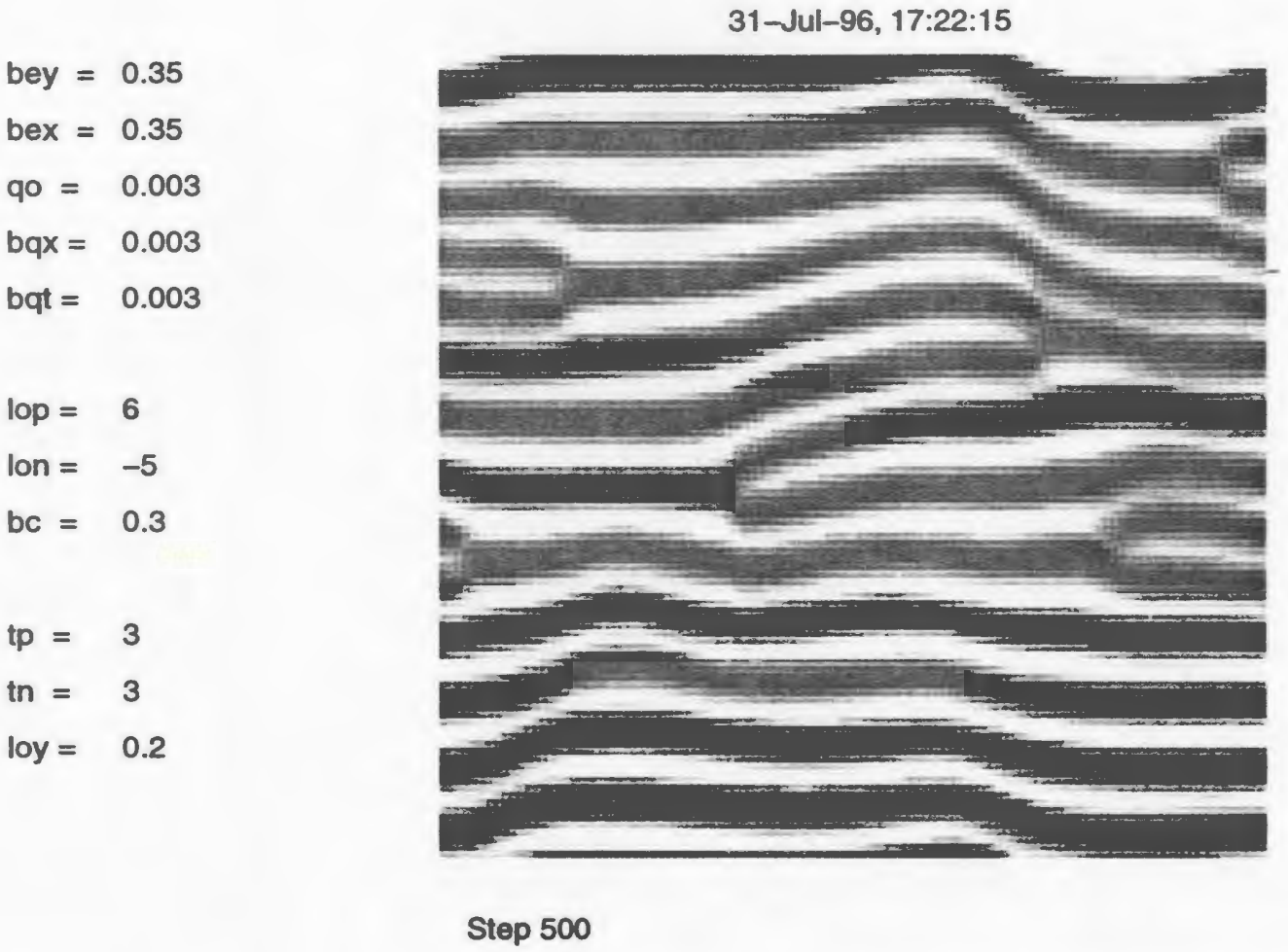

Figure 4.1: Example model results for linear ripples. Note that darker grey represents higher elevation, and that the grey scale has been scaled to the maximum and minimum elevations. The constants used for the run are listed on the left hand side of the figure. Note that an additional constant b_{qt} is listed as this was varied in other trials not discussed here.

bey = 0.35
bex = 0.35
qo = 0.006
bqx = 0.006
bqt = 0.006

lop = 10
lon = –6
bc = 0.33

tp = 2
tn = 4
loy = 0.4

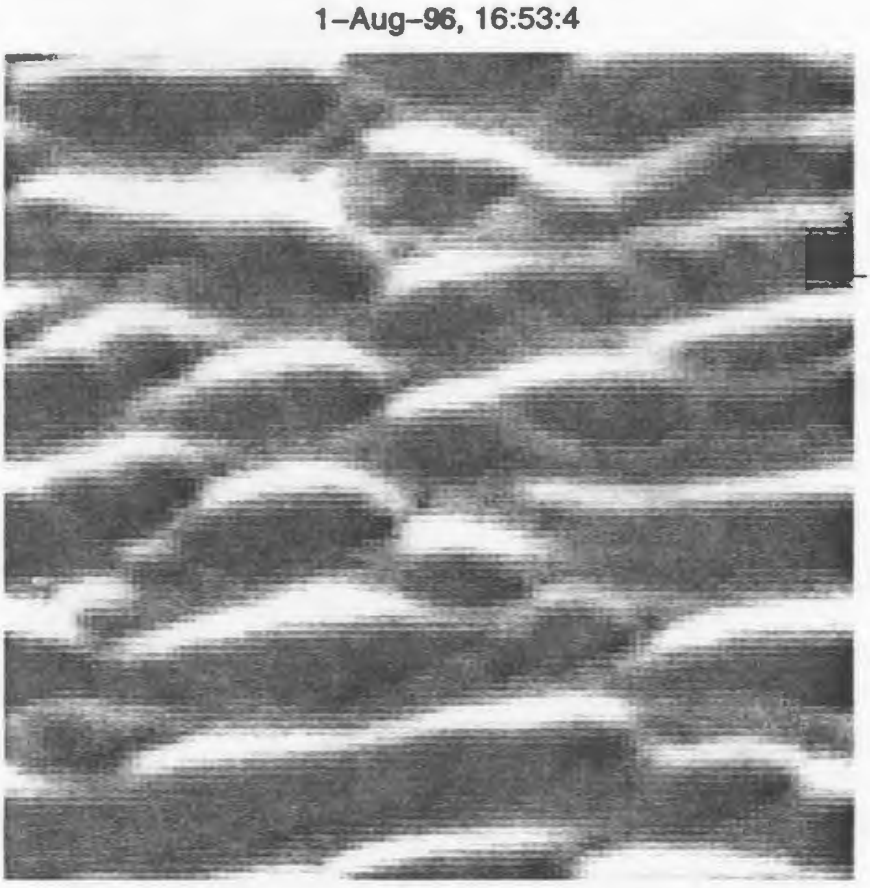

Figure 4.2: Example model results for irregular ripples. Model parameters were similar to the previous figure, but with an increase in saltation velocity and quantity of sand moved q_o.

bey =	0.35
bex =	0.35
qo =	0.005
bqx =	0.005
bqt =	0.005
lop =	14
lon =	–3
bc =	0.34
tp =	2
tn =	5
loy =	0.6

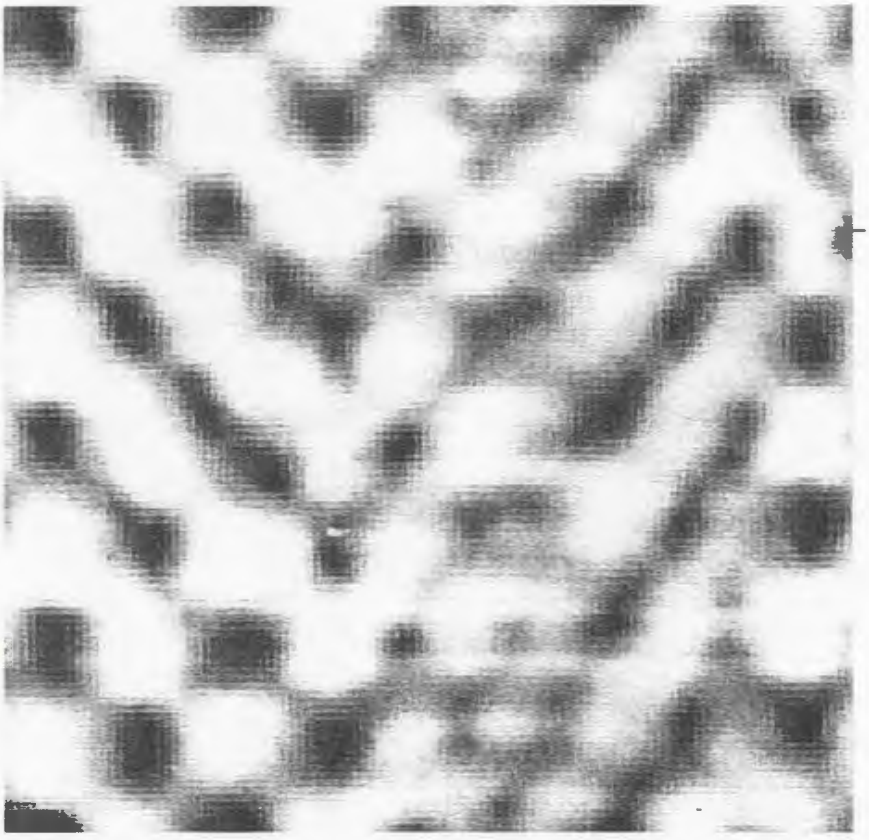

Step 500

Figure 4.3: Example model results for cross-ripples with parameters as listed in the left-hand table. Note the diamond pattern with large ridges with some irregular smaller ripples inside.

bey = 0.48
bex = 0.48
qo = 0.008
bqx = 0.008
bqt = 0.008

lop = 17
lon = –3
bc = 0.45

tp = 2
tn = 5
loy = 0.3

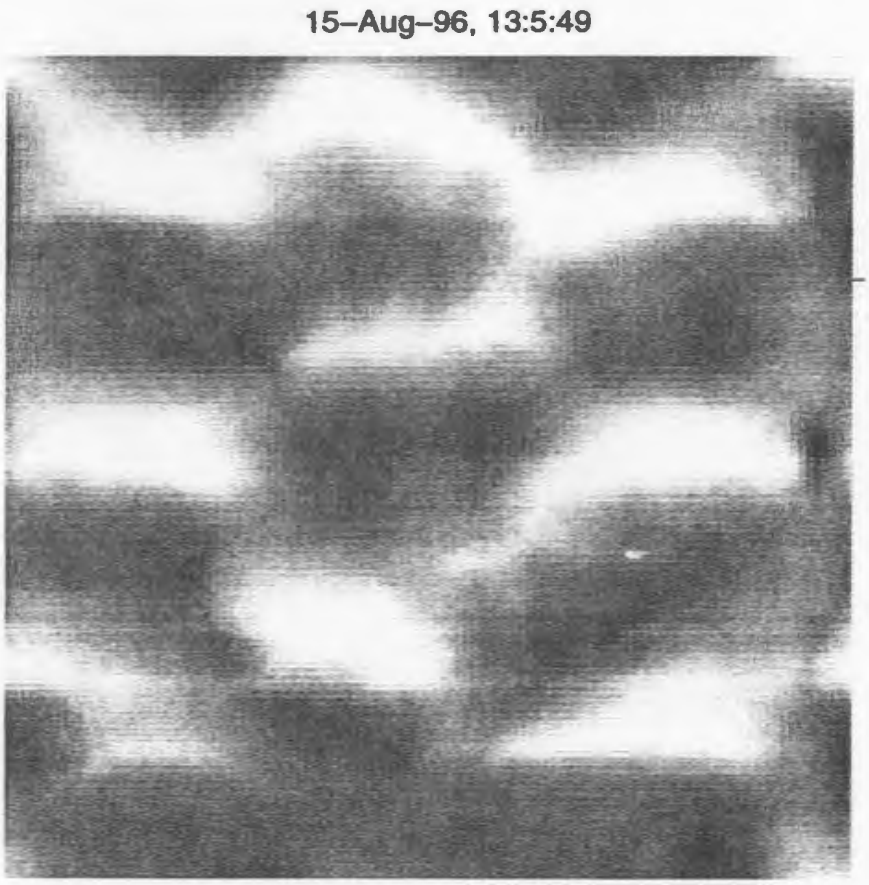

Figure 4.4: Example model results for lunate megaripples. Note the white depressions with mild on-shore curves and irregular location.

Run	1	2	3	4
b_e	0.35	0.35	0.35	0.48
q_o	0.003	0.006	0.005	0.008
b_q	0.003	0.006	0.005	0.008
l_{op}	6	10	14	17
l_{on}	-5	-6	-3	-3
l_{oy}	0.2	0.4	0.6	0.3
β_e	0.3	0.33	0.34	0.45
t_p	3	2	2	2
t_n	3	4	5	5

Table 4.1: Parameters used to produce the images in Figures 4.1through 4.4. Note that coefficients are given in lower case, whereas the arrays of constants used in the equations are written in upper case in the text.

and larger Q_o, irregular ripples form. Increasing the difference between the onshore hop length L_{op} and offshore hop length L_{on} causes the bed to form cross-ripples. The alongshore current L_{oy} was also increased in the model runs presented in Figure 4.3 to give the crossed pattern a clearer dominant ripple set orientation. Note that the parameters displayed on the left side of the images in Figures 4.1 to 4.4 include "bey" and "bex", which refer to the slope effect parameter "b_e" in the "x" and "y" directions, i.e. cross-shore and alongshore. "bex" and "bey" may not be equal under the flow regimes considered in this thesis, but have been kept equal for the model runs presented here.

Further increases in Q_o and β_e under asymmetric forcing cause the bed to continue to transform into a series of curved depressions analogous to lunate megaripples. The amplitude of these ripples scales in general with their horizontal dimensions. Note that for all the model runs presented here the parameter β_q has been scaled to equal q_o (which translates to scaling each constant in the array Q_o), so that sand removal in the lees of ripples is minimized for bedforms with larger slopes. Linear and irregular ripples have heights of 1 to 3 cm for crest-crest spacings of 5 to 12 cm, while cross-ripples have heights of 5 to 10 cm and crest-crest spacings of 10 to 25 cm, and the

lunate depressions have depths of 10 to 20 cm with 30 cm up to the entire model domain (approximately 100 cm) between each of them.

The model produces cross-ripple like features at on-off shore saltation length asymmetries both less extreme and more extreme than those observed in the field and wavetank experiments. For the results in Figure 4.3, an on-shore saltation length of 14 cm, and an off-shore length of 3 cm was used. However, the on-shore period t_p is two seconds, while the off-shore period t_n is five seconds, so that the net sand movement is only slightly on-shore. Note that there does not seem to be a dominant orientation to the larger-scale diagonal bedforms: that is, there are two large scale ripple sets. On the left hand side of the image the large scale ripple set is trending from lower left to upper right while on the left side the larger set trends from upper left to lower right. This is similar to the wavetank observations. The angles of the bedforms with respect to the flow directions and each other vary as a function of the model parameters. These angles have been observed to vary somewhat in the wave tank in the Ottawa'95 experiment and in subsequent field experiments. In the simple form of the model presented here, the smaller scale ripples found in the troughs of the larger diagonal ripples are often poorly formed or absent. This may be due to the lack of any lee sheltering by the larger ripples during higher on-shore velocities, or it may be due to the inability of the model to resolve the smaller ripple scale.

The lunate depressions in Figure 4.4 resemble the lunate megaripples forms. The curvature of the depressions varies as a function of forcing asymmetry, smoothing parameter β_c, and total sediment transport Q_o. The crests of the lunate forms become more curved if β_{Lx} is made greater than β_{Ly}. The ratio of β_{Lx} and β_{Ly} is an additional parameter to vary, as it too should be a function of the near-bed shear stress, and is a subject for further research.

4.2.1 Dominant Ripple Formation Mechanisms.

Several ripple formation mechanisms have been displayed by the model. The principal mechanism involves the systematic increase in the quantity of sand displaced

on the stoss side of each ripple towards the crests of the ripples. This action starts ripple patterns in the cross-shore direction, and these are smoothed together by the creep movement to eventually produce self-reinforcing linear ripples transverse to the flow direction.

With increasing shear stress (or analogously, larger $\vec{L}_o$ and q_o), the slopes transverse to the direction of the flow start to affect the sand movement appreciably. Initially, these transverse slopes produce randomly occurring breaks in the linear ripple pattern which grow into "tuning fork" patterns or more rarely "terminations". It would appear that increases in q_o and β_q are necessary to cause the breaks from linear pattern to become stable. The linear relationships between $\vec{L}$ and Q and the β's did not cause the necessary magnitude of increase, so that further increases in q_o and the β's can be noted in Table 4.1. The mechanisms responsible for the regularization of the pattern in the cross-flow, or y-direction as well as the along-flow, or x-direction are associated with the combination of distance and quantity of sand deflected and the asymmetry associated with the reversing flow. Thus increasing the quantity of sediment deflected in directions transverse to the flow direction leads to three dimensional patterns, and some of these patterns, like cross-ripples, have a regularity in directions oblique to the flow direction.

The creep serves to stabilize the bedforms by smoothing out small scale roughness. Increasing the creep parameter β_c along with asymmetric forcing causes the model to produce lunate forms. Larger β_c is analogous to increasing the bombardment of the bed by suspended sediment which occurs under more energetic flow situations. This tends to wipe out the regular ripple formation mechanism, allowing larger scale bed instabilities to grow. These larger scale features appear to be decoupled from one another by the more intense smoothing and by the increased variability in hop length represented by an increase in β_L. As the emphasis in this thesis is on cross-ripple formation, the formation of lunate bedforms by the model has not been explored fully, and is another topic for further study.

In the simple form presented here, there is no obvious stabilizing influence in the

model to keep the bedforms from growing indefinitely. The stability of the model is discussed further in the next section.

4.2.2 Long-term Ripple Stability.

In the model the ripple fields are only quasi-stable. If the model is perturbed enough, the scale of the ripples will continue to grow until they become linear transverse ripples which approach the domain size of the model. This may be analogous to laboratory ripples, in which the ripples grow to the orbital amplitude even if that amplitude is very large (in some cases over a meter, Arnott and Southard 1990). The model in its current form does not have the temporal variation of lee vortex formation which plays an important role in determining the crest-crest length of orbital ripples (Fredsøe and Deigaard 1992) so that orbital-type ripples may continue to grow in the model beyond the orbital semi-excursion length.

Comprehensive studies of the conditions under which the ripple patterns in the field are stable are underway. The examples chosen from the field and laboratory data for this comparison appeared stable under constant observation for over one hour each. The wave conditions in the field during the decline of the third storm at Burley Beach (Figure 3.18) changed much more slowly than the bed response time. Bed response time was measured in the wave tank as being on the order of ten minutes for the development of stable cross-ripples from an irregular bed after the waves were turned on. This suggests that there is a stability mechanism in the field which is not present in this simplified model or in the wave tunnel results of others. Some efforts to find the stability mechanism are described in following sections.

4.2.3 Secondary Ripple Formation Mechanisms.

There are other mechanisms at work concurrently in the physical environment, not included explicitly in the model, but which may play a role in the formation of cross-ripples as well. Vortices pinned to the crests of the ripples have been observed

by many, and measured by Bagnold in 1946, and are commonly held to be the principle formative mechanism of most naturally occurring wave induced ripples. Their influence on which of the patterns, i.e. straight, brick, or crossripple, the ripples take is less well researched and understood, though it has been postulated that the regularity of the brick pattern may be due to sausage type instabilities in their vortices (Sleath 1984).

The effect of vortices is simulated indirectly by this model. Sediment removal on the lee sides of the ripples can be zero or negative in general. Sediment removal on the lee sides of ripples was prevented from being negative by ensuring that $\beta_q \partial H(x,y)/\partial x > Q_o(x,y)$ for all x and y. In the higher energy flows under consideration here, Bagnold observed that the vortex generation and pinning-release cycle is much more complicated than a simple lee sheltering effect. An interesting feature of this model is that it produces stable cross-ripples even with no lee side sheltering (i.e. $\beta_q = 0$), as shown in Figure 4.5. These cross-ripples appear to be more similar to those observed in the field than those in Figure 4.3, with two different length scales and angles for the larger and smaller ripple sets respectively.

The model in its current form remains rather qualitative, as rigorous measurements of saltation, creep, lee-side sand motion, and the deflection of sand transport and by bedforms are currently lacking. Nonetheless, the model results reproduce many of the features of the field and wave-tank observations.

4.2.4 Model Additions and Tests.

The actual relationships for saltation length $\vec{L}$ and quantity Q as a function of bed slope ∇H are likely more complex than the ones used here. For example, the saltation length ought in general to depends not only on the slope at the initial position of the saltating grains, but also on the difference in elevation between starting and landing positions, and whether the path is obstructed by a bedform peak.

As suggested by Landry and Werner (1994), creep is also more complex than the simple smoothing function described here. Individual grains can roll and hop

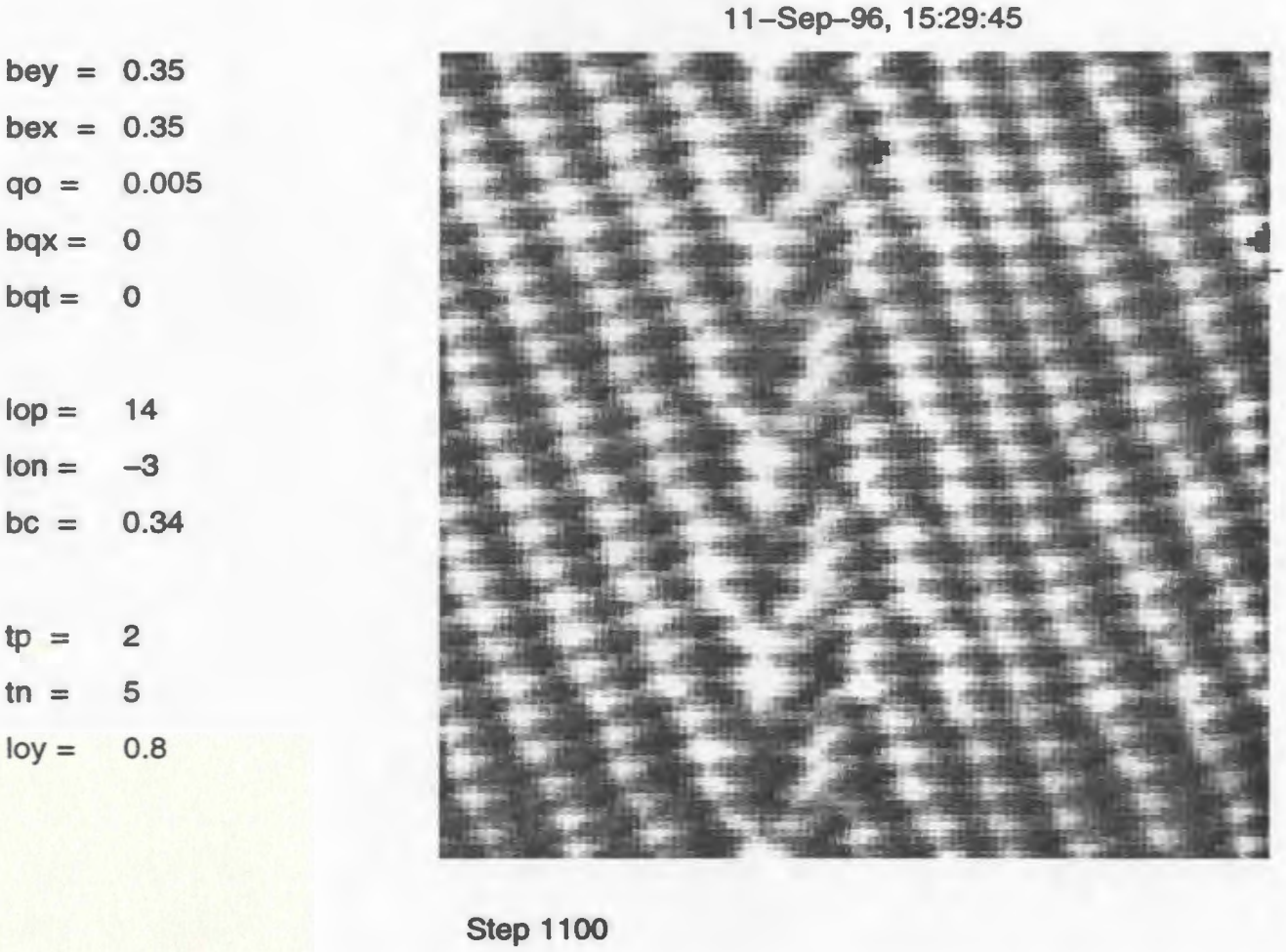

Figure 4.5: Example model results for cross-ripples produced with the same parameters as in Figure 4.3 but with $b_{qx} = b_{qy} = 0$. Note the asymmetrical ripple angles and two scales of ripples, similar to those seen in the field.

along the bed a considerable distance before coming to rest. These grains will be influenced by the shear at the bed so the creep may not be symmetrical. The effect of modelling creep with a simple symmetric smoothing convolution was tested by trying asymmetric forms of the convolution array C. Even with complete smoothing asymmetry (the first column of the array in equation 4.6 made zeros and the third column doubled) no difference was found in the resulting bed-form patterns.

Several additions and modifications to the model were tried to enhance the ripple stability, including angle of repose checking and modulation of the forcing. Of those employed, only applying irregularity to the amplitude of the wave forcing stabilized the cross-ripples. It is interesting to note that limiting the angle of repose had little effect on ripple stability. A routine was written to check for slopes greater than the angle of repose of sand (taken to be approximately 33 degrees for modelling purposes). A fraction of the elevation on the high side grid point exceeding the angle of repose was removed and added to the lower grid point, landslide fashion, and this was repeated iteratively until all slopes had relaxed below the angle of repose.

Another addition to the model was the explicit inclusion of sheltering of the lee-side of each ripple. This was invoked in a simple manner by preventing any deposition on lee slopes steeper than a given small angle. The main effect of this addition was to sharpen the crests of the ripples. The instability was not affected noticably by this addition, though the sharpening of the crests meant that slope limiting kept the ripples from growing as high as they do without the lee sheltering effect. This in turn affects the self-organization of the geometry, since the sand movement is dependent on the bedform slopes and the smaller ripples have smaller slopes. The addition of time dependent lee-side sheltering awaits further software development.

The model was thoroughly tested in the cross-ripple producing parameter range. One of the tests of model validity was to determine the effect of the direction and intensity of longshore currents. It was found that reversing the longshore current reversed the dominant ripple set. In most circumstances, very small ($L_y < 0.1$) longshore saltation rates were sufficient to set up a dominant set. Longshore saltation

rates greater than one or two grid spacings per time step appeared to suppress cross-ripple formation. Many periods of strong longshore current were observed in the field, and no cross-ripples were observed to form under these conditions. The saltation rates for cross-ripple formation and inhibition in the model scale well with the longshore velocities observed in the field for cross-ripple formation and inhibition.

Cross-ripples were formed by the model over a wide range of values for the parameters β. Their influence on the pattern in the bed-forms appears to be more strongly associated with the mechanisms they represent than their values. The parameter which simulates the effect of bed slope deflecting the saltation path, β_L, acting in directions both transverse to and in the direction of the wave motion is sufficient to induce cross-ripples in the model under strong enough flow conditions. The value for β_L in the transverse direction can be made different from the longshore value, as is postulated theoretically (Fredsoe and Deigaard 1992), and cross-ripples still appear. Cross-ripples form in a more regular and stable way if a simulation of the slope effect on quantity of sand moved, β_q is included in the model. The creep parameter β_c is an important source of stabilization in the model. The main effect of β_c on ripple patterns is that it can inhibit the formation of small scale, stable linear ripples in favour of larger forms if set to a sufficiently large value.

Chapter 5

Conclusions.

Using a combination of field observations, wave tank experiments, and model results, the formative mechanisms of sand bedforms under waves in the nearshore have been explored. Considerable variety has been observed in the plan view bedform pattern. At intermediate values of the Shields parameter, the dominant pattern depends on the near-bottom orbital velocities of the waves, and on skewness in these velocities. A most probable formative mechanism for the cross-ripple pattern has been identified. A fundamental instability in the sand bed transverse to the direction of flow leads to self-reinforcing (self-organised) transverse deflection of saltating sand. Under sufficiently energetic conditions, the saltation is deflected along ripple crests at an angle to the flow, while the slower return flow is incapable of reintroducing onshore-offshore symmetry. Laboratory and modelling studies have shown that previously suggested formation mechanisms such as intersecting wave trains are not necessary for the formation of cross-ripples.

Due to the difficulties inherent in observation and measurement during cross-ripple formation, and the inherent complexity of their formative mechanism, direct observation of the movement of the individual sand grains and the forces on them while they organise into cross-ripples has yet to be achieved. Therefore the evidence presented here is somewhat indirect. One of the intriguing aspects of the study of sand ripples is the fact that they occur in a variety of forcing situations in air and under

water. The central mechanisms of the ripple formation and stability are recognised to be different in each regime, yet the ripples are remarkably similar in character, pattern, and even size. This observation must temper any conclusions to be drawn from such a simple model while supporting the hypothesis that self-organization plays a role.

All efforts to include in the model a more complete description of the physical mechanisms of ripple formation have not affected the robust nature of the model's ability to produce cross-ripples. The model also correctly generates the other ripple patterns observed in the field, and with the correct order of pattern observed as a function of increasing wave energy. Thus the model is highly suggestive, yet the lack of long term stability of the model ripples indicates that the model is not complete. Work is in progress to address this and to make measurements to establish physical values for the parameters used in the model.

Bibliography

Allen, J.R.L., *Current Ripples, Their Relation to Patterns of Water and Sediment Motion*, North-Holland Publishing Co., Amsterdam 1968.

Allen, J.R.L., *Sedimentary Structures; Their Character and Physical Basis*, Vol.1 and 2, Elsevier, Amsterdam 1982.

Amos, C.L., A.J. Bowen, D.A. Huntley, and C.F.M. Lewis, 1988. Ripple generation under the combined influences of waves and currents on the Canadian continental shelf. *Continental Shelf Res.* **8** No. 10, pp. 1129-1153.

Arnott, R.W. and J.B. Southard, 1990. Exploratory flow-duct experiments on combined-flow bed configurations, and some implications for interpreting storm-event stratification, *J. Sedimentary Pet.* **60**, No.2 , pp. 211-219.

Aubrey, D.G., J.H. Trowbridge, and W.D. Spencer. 1984. Dynamic response of spherical electromagnetic current meters. *IEEE Oceans '84 Proceedings* Vol. 1 pp. 242-248.

Bagnold R.A., 1946. Motion of Waves in Shallow Water. Interaction of Waves and Sand Bottoms. *Royal Soc. London Proc.* Ser. A **187**, pp.1-18.

Battjes, J.A., 1988. Surf-Zone Dynamics, *Ann. Rev. Fluid Mech.* **20** 257-293.

Beach,R.A., and R.W. Sternberg, 1988. Suspended sediment transport in the surf zone: response to cross-shore infragravity motion. *Marine Geol.* **80**, pp 61-79.

Blondeaux, P., 1990. Sand Ripples under Sea Waves, Part 1. Ripple Formation. *J. Fluid Mech.* **218**, pp. 1-17.

Boyd, R., D.L. Forbes, and D.E. Heffler, 1988. Time-sequence observations of wave-formed sand ripples on an ocean shoreface. *Sedimentology* **35**, pp. 449-464.

Briggs, K.B. 1989. Microtopographical roughness of shallow-water Continental shelves. *IEEE J. Ocean. Eng.* **14**, No. 4, pp.360-367.

Clifton, H.E., R.E. Hunter, and R.L. Phillips. 1971. Depositional structures and processes in the non-barred high-energy nearshore. *J. Sed. Petrology* **41**, pp. 651-670.

Clifton, H.E., 1976. Wave-Formed Sedimentary Structures-A Conceptual Model, In *Beach and Nearshore Sedimentation*, R.A. Davis, Jr. and R.L. Ethington, eds. SEPM, Special Pub. No. 24, pp. 126-148.

Clifton, H.E., and J.R. Dingler, 1984. Wave-formed structures and paleoenvironmental reconstruction. *Marine Geol.* **60**, pp. 165-198.

Davidson-Arnott R.G.D., and B. Greenwood, 1974. Facies Relationships on a Barred Coast, Kouchibouguac Bay, New Brunswick, Canada., in Davis, R.A., Jr., and Ethington, R.L., eds., *Beach and Nearshore Sedimentation: Soc. Econ. Paleontologists Mineralogists Spec. Pub. No. 24*, pp. 149-168.

Dingler, J.R., and H.E. Clifton, 1984. Tidal-cycle changes in oscillation ripples on the inner part of an estuarine sand flat. *Marine Geol.* **60**, pp. 219-233.

Dingler, J.R. and D.L. Inman, 1976. Wave-formed ripples in nearshore sands, *Proc. 15th Conf. Coastal Eng.*, pp. 2109-2126.

Dostoevsky, F. 1874. *The Brothers Karamazov.* Penguin Books Ltd. Harmondsworth, U.K. 1974.

Elgar, S., and R.T. Guza, 1985. Observations of bispectra of shoaling surface gravity waves. *J. Fluid Mech.* **161**, pp. 425-448.

Fernandez Luque, R., and R. van Beek, 1976. Erosion and transport of bed-load sediment,*J. Hydraulic Res.*, **14**(2), pp. 127-144.

Fredsøe, J. and R. Deigaard, 1992. *Mechanics of Coastal Sediment Transport*, World Scientific Publishing Co. Singapore, 1992.

Gilly J.E., Kottwitz, E.R., and Wieman, G.A., 1992. Darcy-Weisbach roughness coefficients for gravel and cobble surfaces. *J. Irr. and Drainage Eng.* **118** No.1, pp. 104-112.

Grant, W.D., and O.S. Madsen, 1979. Combined wave and current interaction with a rough bottom. *J. Geophys. Res.* **84** No. C4. pp. 1797-1808.

Grant, J. and G. Gust, 1987. Prediction of coastal sediment stability from photopigment content of mats of purple sulphur bacteria. *Nature* **330**, No. 6145, pp. 244-246.

Guza, R.T., and E.B. Thornton, 1980. Local and shoaled comparisons of sea surface elevations, pressures and velocities. *J. Geophys. Res.* **85**, pp. 1524-1540.

Guza, R.T., and E.B. Thornton, 1985. Velocity moments in the nearshore. *J. Waterway, Port, Coastal and Ocean Eng.*, **111**, No. 2, pp. 235-256.

Hasselmann, K., W. Munk, and G. MacDonald, Bispectra of Ocean Waves. In *Time Series Analysis* (ed. M. Rosenblatt), pp.125-139, Wiley Press, New York. 1963.

Hay, A.E., Huang L., E.B. Colbourne, J. Sheng, and A.J. Bowen, 1988. A High Speed Multi-Channel Data Acquisition System for Remote Acoustic Sediment Transport Studies, in *Oceans '88 Proceedings* IEEE, Baltimore Vol.2, pp. 413-418.

Hay, A.E., and D.J. Wilson, 1994. Rotary sidescan images of nearshore bedform evolution during a storm. *Marine Geol.* **119**, pp. 57-65.

Hazen, D.G., D.A. Huntley and A.J. Bowen, 1987. UDATS: A System for Measuring nearshore Processes, *Proc. Oceans '87*, pp. 993-997, 1987.

Horikawa, K., *Nearshore Dynamics and Coastal Processes*, K. Horikawa ed., University of Tokyo Press, Tokyo, 1988.

Hwung, H.H. and C. Lin, 1990. The mass transport of waves propagating on a sloping bottom. *Proc. 23rd Coastal Eng. Conf.*, pp. 544-556.

Hunt, A.R., 1882. On the foramtion of ripplemark. *Proc. Roy. Soc.* **34**, pp. 1-18.

Hunter, R.E., H.E. Clifton, and R.L. Phillips, 1979. Depositional Processes, Sedimentary Structures, and Predicted Vertical Sequences in Barred Nearshore Systems, Southern Oregon Coast., *J. Sedimentary Pet.* Vol.49, No.3 pp. 711-726.

Inman, D.L., 1957. Wave Generated Bedforms in Nearshore Sands. *Tech. Memo 100*, U.S. Army Corps Eng., Beach Erosion Board, 41p.

Jonsson, I.G., 1966. Wave Boundary layers and friction factors. *Proc. 10th Coastal Eng. Conf.*, Vol. 1, pp. 127-145.

Kawata, Y., T. Shirai, and Y. Tsuchiya, 1990. Field observations on sand ripples under rough sea state. *Proc. 23rd Conf. Coastal Eng.*, pp. 2164-2174.

Kennedy, J.F., 1963. The mechanics of dunes and antidunes in erodible-bed channels. *J. Fluid Mech.* **16**, pp. 521-544.

Kennedy, J.F., 1969. The formation of sediment ripples, dunes, and antidunes. *Ann. Rev. Fluid Mech.* **1**, pp. 147-168.

Landry, W, and B.T. Werner, 1994. Computer simulations of self-orgainized wind ripple patterns., *Physica* **D77** pp. 238-260.

Lee, D., and H. Wang, 1984. Measurement of surface waves from subsurface gage. *Proc. 21st Conf. Coastal Eng.*, pp. 271-286.

Li, M.Z., and Amos, C.L., 1995. Ripple geometry and bed roughness under combined waves and currents on the Scotian Shelf. *Proc. 1995 Canadian Coastal Conf.* Vol.2,

pp. 511-526.

Lofquist, K.E.B., 1978. Sand Ripple Growth in an Oscillatory-Flow Water Tunnel, Tech. Paper No. 78-5 Coastal Eng. Res. Center, U.S. Army Corps Eng.

Longuet-Higgins, M.S., 1957. The statistical analysis of a random, moving surface, *Phil. Trans. Roy. Soc. London* Ser. A, **249**, pp. 321-387.

Longuet-Higgins, M.S. and R.W. Stewart, 1964. Radiation stresses in water waves; a physical discussion, with applications. *Deep Sea Res.* **11**, pp. 529-562.

McLean, S.R., 1990. The stability of ripples and dunes. *Earth Sci. Rev.* **29**, pp. 131-144.

McLean, S.R., and Smith, J.D., 1986. A Model for Flow over two-dimensional bed forms., *J. Hydraul. Eng.* ASCE, 112: pp 300-317.

Miller, M.C., and P.D. Komar, 1980a. Oscillation sand ripples generatied by laboratory apparatus. *J. Sed. Petro.* **50**, No. 1, pp. 173-182.

Miller, M.C., and P.D. Komar, 1980b. A field investigation of the relationship between oscillation ripple spacing and the near-bottom water orbital motions. *J. Sed. Petro.* **50**, No. 1, pp. 183-191.

Mogridge, G.R., and J.W. Kamphuis, 1972. Experiments on bed form generation by wave action. *Proc 13th Conf. Coastal Eng.*, pp. 1123-1142.

Nielsen, P., 1981. Dynamics and Geometry of Wave-Generated Ripples. *J. Geophys. Res.* **86**, pp. 6467-6472.

Nielsen, P., 1988. Three simple models of wave sediment transport. *Coastal Engineering* **12**, pp. 43-62.

Nielsen, P., 1992. *Coastal Bottom Boundary Layers and Sediment Transport*, World Scientific Publishing Co. Singapore.

Nishimori, H., and N. Ouchi, 1993. Formation of Ripple Patterns and Dunes by Wind-Blown Sand, *Phys. Rev. Lett.* **71** No. 1, pp. 197-200.

Pettijohn, F.J, P.E. Potter, and R.Siever, 1987. *Sand and Sandstone, Second Edition*, Springer-Verlag, New York.

Raudkivi, A.J., 1990 *Loose Boundary Hydraulics*, Pergamon Press, Oxford.

Ribberink, J.S., and A. Al-Salem, 1990. Bedforms, sediment concentrations and

sediment transport in simulated wave conditions. *Proc. 23rd Conf. Coastal Eng.*, pp. 2318-2331.

Richards, K.J. 1980. The formation of ripples and dunes on an erodible bed. *J. Fluid Mech.* **99**, pp. 597-618.

Sato, S. and K. Horikawa, 1988. Sand ripple geometry and sand transport mechanism due to irregular oscillatory flows. *Proc. 22nd Conf. Coastal Eng.*, pp. 1748-1762.

Shields, A., 1936. Anwendiung der Ahnlichkeitsmechanik und der Turbulenzforschung auf die Geschiebebewegung: Mitteilungen der Preuss. Versuchanst. für Wassserbau und Schiffbau, Berlin, v. 26, 26p., translated by W.P. Ott and J.C. van Uchelen, U.S. Dept. Agriculture, Soil conservation Service Coop. Lab., Calif. Inst. Tech.

Sleath J.F.A., 1984. *Sea Bed Mechanics*, John Wiley and Sons, Inc. New York.

Sleath J.F.A., 1987, Turbulent oscillatory flow over sand grain roughened beds, *J. Fluid Mech.* **182**, pp. 369-409.

Sleath, J.F.A., 1990. Seabed boundary layers, in *The Sea, Volume 9.*, Pergamon Press, London.

Sleath, J.F.A., 1991. Velocities and shear stresses in wave-current flows. *J. Geophys. Res.* **96** No. C8, pp. 15237-15244.

Smith, J.D., 1970. Stability of sand beds under waves. *J. Geophys Res.*, **75**. pp 5928-5938.

Southard, J.B., Lambie, J.M., Federico, D.C., Pile, H.T., and Weidman, C.R., 1990. Experiments on bed configurations in fine sands under bidirectional purely oscillartory flow, and the origin of hummocky cross-stratification. *J. Sed. Petro.*, **60**, No. 1, pp. 1-17.

Swart, D.H., 1974. Offshore sediment transport and equilibriem beach profiles. *Delft Hydr. Lab Pub. No. 131.*

Vittori G., and P. Blondeaux, 1990. Sand Ripples under Sea Waves, Part 2. Finite-Amplitude Development. *J. Fluid Mech.* Vol 218 pp. 19-39.

Vittori G., and P. Blondeaux, 1992. Sand Ripples under Sea Waves, Part 3. Brick-pattern Ripple Formation. *J. Fluid Mech.* Vol 239 pp. 23-45.

Wiberg, P.L., and J.D. Smith, 1985. A theoretical model for saltating grains in water. *J. Geophys. Res.* **90** No. C4, pp 7341-7354.

Wiberg, P.L., and C.L. Harris, 1994. Ripple geometry in wave-dominated environments. *J. Geophys. Res.* **99** No. C1, pp. 775-789.

Willis, D.H., M.H. Davies, and G.R. Mogridge, 1993. Laboratory observations of bedforms under directional irregular waves. *Can. J. Civ. Eng* **20**, pp. 550-563.

Wilson, D.J., and A.E. Hay, 1995. High resolution sidescan sonar observations of small scale sand bedforms under waves: a comparison of field and laboratory measurements. *Proc. 1995 Canadian Coastal Conf.* Canadian Coastal Science and Engineering Association, Ottawa.

Yalin, M.S., and R.C.H. Russell, 1962. Similarity in sediment transport due to waves. *Proc. Eighth Coastal Eng. Conf.*, pp. 151-167.

Yalin, M.S., 1977. *Mechanics of Sediment Transport*, Pergamon Press, Oxford 1977.

Yalin, M.S., and E. Karahan, 1978. On the Geometry of Ripples Due to waves. *Proc. 16th Conf. Coastal Eng.* pp. 1776-1790.

Appendix A

Further Analysis of Results.

In this thesis data analysis consisted of the interpretation of the sonar ripple images, and the correlation of cross-ripple formation times with the wave parameters relevant to ripple formation, with an emphasis on narrowing down the wave properties responsible for cross-ripple formation. The first section of this appendix describes some processing of the sonar images which was done to aid in their interpretation. The second section of the appendix describes some of the wave and current analyses which were done to determine whether changes in wave directionality played a role in cross-ripple formation. These analyses were not included in the body of the thesis because they were inconclusive, and the wave tank results were strong evidence that wave directionality was not an important factor. The third section includes discussions of the factors influencing the accuracy of the wave and current measurements.

A.1 Image Analysis.

Analysis of sonar images from Burley Beach and Ottawa follow similar paths, though the level of external information available in the Ottawa experiment means that the image analysis of the Ottawa images can be used as verification of the analysis techniques. There is a large amount of information in the digitised images, and there

are a large number of images from the two experiments. However, when a storm by storm study of bedforms was undertaken, the video-taped data were necessary to fill in bedform information during rapid changes in the bed. For the purposes of identifying and classifying the bedforms present at any given time, much of the image information is redundant.

A.1.1 Geometrical Corrections and Filtering.

As mentioned in the results section, the sonar images of bottom bedforms were slant-range corrected and dejittered before classification. Considerable care was taken to remove image distortions due to the acoustics. The first order geometrical correction was slant-range correction assuming the bed under the sonar was flat on the scale of 10 meters and the axis of rotation of the transducer was normal to this flat bed (the range rings at every two metres have been adjusted to reflect the distance along the bottom from the axis of rotation). Tests on the validity of these assumptions have been made using the variation in beam intensity as a function of angle from the head (Figure 2.1). As discussed in the the Experiments section, variations in beam intensity show up as bright and dark rings in the image on the scale of a half to one meter, of 1 to 3 meters radius. Large scale slope or undulations in the bed show up as deviations of these rings from circular into ovals. The geometrical lengthening of the long axis of a ring of angle β in ordinal (as measured above horizontal) and an overall bed slope of α can be shown to be

$$\frac{A}{C} = \frac{1}{2}\left(\frac{\cos(\beta)}{\cos(\alpha+\beta)} + \frac{\cos(\beta)}{\cos(\alpha-\beta)}\right). \tag{A.1}$$

The effect is small for the β and α encountered at Burley Beach. Thus preliminary filtering consisted of removal of jitter in the trigger only. The digitising for each ping was started approximately 10 to 13 samples (100 to 130 microseconds) before the transducer actually generated the sound. This variable gap in data at the beginning of each ping record was removed using the falling edge of the sound pulse as the

starting point of the data.

A.1.2 Effects of Suspended Sediment on Images.

Several effects due to suspended sediment were observed in the images. During periods of cross-ripple formation the principal effect was intermittent obscuring of view. Another effect was loss of signal at greater range, due to attenuation. Thus although the sonar range was five meters, visibility was less than three meters during the most energetic periods of the storms. During these periods flat bed generally prevailed. Initially it was not clear whether the bed was flat, or merely obscured by suspended sediment. However, the frame posts and their shadows were always visible, and the bottom reflection signal was quite strong near the sonar head, indicating that we were still seeing the bottom. At somewhat lower energies suspension "events" lasting on the order of seconds and extending over a range of 1 to 3 meters blurred portions of some of the images. The effects of intermittent suspension events can be ameliorated by averaging several successive images together. The time scale of bed form motion was typically on the order of several centimeters per hour (see, for example Lofquist 1979) and the successive bottom images were obtained approximately one minute apart, so that blurring on the order of millimeters can be expected due to averaging data files 1 to 5 minutes apart. In this thesis, the images have been used mainly for classification of bedform type, so averaging has not been used.

A.1.3 Ripple Height Information.

In the existent literature, the cross-sectional profiles of bedforms provide an important means of classifying the bedform. This information is not readily available from the rotary sidescan data. Photographs from the Ottawa experiments through the side glass indicate that the cross-ripples form to nearly the angle of repose in both inter-leaved sets. This information may well be adequate for the classification of the bedforms described in this thesis.

One piece of information possibly available is whether the bedforms are symmetrical in the on-off shore direction. This is of particular relevance to the mechanism of formation of cross-ripples, for if caused by wave velocity asymmetry, the bedforms would be expected to have an asymmetrical shape. If the assumption can be made that the bedforms are uniform about the sonar head (an assumption not always correct, as seen in some Burley Beach files), then differences in appearance and intensity of backscatter from the ripples off-shore of the sonar head and ripples on-shore is related to the relative steepness of the off-shore facing and on-shore facing sides of the ripple crests. This asymmetry was quite apparent in both sonar and direct observations in the Ottawa'93 experiment in runs 19 (0.5 meter waves with 5 second period) and run 22 (0.55 meter waves with 3.5 second period). These runs produced low amplitude linear ripples and megaripples. The runs which produced cross-ripples did not show obvious asymmetry.

A.2 Wave and Current Analysis.

A.2.1 Directional Spectra

Directional spectra were calculated for the Burley Beach experiment using the extended maximum likelihood method as described by Horikawa 1988. For a three component array consisting of a single two component current meter and a pressure gauge, the directional power spectrum $S(f,\alpha)$ can be estimated from the power cross-spectra by

$$S(f,\alpha) = K_o \left[\begin{array}{l} M_0 M_2(\gamma^2 \cos^2 \tilde{\alpha} + \sin^2 \tilde{\alpha}) - \\ M_1^2 \sin^2 \alpha - 2M_1 M_2(\gamma^2 \cos \tilde{\alpha_m} \cos \tilde{\alpha} + \sin \tilde{\alpha_m} \sin \tilde{\alpha}) + M_2^2 \gamma^2 \end{array} \right]^{-1} \quad \text{(A.2)}$$

where

$$\tilde{\alpha} = \alpha - \alpha_p \quad \text{(A.3)}$$

$$\tilde{\alpha}_m = \alpha_m - \alpha_p \tag{A.4}$$

$$\alpha_m = \tan^{-1}(\Phi_{zv}/\Phi_{zu}) \tag{A.5}$$

$$\alpha_p = \frac{1}{2}\tan^{-1}\left(\frac{2\Phi_{uv}}{\Phi_{uu} - \Phi_{vv}}\right) \tag{A.6}$$

$$M_0 = \Phi_{zz}(f) \tag{A.7}$$

$$M_1 = \sqrt{\Phi_{zu}^2 + \Phi_{zv}^2}/H_u \tag{A.8}$$

$$M_2 = \frac{\Phi_{uu} + \Phi_{vv}}{2H_u^2} + \sqrt{\left(\frac{\Phi_{uu} - \Phi_{vv}}{2H_u^2}\right)^2 + \frac{\Phi_{uv}^2}{H_u^2}} \tag{A.9}$$

where the Φ_{ij} are the cross-spectral components calculated by multiplying the Fourier components term by term of the surface height z, cross-shore velocity u, and long-shore velocity v records. H_u are factors which convert velocities to their proportional surface wave heights. These factors can be calculated by shallow water theory, but Horikawa suggests a self-calibration scheme to avoid calibration mismatches which might give anomalous results: that is,

$$H_u = \sqrt{[\Phi_{zu} + \Phi_{zv}]/\Phi_{zz}}. \tag{A.10}$$

The factor γ in equation A.2 is the Longuet-Higgins Directionality coefficient, as described in the next section. The angles α_m and α_p are the mean and principal angles of incidence of the waves.

Longuet-Higgins Directionality

A simpler approach to measuring the effect of the directions of incident waves is Longuet-Higgins'(1957) wave directionality coefficient, γ, a measure of the spread in the angle of incidence obtained by taking the ratio of the variances of the cross-shore and long-shore velocity signals in the incident wave band. The directionality coefficient γ is defined as

$$\gamma = \left[\frac{(\Phi_{uu} + \Phi_{vv}) - \sqrt{(\Phi_{uu} - \Phi_{vv})^2 + 4\Phi_{uv}^2}}{(\Phi_{uu} + \Phi_{vv}) + \sqrt{(\Phi_{uu} - \Phi_{vv})^2 + 4\Phi_{uv}^2}}\right]^{1/2}. \tag{A.11}$$

A.2.2 Directional Spectral Analysis.

Directional spectral analysis was performed using MATLAB on wave records from Burley Beach. Directional spectra could not be calculated on the wave tank data as the current meters were oriented to measure horizontal and vertical velocity.
The directional spectra were calculated using the extended maximum likelihood method as described by Horikawa 1988 using sample lengths of 1024 samples (approximately four minutes) from the 55 minute record with no overlap. This gave 14 completely statistically independent realizations of the waves. The 1024 sample segments were Hanning windowed, then cross-power spectra were calculated. The angle resolution was divided into 60 bins, and spectra for each angle were calculated. Then the 14 directional spectra were averaged together to obtain a statistically meaningful result. an example of which is shown in Figure A.1.
This example is typical of the directional spectra for the declining of the storms at Burley Beach. The dominant wave was the 5.5 second period storm swell approaching the beach from about 20 degrees North of the beach normal. There also appears to be some energy at 4.5 second period, approaching the beach from 15 degrees south of beach normal. The initial parts of the storm display a broader energy range in both frequency and direction, but the dominant peak is almost always close to shore-normal. In most of the power spectra, the second harmonic of the main incident wave band is visible above the noise, but is typically an order of magnitude smaller than the main peak, so does not show up in the contouring in Figure A.1.

A.3 Wave Measurement Accuracy.

As with the sonar systems employed, there are limitations to the accuracy and applicability of the wave data from field and laboratory measurements. These limitations become more important as higher order wave moments, such as skewness and asymmetry, and low frequency effects, such as currents, wave tank seiches, and

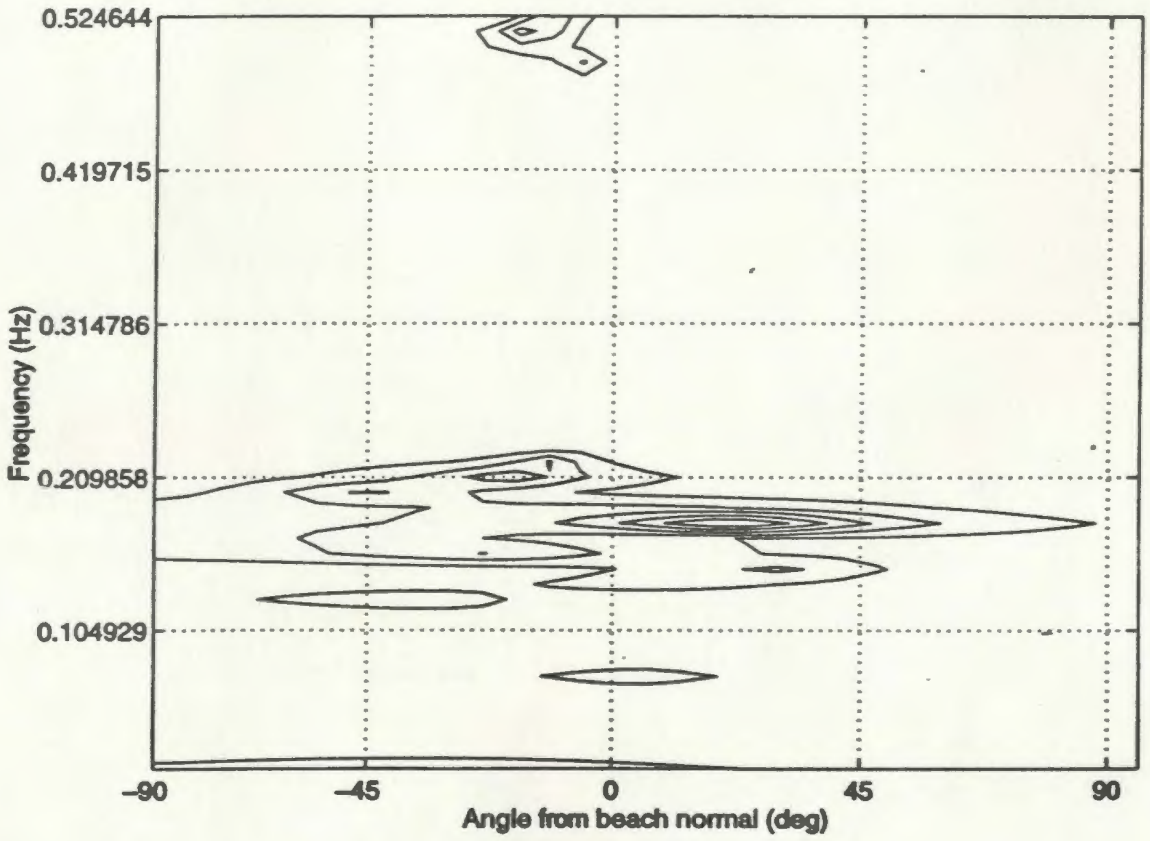

Figure A.1: Contour plot of the directional Spectrum from the Burley Beach wave record. The data used were from Marsh-McBirney current meter cm849, and pressure sensor p500 from the time period of Oct. 25, 1992 from 20:00 to 20:55. This is part of the period in which cross-ripples dominated the bedforms at the end of the third storm.

infra-gravity waves are considered.

As mentioned in the Experiment section, in the Burley Beach and Ottawa 1993 experiments, wave velocities were measured with Marsh McBirney model 512 (5 centimeter diameter heads) current meters and either a pressure transducer (at Burley Beach) or wave staffs (in the NRC). The accuracy and precision of these current meters has been extensively studied, see for example Aubrey, Trowbridge and Spenser (1984). In general, a calibrated Marsh-McBirney has linearity of 2.0 % over the range of velocities from 0.01 to 3 meters per second, as claimed by the manufacturer. There is a high frequency cut off in the electronics at 1.6 Hz for the -3 dB point. There is a systematic increase in the sensitivity of the sensor in oscillatory flows, and a systematic decrease in sensitivity of in combined steady-oscillatory flows of up to 10 % due to complicated wake effects. Thus for this study, since a single calibration factor (plus offset) was used for all frequencies, the uncertainty has been roughly estimated to be 5 %, as in Guza and Thornton (1980). The uncertainty for skewness would thus be approximately three times this uncertainty (as discussed in Aubrey et al.). Thus the skewness and asymmetry from the pressure sensor, which has an estimated uncertainty of approximately 2%, were used in the analysis of the Burley Beach data, and the wave staffs, which have uncertainties of approximately 1%, were used for skewness and asymmetry in the Ottawa experiments.

At the Ottawa'95 experiments the most reliable velocity measurements were obtained from an Sontek Acoustic Doppler velocimeter. As the instrument samples a location approximately ten centimeters away from the instrument, there should be no sensor wake effects.

Wave height measurements from the pressure sensor in the field were also prone to frequency dependent effects, as the water depth acts as a low pass filter. These effects have been discussed in Lee and Wang (1984). For the one meter nominal depth of the pressure sensor at Burley Beach, the cut-off frequency was on the order of 2 Hz, which is also the cut-off of the preliminary data filter. The accuracy of the pressure sensor

was better than the precision of the digitising system, which gave a resolution of approximately 0.12 kPa, or approximately one centimeter resolution in wave height. In the Ottawa experiments calibrated wave staffs and relatively clean fresh water were used, so that uncertainties in wave heights were of the order of the meniscus (0.003 meters) and the accuracy was even greater.

Thus the pressure sensor and wave staffs were used to calculate the higher moments such as skewness and asymmetry used in this analysis. The relationships between skewness derived from the Marsh-McBirney current meter CM849 S_v and skewness from the pressure sensor S_p are shown in Figure A.2. After filtering for outliers. linear regression gives a relationship of

$$S_p = 0.94 S_v + 0.195. \tag{A.12}$$

Much of the scatter in the data occurs at low wave heights, where signal noise has a much larger effect. Velocity skewnesses and asymmetries may also be contaminated by cross-shore currents. As shown in Figure A.3. there is more scatter in the asymmetry data.

A.3.1 Calibration.

Calibrations for the current meters used at Burley Beach and Ottawa 1993 were done in a unidirectional flume at the National Research Council in Ottawa and by the Dalhousie group at the Centre for Inland Waters, National Research Council, Burlington, Ontario (unpublished). Wave staff calibrations were done using still water level readings in-situ before and after the Ottawa experiments.

The Acoustic Doppler velocimeter used in the Ottawa'95 experiment relies on the speed of sound in water to measure velocities, so that as long as the scatterers in the water are passive drifters (a reasonable assumption in most conditions) the calibration is very accurate. Gain calibration was performed in the Memorial University of Newfoundland Tow tank. Velocities measured with the the Doppler system were

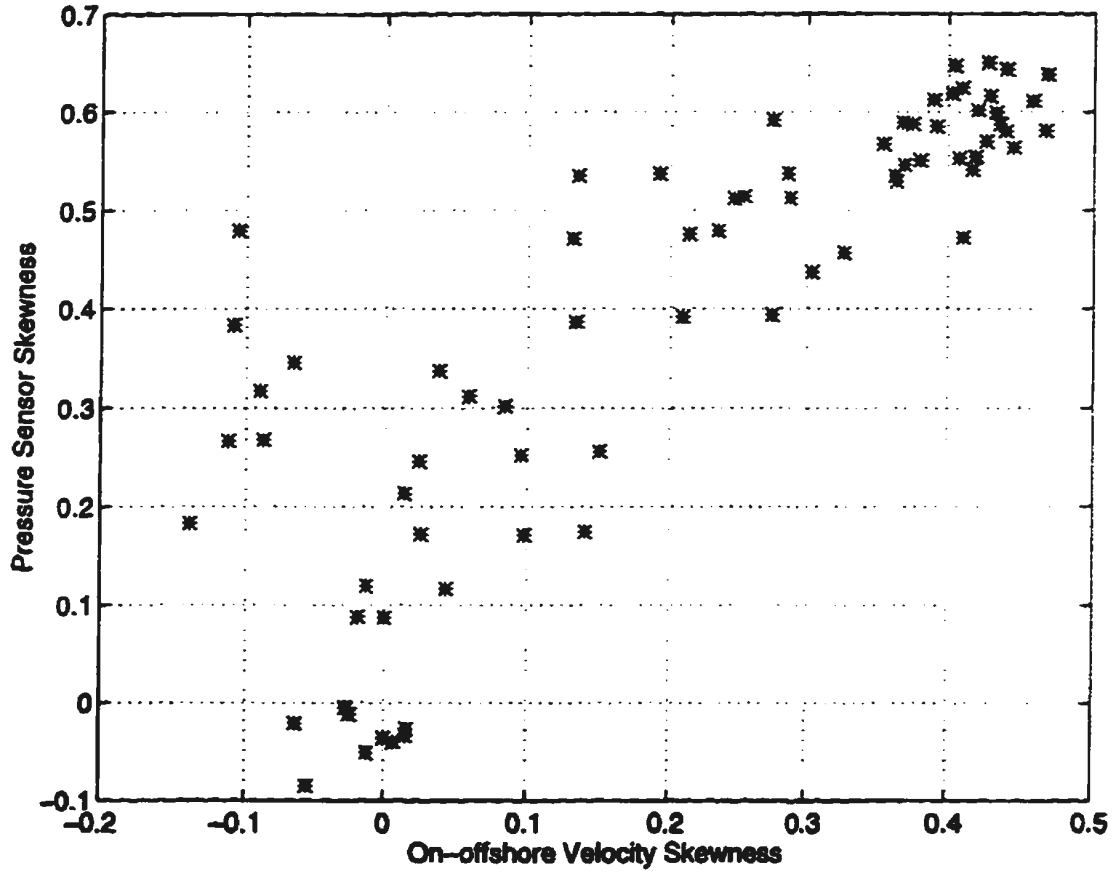

Figure A.2: Skewness calculated from on-offshore velocity compared to skewness obtained from a co-located pressure sensor. The data are from the Burley Beach 1992 experiment.

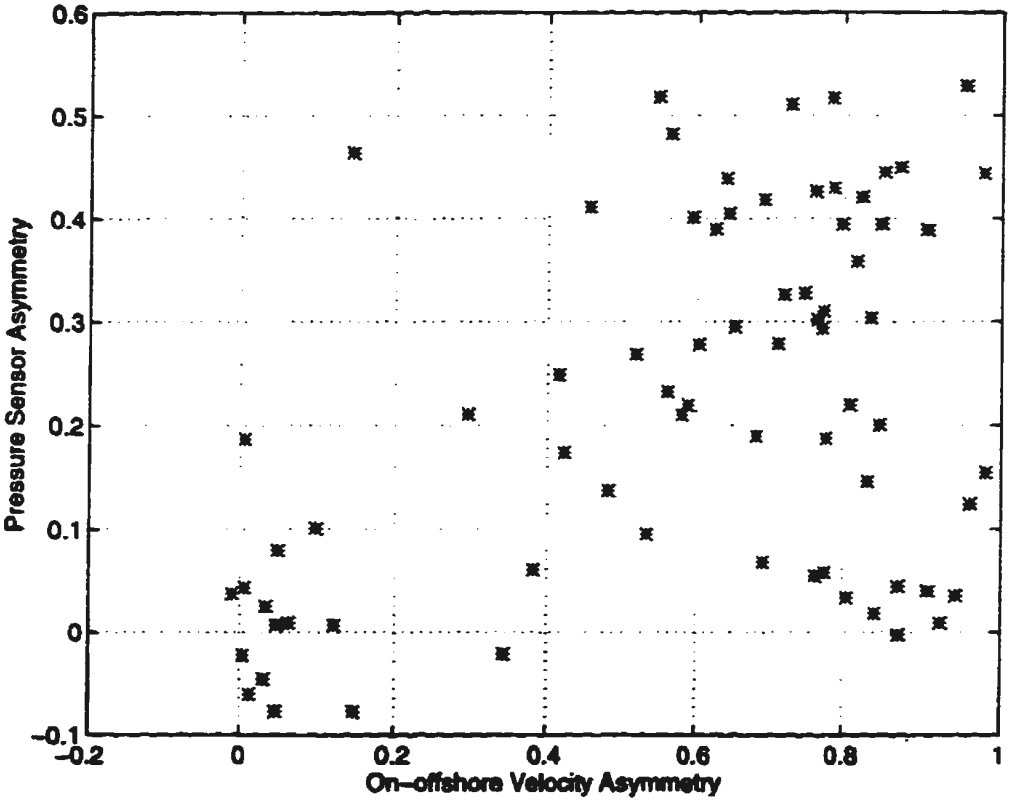

Figure A.3: Asymmetry calculated from on-offshore velocity compared to asymmetry obtained from a co-located pressure sensor. The data are from the Burley Beach 1992 experiment.

within 3 to 5% of those measured by the tow carriage (all low, suggesting a speed of sound related correction) with linear slope to within 1 % for speeds of .05 to .5 meters per second. The standard deviations for the speed in a given run was typically below 0.005 meters per second, some of which would have been due to vibrations and minor speed variations in the tow carriage. The main source of error in the ADV measurements was the signal to noise ratio in the returned sonar signal. The ADV measures the velocities of particles advected through the sample volume by correlating the signals from successive pings. If there are insufficient particles, spurious results are obtained. The ADV does calculate correlation coefficients, which drop if there are insufficient particles, so occasional samples with insufficient particles were screened out.

A.3.2 Statistics and Stationarity.

The sample rate from the UDATS system at Burley Beach was approximately 4 samples per second. Thus for a fifteen minute data segment there were 3500 data points. Perhaps of greater relevance to the analysis is the number of waves passing the instrument frame during fifteen minutes. The largest peak periods during the experiment were around six seconds, so that a minimum of 150 waves were analysed in a fifteen minute segment.

In the Ottawa'93 experiment analog data from the current meters and wave staffs were digitised by an OMEGA 16 channel analog to digital board placed in the personal computer which controlled the RASTRAN system. This board digitised samples for each RASTRAN cycle at approximately 10 samples per second. Typically, the wave paddle was programmed with a six minute wave record and thus a six minute repeat cycle. The typical wave period was 3.5 seconds, so approximately 100 waves would be processed for the numbers in Tables 3.1 and A.1. These waves were highly repeatable, so the uncertainties for the values were mainly due to the instrument calibration uncertainties.

Similar conditions applied for the Ottawa'95 wave measurements, though the effective sampling rate of the Acoustic Doppler Velocimeter was 8 samples per second, and current meter records of ten minutes duration were analysed. Thus approximately 170 waves were analysed for the numbers in Tables 3.2 and A.2.

A.3.3 Data Filtering.

For the Burley beach data, initial filtering consisted of identifying and smoothing small dropouts (of one to four data points) and eliminating portions of records where larger dropouts occurred. Several fifteen minute segments of data were not used because of serious noise in the signal. Periods for which the current meter appeared to be either too close to the bed or buried were also rejected. These periods were determined by comparing the amplitude of the response of the current meter to the pressure sensor which was mounted above the frame, and a segment of the data during the first storm was rejected as the current meter response was much smaller than the simultaneous pressure sensor response.

A.3.4 Wave Breaking.

In much of the nearshore studies literature, the flow field is split into two regions, "seaward of the breaker line", and "shoreward of the breaker line". The question of whether this criterion is relevant to bedform formation is still open in the literature, as there are very few observations shoreward of the breaker line. The data set here provides opportunity to address this question, as throughout the storms the "breaker line" moved on and off shore.

At Burley beach, the breaking of the waves was complicated by multiple bars present in the beach topography (Figure 2.3). A well defined breaker line was often difficult to discern, and may not have been present due to the irregularity of the storm generated waves. The post-storm swell was more regular, and for these waves the various wave breaking criteria suggested in the literature (Battjes 1988, or Horikawa 1988) can be

applied. The ratio of wave height to wavelength for a given water depth and beach slope has typically been used, but skewness and ratio of velocities at different depths has also been applied successfully.

In the Ottawa'93 experiment, the waves were not breaking over the test section of the wave flume. Yet crossripple bedforms were observed. In Ottawa'95, a portion of the JONSWAP simulating wave record which produced a breaking wave over the test area of the tank was found, and was run at 90 second repetitions (the remainder of the record contained smaller waves of pseudo-random frequencies and heights which filled in the JONSWAP frequency spectrum shape and wave height distribution).

A.3.5 Wave Flume Statistics.

Due to the unusual nature of some of the waves used in the Ottawa wave research flume, it was felt that additional statistics for the three different types may be of interest for comparison with other studies. Thus measured peak period T_p, depth h. surface standard deviation z_{rms}, the significant wave height $H_{1/3}$ (average height of the highest third of the waves), mean and variance of the velocities (u_m and u_{rms}) as well as the 'significant horizontal velocity' $u_{1/3}$ for the two Ottawa experiments have been given in Tables A.1 and A.2. Uncertainties in these quantities are due mainly to instrument calibration uncertainties or in some cases the instrument resolution. Uncertainty in the measured peak period T_p was ± 0.1 s, due to the resolution of the Fourier transform used (timing the wave paddle stroke would have been a more accurate measurement, but would not have worked for the JONSWAP simulated waves, so for consistency all the wave periods were measured by finding the energy peak in the Fourier transforms of the wave staff data). Uncertainty in the depth h was ± 0.05 m due mainly to variations in the amount of sand and bedform size in the test section. The wave staffs are very accurate and were calibrated several times throughout the experimental runs. A conservative estimate of their uncertainties is ± 0.005 m for each reading. The current meters were also calibrated, so uncertainties

have been estimated to be ±0.02 m/s.

Run	T_p	h	Wave Type	z_{rms}	$H_{1/3}$	u_m	u_{rms}	$u_{1/3}$	Bed
6	3.58	1.5	JONSWAP	0.074	0.28	0.00	0.16	0.29	L
7	3.78	1.5	JONSWAP	0.097	0.37	-0.03	0.20	0.37	I,L
8	3.82	1.5	JONSWAP	0.109	0.41	0.04	0.23	0.43	C,I
9	3.57	1.5	JONSWAP	0.121	0.45	0.03	0.25	0.47	C,I
10	3.42	1.5	JONSWAP	0.086	0.32	-0.14	0.18	0.34	I
11	3.61	1.5	Regular	0.070	0.20	0.02	0.16	0.24	L,I
12	3.61	1.5	Regular	0.106	0.30	-0.02	0.25	0.38	L
13	3.68	1.5	Regular	0.142	0.41	-0.06	0.33	0.50	I
14	3.61	1.5	Regular*	0.10	0.31	0.00	0.23	0.35	I,C
15	2.61	1.5	Regular	0.068	0.19	0.03	0.08	0.12	I
16	2.07	1.5	Regular	0.102	0.28	0.05	0.11	0.17	L
17	2.09	1.5	Regular	0.147	0.42	-0.03	0.15	0.24	L
18	5.13	1.5	Regular	0.103	0.30	-0.02	0.35	0.53	C,I
19	5.20	1.5	Regular	0.181	0.53	-0.12	0.60	0.89	M,E
20	3.64	1.5	Groups	0.074	0.28	0.02	0.16	0.31	I
21	3.64	1.5	Groups	0.147	0.56	-0.10	0.35	0.67	C
22	3.68	1.5	Regular	0.194	0.58	-0.11	0.46	0.68	M,E

Table A.1: Summary of wave conditions for the runs in the Ottawa National Research Council Wave flume, September 1993 experiment. T_p is the maximum wave energy period (±0.1 s), h is the water depth (±5 cm in the sandy test section). z_{rms} is the standard deviation of the surface (±0.005 m), $H_{1/3}$ is the significant wave height(±0.01 m), u_m mean velocity at the electromagnetic current meter depth (±0.02 m/s), u_{rms} the standard deviation of the horizontal velocity (±0.02 m/s), and $u_{1/3}$ average of the highest third of the velocities (±0.02 m/s). Also included in this table is the dominant bedform type observed to form under these waves. For a key to the bedform symbols, see the Introduction. Run 14 was unique in that the waves were generated with the wave paddle in flapper mode rather than the piston mode used in all the other runs. Note that all units are in meters and seconds.

Run	T_p	h	Wave Type	z_{rms}	$H_{1/3}$	u_m	u_{rms}	$u_{1/3}$	Bed
18	3.38	1.5	Groups	0.088	0.34	-0.02	0.19	0.41	I
19	3.37	1.5	Groups	0.070	0.26	-0.01	0.15	0.33	I,L
25	3.38	1.5	Groups	0.076	0.29	-0.01	0.15	0.33	L,I
26	3.38	1.5	Groups	0.088	0.33	-0.02	0.19	0.40	I
27	3.38	1.5	Groups	0.111	0.42	-0.02	0.26	0.52	I,C
28	3.38	1.5	Groups	0.151	0.60	-0.01	0.28	0.58	C
29	3.52	1.5	Groups	0.169	0.64	0.00	0.31	0.62	C,M
30	3.52	1.5	Groups	0.148	0.69	0.01	0.36	0.71	M
37	2.97	1.5	regular	0.097	0.47	0.01	0.26	0.39	L,I
54	3.52	1.5	JONSWAP	0.116	0.38	0.01	0.16	0.31	I,L
55	3.52	1.5	JONSWAP	0.129	0.45	0.02	0.19	0.39	I
56	3.37	1.5	JONSWAP	0.116	0.51	0.04	0.22	0.43	I,C
59	3.51	1.5	Groups	0.050	0.21	-0.00	0.10	0.22	L
60	3.47	1.5	JONSWAP	0.045	0.20	-0.00	0.10	0.20	L
62	3.37	1.5	Groups	0.101	0.40	-0.01	0.20	0.39	I
63	3.52	1.5	JONSWAP	0.069	0.28	0.01	0.11	0.22	I,L
64	3.47	1.5	Regular	0.151	0.44	-0.01	0.30	0.44	I
65	3.37	1.5	Groups	0.121	0.48	-0.00	0.24	0.49	I,C
66	3.52	1.5	JONSWAP	0.092	0.40	0.01	0.16	0.29	I
68	3.47	1.5	Regular	0.187	0.56	0.02	0.37	0.55	C
69	3.37	1.5	Groups	0.142	0.56	0.00	0.28	0.56	C
70	3.52	1.5	JONSWAP	0.117	0.46	0.02	0.20	0.38	I
71	3.47	1.5	Regular	0.222	0.65	0.07	0.45	0.67	M
72	3.38	1.5	Groups	0.168	0.69	0.02	0.35	0.69	M
73	3.52	1.5	JONSWAP	0.130	0.58	0.02	0.23	0.44	C
74	3.47	1.5	Regular	0.254	0.76	0.08	0.48	0.72	M
75	3.52	1.5	Groups	0.182	0.76	-0.02	0.34	0.71	M

Table A.2: Summary of wave conditions for the runs in the Ottawa 1995 experiment. T_p is the maximum wave energy period (±0.1 s), h is the water depth (±5 cm in the sandy test section). z_{rms} is the standard deviation of the surface (±0.005 m), $H_{1/3}$ is the significant wave height(±0.01 m), u_m mean velocity at the electromagnetic current meter depth (±0.02 m/s), u_{rms} the standard deviation of the horizontal velocity (±0.02 m/s), and $u_{1/3}$ average of the highest third of the velocities (±0.02 m/s). Also included in this table is the dominant bedform type observed to form under these waves. For a key to the bedform symbols, see the Introduction. Note that all units are meters and seconds.